Title
Understanding the Dynamics of Complex Fluids Using Microfluidics: Suspensions and Wormlike Micellar Solutions

Author
Hwang, Margaret Yvonne

Publication Date
2017

Peer reviewed|Thesis/dissertation

Understanding the Dynamics of Complex Fluids Using Microfluidics: Suspensions and Wormlike Micellar Solutions

By

Margaret Yvonne Hwang

A dissertation submitted in partial satisfaction of the

requirements for the degree of

Doctor of Philosophy

in

Chemical Engineering

in the

Graduate Division

of the

University of California, Berkeley

Committee in charge:

Professor Susan J. Muller, Chair
Professor Clayton J. Radke
Professor Amy E. Herr

Summer 2017

Understanding the Dynamics of Complex Fluids Using Microfluidics:
Suspensions and Wormlike Micellar Solutions

Abstract

Understanding the Dynamics of Complex Fluids Using Microfluidics:
Suspensions and Wormlike Micellar Solutions

by

Margaret Yvonne Hwang

Doctor of Philosophy in Chemical Engineering

University of California, Berkeley

Professor Susan J. Muller, Chair

Microfluidics are often used to inform the design of applications such as blood additives, high-throughput DNA sequencing, and point-of-care/lab-on-chip diagnostics. The small characteristic length scales in microfluidic systems can be leveraged to maintain low Reynolds numbers Re (ratio of inertial to viscous forces); with a viscoelastic fluid, the length scales can also lead to high elasticity numbers El (ratio of elastic to inertial forces). As a result, flow in microfluidic devices is not turbulent and can be highly elastic, providing a wealth of experimental capabilities. These include multiphase flow manipulation (which can be used to generate monodisperse bubbles and drops), trapping and analysis of single cells, and the development of secondary flows driven by elasticity. This dissertation focuses on three microfluidic studies: 1) microparticle generation and characterization, 2) examination of suspension flow dynamics, and 3) development of elastic instabilities in viscoelastic fluids flowing around a sharp bend.

Microfluidic devices are capable of monodisperse, deformable particle generation, which is advantageous for tuning the specific properties of suspension components. This facilitates the systematic study of individual component properties on suspension flow behavior such as lateral migration and enables the study of suspension flow dynamics. Microfluidics is an ideal platform for studying suspension flow phenomena due to the long entry lengths needed to observe lateral migration. Although these length scales are large in macroscale, potentially on the order of meters, in microscale the entry length can be on the order of centimeters. This work additionally concerns the development of elastic instabilities in wormlike micellar solutions, a class of surfactant-based viscoelastic fluids. Due to the coupling of the elastic nature of wormlike micellar strands and the curvature of the flow streamlines, wormlike micellar solutions in flow can develop secondary flows (vortices). Despite the prevalent use of wormlike micellar solutions in consumer products, in drug delivery, and in drag-reducing agents, their structure and the mechanics of their flow behavior are not well understood. Planar microdevices can be used to investigate purely elastic instabilities that develop from a combination of shear or extensional flows. In contrast to flow in the more commonly studied microfluidic cross slot and contraction geometries, which is predominantly extensional, the flow in a sharp 90-degree bend is shear-dominated.

This dissertation first investigates controlled microparticle generation and characterization. Monodisperse particles of varying size, shape, and deformability were produced using two microfluidic strategies. First, monodisperse emulsion droplets of a crosslinkable polymer solution were generated via a flow-focusing design, in which drops are formed from a central emulsified phase that is focused by adjacent continuous phases, generating well-controlled drop sizes from 45 to 183 μm. Subsequently, droplets were crosslinked either 1) on chip, resulting in spherical particles, or 2) in an external gelation bath, resulting in an assortment of non-spherical, axisymmetric particles. Particle deformability was then quantified using micromechanics in a tapered capillary, where a particle is trapped at the tip of the taper. The shear and compressive moduli were obtained simultaneously by applying a range of hydrostatic pressures on the particle and analyzing the resulting particle deformation. This method allowed for differentiation between shear and compressive moduli and determined an effective modulus for an entire particle rather than a localized modulus. Changing the polymer system, crosslinker concentration, or polymer concentration produced particles with shear moduli (G) ranging over three orders of magnitude, from 0.013 kPa to 26 kPa.

This library of particles was then used for lateral migration studies in long channels. The lower moduli microparticles ($G < 0.10$ kPa) are sufficiently soft to deform in channel flow, undergoing similar shape transitions as those seen in literature for capsules and vesicles. With increasing viscous shear, initially circular solid elastic particles in confined channel flow form egg-like, triangular, arrowhead, and finally parachute-like shapes. These shapes are distinct from previously reported capsule and vesicle deformation shapes and can be quantified by dimensionless quantities such as circularity, elongation, depth of the dimple at the trailing edge, and radius of curvature at the leading edge of the particle. Correlations were observed between capillary number Ca (ratio of viscous forces to restoring forces, in this case shear modulus) and the deformation as characterized by two parameters: circularity and radius of curvature at the tip. At low Ca, particle deformation is small and circularity is very close to 1; as Ca increases, circularity changes become more significant. Using circularity and radius of curvature at the tip, it is possible to obtain Ca and the corresponding shear modulus for individual particles from their deformation in channel flow.

The final focus of this work is to examine the behavior of wormlike micellar solutions in a shear-dominated flow, particularly considering the flow and instabilities of shear thinning polymeric and wormlike micellar solutions through a microfluidic 90-degree bend. Two wormlike micellar solutions of cetylpyridinium chloride (CPCl) and sodium salicylate (NaSal) in water were investigated. At low NaSal to CPCl ratios, the wormlike micelles were linear; however, at high ratios the wormlike micelles became branched and showed shear banding within a range of shear rates. Microfluidic experiments on all solutions studied revealed unique regimes as secondary flows developed. At a critical Weissenburg number Wi (the ratio of elastic forces to viscous forces in shear), the flow of the polymeric solution transitioned from a steady base flow to a secondary flow that is characterized by the formation of a stationary lip vortex. The wormlike micellar solutions developed intermediate secondary flow behavior as Wi increased before transitioning to a third regime characterized by a time-dependent lip vortex. The linear wormlike micellar solution revealed a second regime similar to the one observed in the polymeric solution,

but the branched, shear-banding wormlike micelle solution developed an intermittent outer corner vortex in addition to a time-dependent lip vortex. In contrast, no third regime was apparent in the polymeric solution over the same range of Wi. These differences in flow behavior demonstrate that the stability of elastic flows is a strong differentiator of rheological differences.

Table of Contents

List of Figures

List of Tables

Acknowledgements

First and foremost, I would like to thank Susan for being a wonderful advisor throughout my time at Berkeley. She has been incredibly witty, patient, and perceptive, providing me with a wealth of advice and guidance. Under her mentorship and support, I have matured as a researcher and an engineer, and I am extremely thankful for the opportunity to have worked in Muller Lab. I would also like to thank the rest of my dissertation committee, Prof. Radke and Prof. Herr, for their insightful and thorough feedback during my qualifying exam and dissertation writing.

Muller Lab members, past and present, have provided endless advice, discussions, collaborations, and company: Kari Storslett, Thibaut Divoux, Joanna Bechtel Dahl, Fatemeh Khalkhal, Hadi Mohammadigoushki, Prof. Ruri Hidema, Naoto Oba, Prof. Heon Sang Lee, and Yiran Zhang. In particular, Kari has been a reliable and invaluable friend and labmate starting from the very beginning, when Muller Lab had a population of two. I have been fortunate to have worked with two undergraduate researchers: "Phil" Yong Bin Kim and Timothy Sivaraman, who were enthusiastic and hard-working.

I am grateful for the financial support that I have received from the National Science Foundation through the Graduate Research Fellowship.

My graduate school life has been balanced and enriched by the friends I have made at Berkeley: Alex and Sarah Wang, Lisa Felberg, Alex Albaugh, Ellyn Gendler, Brian and Elisabeth Perea, Nico Herman, Adriana Rojas, Gina Noh, Eddie and Ellie Buehler, Meron Tesfaye, Jessica Nichols, and Emily Davidson. Without Thursday night trivia, potlucks, opera, and board games, my Berkeley experience would have been incomplete. I am also grateful to my friends outside of lab and graduate school, Eric and Lauren King, Thad Macy, Ian Strzyzewski, and Kelly Taylor, for their friendship and support. I would finally like to thank my parents, Daniel and Monica, and my sister Maxine for their encouragement and unwavering support.

1 Introduction

1.1 Advantages of Microfluidic Systems

Microfluidic systems are devices with small characteristic length scales, on the order of tens or hundreds of micrometers, designed to manipulate small volumes of liquid. The small volumes provide many advantages for analysis, including low sample or reagent consumption, small device footprint, short analysis times, and low fabrication costs.[1,2] The small length scales also mean that microfluidic systems are characterized by laminar flow, diffusion-dominated mass transfer, and large area-to-volume ratios resulting in thermal homogeneity. These features enable well-controlled manipulation of flow and uniform conditions. There are a wide range of applications, including single-molecule or single-cell experiments,[3–5] high-throughput DNA sequencing,[6,7] point-of-care/lab-on-chip diagnostics,[8–10] and simulating physiological systems and organs.[11,12]

Due to the small length scales found in microfluidic devices, flow can exhibit interesting dynamics, the regimes of which are described by non-dimensional parameters. The relevant non-dimensional parameters in microfluidic systems include Reynolds number Re (the ratio of inertial to viscous forces), Weissenberg number Wi (the ratio of elastic forces to viscous forces in shear), Deborah number (the ratio of the characteristic time of the fluid to that of the flow), and elasticity number El (the ratio of elastic to inertial forces), defined in Equations 1-1, 1-2, 1-3, and 1-4, respectively.

$$Re = \frac{\rho U L}{\mu} \qquad \text{(Equation 1-1)}$$

where ρ is solution density, U the average velocity in the channel, L is the characteristic length scale, and μ is the solution viscosity.

$$Wi = \lambda_1 \dot{\gamma} \qquad \text{(Equation 1-2)}$$

where λ_1 is the longest relaxation time of the solution and $\dot{\gamma}$ is the characteristic shear rate, which can be approximated as U/L.

$$De = \lambda_1 \dot{\varepsilon} \qquad \text{(Equation 1-3)}$$

where $\dot{\varepsilon}$ is the extension rate.

$$El = \frac{Wi}{Re} = \frac{\lambda_1 \mu}{\rho L^2} \quad \text{(Equation 1-4)}$$

Microfluidic devices often have low Re, reflecting minimal inertial effects and resulting in laminar flow. However, at sufficiently high flow rates when Re > 1, inertial effects can be examined without needing to account for turbulence. This can lead to a number of interesting behaviors, such as cross streamline migration of a particle in laminar flow,[13,14] further described in Section 1.2.

Because Re scales with characteristic length scale L and shear rate $\dot{\gamma}$ (and accordingly Wi) scales with L^{-1}, small length scales can also lead to highly elastic flows, characterized by high El (El > 1) (Eq. 1-4). This drives the development of secondary flows. Thus, microfluidic systems can examine purely elastic instabilities, occurring in the presence of strong elastic forces and negligible inertial forces (low Re), which could otherwise mask viscoelastic effects or couple with elastic effects and lead to inertio-elastic instabilities. Elastic instabilities have been examined in a range of planar microfluidic geometries, including expansion/contractions,[15] cross-slots,[16–18] serpentine channels,[19,20] and sharp corners.[21,22] A commonly used microfluidic geometry is the cross-slot, which has opposing inlets and opposing outlets perpendicular to the inlets. In this geometry, the flow is shear dominated at the walls and extension dominated near the center, with a stagnation point at the exact center. For example, Arratia *et al.* used polyacrylamide/glycerol/water solutions to examine purely elastic transitions, finding that the symmetric base flow becomes steady and asymmetric then unsteady and asymmetric with increasing De.[23] As flow in microchannels is laminar, mass transfer normal to the direction of flow is generally diffusion controlled and inefficient. As a result, the onset and development of purely elastic instabilities is applicable to mixing, which can be otherwise difficult to induce in microchannels.[24]

Multiphase flows, with more than one fluidic phase in contact, can also be manipulated in microfluidic systems. This allows for the generation of monodisperse emulsion drops or bubbles, where a liquid or gas phase is dispersed in a second immiscible liquid phase.[25–28] Control of this generation can lead to controlled synthesis of microparticles,[29–34] foams,[35–37] and emulsions as well as contribute to single-cell culture and analysis capabilities.[7,38,39] Drop formation depends primarily on the capillary number Ca (viscous to restoring forces), in which the restoring force depends on the system, e.g. in drop formation, the restoring force is interfacial tension. A common geometry used is flow focusing, which consists of one phase in a center channel that is pinched into drops (hence, it is referred to as the dispersed phase) by the flow of an immiscible, continuous phase in the two outer channels (Fig. 1-1). [26,27,40–43] Anna and Mayer have characterized drop formation regimes based on Ca.[27] As demonstrated by Lee *et al.*, drop size depends on the ratio of the dispersed to continuous phase flow rates, the continuous phase flow rate, and the characteristic length scale of the device.[40] Nie *et al.* also found that relative fluid viscosities affects drop formation.[41] Optimization of flow rates and relative viscosities allows for easy control of resulting emulsion drop characteristics that lead directly into microparticle generation.

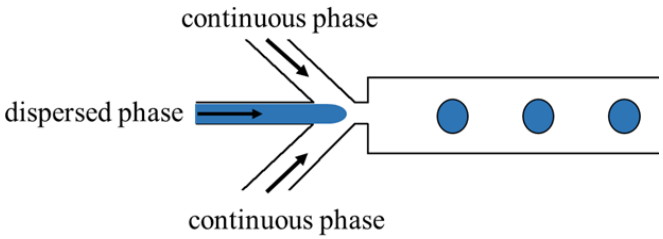

Figure 1-1. Schematic of a flow-focusing geometry used for generating emulsion drops

Other multiphase flows are also characterized by Ca, where emulsion droplet, capsule, vesicle, or elastic particle deformation is driven by Ca. In each of these cases, the restoring force is different, being interfacial tension, membrane shear modulus, membrane bending modulus, or bulk shear modulus dominated, respectively. For contrast, Equation 1-5 defines Ca for a vesicle, where d is the vesicle diameter and κ is the membrane bending modulus, and Equation 1-6 defines Ca for a solid elastic particle, where G is the particle bulk shear modulus.

$$Ca = \frac{\mu \dot{\varepsilon} d^3}{\kappa} \qquad \text{(Equation 1-5)}^{44}$$

$$Ca = \frac{\mu \dot{\gamma}}{G} \qquad \text{(Equation 1-6)}$$

As Ca increases, the viscous forces from the flow become more dominant, and as a result, the soft-object deformation increases. Consequently, to see notable deformation experimentally, we target finite Ca > 0.1.

1.2 Suspension Flow Behavior

Suspensions—multicomponent soft materials consisting of particulates dispersed into a liquid phase—are found in consumer products such as paint, food, and cosmetics, biological fluids such as blood, and in pharmaceuticals as drug delivery particles. With moving particles in a moving fluid, suspension flow behavior is a two-phase flow that cannot easily be described with classical models.[45] Based on a variety of parameters such as component size,[46,47] shape,[33,48,49] stiffness,[50–52] and concentration,[53–55] solvent rheology,[56–58] flow Reynolds number,[13,14,59] and channel curvature,[60,61] suspension flow behavior and bulk properties can vary greatly. Better understanding of suspension flows and how they are affected by the many parameters and their interactions informs the design of blood additives for drug delivery and trauma therapy.

Cross-streamline lateral migration of suspension components can occur in channel flow. For example, in capillary blood flow, red blood cells have been observed to migrate away from the channel walls toward the tube center, resulting in a cell-free

layer adjacent to the tube wall.[62,63] This cell-free layer is observed experimentally through the Fahraeus–Lindqvist effect, where the viscosity of blood decreases with a decrease in a microchannel's diameter as the red blood cells move toward the center and leave plasma and platelets at the wall.[64] This also results in a process called "margination", the segregation of the larger, more deformable red blood cells to the center and the smaller, more rigid platelets and the leukocytes to the walls. Figure 1-2 illustrates this behavior. In comparison, in the absence of inertia, dilute rigid spherical particles are not expected to migrate across streamlines due to the reversibility of Stokes equation.

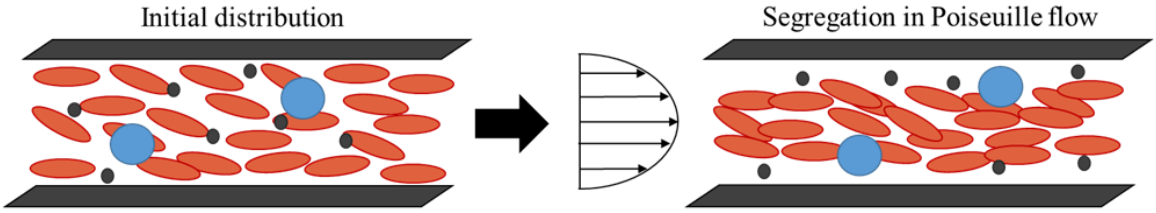

Figure 1-2. Cartoon depiction of segregation in blood flow, with red blood cells (red ellipses) concentrating in the center of the channel, and white blood cells (large blue circles) and platelets (black small circles) moving toward the walls. Adapted from Kumar and Graham.[65]

Although this migration process is driven by the size, rigidity, concentration, and shape of the components in a multicomponent suspension, how these properties result in margination is not well understood. Many studies have examined this process, but most have been with dilute suspensions that do not examine how component concentrations and the resulting interactions affect segregation. In addition, the majority of studies were performed on systems where the components studied vary in diameter, shape, and rigidity simultaneously, so it is difficult to isolate the role of each property. For example, computational studies have been done on the margination of platelets in a suspension of red blood cells, which is a complex system involving the more rigid, smaller platelets and less rigid, larger red blood cells.[66] One study by Kumar, Rivera, and Graham addresses this issue by computationally examining the effects of component size and rigidity on particle segregation in shear flow.[47] However, this study does not address the effects of increasing concentration and shape on margination. In addition, experimental results on rigid particles show contradictory results when compared to theory. Segre and Silberberg demonstrated that rigid spheres in inertial pipe flow migrate to a steady state position at 0.6R, where R is the radius of the pipe.[67] However, Matas, Morris, and Guazzelli experimentally showed that as particles increased in size relative to the pipe radius, the particles migrate toward the center of the pipe instead.[68] This demonstrates the need for further study on suspension focusing lengths and steady state positions.

Understanding lateral migration has implications in membrane-less cell trapping and sorting, which can be used in applications such as point-of-care diagnostics, cell counting, and continuous flow separation. For example, separating

infected red blood cells from healthy ones is vital to diagnosing and treating malaria.[9,69] Fluorescence-activated cell sorting (FACS) is currently commonly used for cell sorting, where cells are labeled with fluorescent molecules, and each individual cell is identified by the fluorescence signal,[70] but a number of microfluidic techniques have been proposed, including active techniques, e.g. magnetic[71] or electrophoretic cell sorting,[72] and passive techniques driven by channel geometry and hydrodynamic forces.[73–76] Numerous studies have been done on inertial focusing, which exploits inertial lift forces, occurring at finite Re, to control cell equilibrium positions.[13] The equilibrium positions depend on component size,[59] shape,[49] and modulus.[77] Understanding and manipulating parameters that drive lateral migration can inform the design of passive separation techniques, which are desirable because no external forces or additional labeling are needed.

Characterizing and leveraging suspension component deformation is also vital to a number of practical applications, including cell separation and drug delivery. Not only do blood components have different rigidity (red blood cells are more deformable than white blood cells and platelets), but red blood cells can stiffen in response to infection such as malaria[78] or sickle cell disease.[79] Microfluidic systems have been proposed for separating objects based on deformation.[80,81] Particle deformation also affects lateral migration, as deformation in flow can result in asymmetric shapes that can migrate across streamlines even in the absence of inertial lift forces.[56,82] As such, deformable suspension components have been shown to have different equilibrium positions compared to rigid objects both computationally and experimentally.[77,83,84] Shin and Sung computationally examined inertial migration of an elastic capsule, concluding that as membrane bending coefficient increased and capsule deformation decreased, the equilibrium position moved further from the channel center.[84] Hur *et al.* also noted the same trend for inertial migration of emulsion droplets, where the lower viscosity droplets focused to positions closer to the center of the channel.[77]

Capsules and microparticles are also in use as potential targeted drug delivery particles, meant to disperse pharmaceuticals to desired regions, which requires careful control of their properties.[85] As a result, controlling and characterizing mechanical properties of micro-sized objects is key, but experimentally obtaining the deformability of ~10-100 μm sized particles can be complicated. Common techniques used to obtain the deformability of cells and other microscale particles, such as atomic force microscopy (AFM),[86] micropipette aspiration,[87,88] and optical stretching,[89] measure a localized modulus that is strongly affected by the particle surface, with measurements that can vary with the technique used. Microfluidics-based platforms have also been examined for the characterization of cell deformation. However, many of these methods result in values relative to a baseline, qualitative comparison rather than an absolute measurement.[90–92] Other microfluidic devices have been used to examine the behavior of deformable objects in flow and confined channels, as the resulting shapes and equilibrium positions have implications in drug diffusion for drug delivery particles, gas transfer in microcirculation, and rupture time for payload delivery. Constriction channels were used by Haghgooie *et al.*[33] and Merkel *et al.*[93] to characterize the ability of synthesized particles to deform in flow conditions. Work from Hu and co-workers also examined the flow of capsules in capillary flow with circular or square cross

sections computationally and experimentally, finding that the capsule shape and flow is affected by 3D effects and characterizing membrane properties is vital, proposing a combination of experiments and numerical modeling to infer membrane mechanical properties.[94,95] Understanding the role of suspension component deformability on flow behavior requires both characterization of the component mechanical properties and the deformed shapes an object takes in response to flow.

1.3 Wormlike Micellar Solutions

Wormlike micelles (WLMs), which are often used in consumer products or as drag reduction agents, are composed of surfactants: amphiphilic molecules with a hydrophobic tail and a hydrophilic head. In an aqueous solution, when the concentration of the surfactant is above the critical micelle concentration (CMC), the surfactant arranges into spherical aggregates known as micelles to shield the hydrophobic tails. For some surfactants or surfactant/salt combinations, such as cetyltrimethylammonium bromide (CTAB) or cetylpyridinium chloride (CPCl), as the concentration increases, rod-like cylindrical micelles form—wormlike micelles. As the cylinder length becomes greater than the persistence length, the WLMs become semi-flexible; their behavior is similar to that of polymer solutions. This trend is illustrated in Figure 1-3. Unlike polymer chains, however, WLMs break and reform under shear.[96,97]

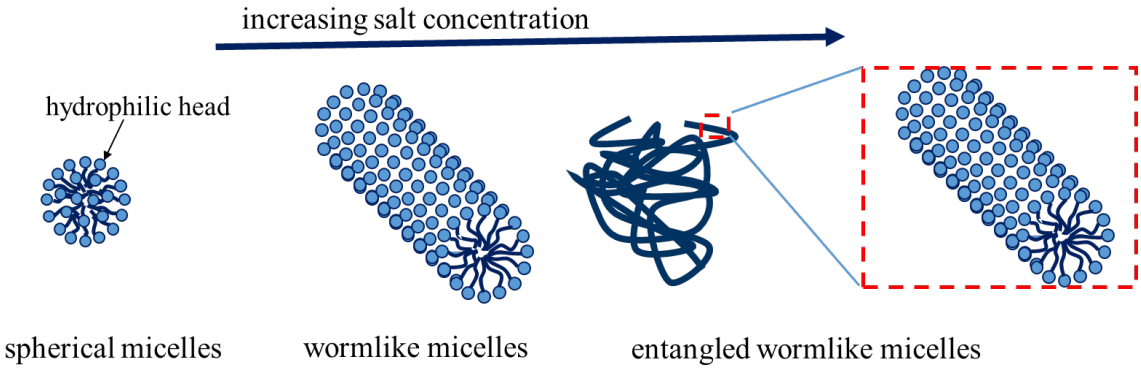

Figure 1-3. Diagram of wormlike micelle solutions with different morphologies as salt concentration is increased: spherical, wormlike, and long, entangled micelles.

In the dilute regime, WLM solutions behave as Newtonian fluids, but with increasing salt and/or surfactant concentration, the solutions can become viscoelastic because of entanglements between the wormlike micelles, similar to how polymer chains entangle in solution.[98,99] Solutions can also become shear-thinning as micelles orient in shear flow above a critical shear rate.[100] At appropriate concentration and temperature, WLM-solution behavior can be described with a single-mode Maxwell model in small amplitude oscillatory shear flow, behaving as if it has a single relaxation

time, unlike polymer solutions, which exhibit a spectrum of relaxation times.[96] In the non-linear regime, WLM solutions can undergo shear banding in simple shear flow, characterized by a stress plateau on the shear stress versus shear rate curve.[101–103] This reflects the change in flow behavior with increasing shear rate. WLM solutions at low shear rates flow homogeneously (the low shear-rate phase). Above a critical shear-rate $\dot{\gamma}_1$, the solutions can split into shear bands, where low and high shear-rate layers coexist at the same shear stress, a behavior known as shear banding. When the shear-rate is above a second critical shear rate $\dot{\gamma}_2$, the fluid returns to a homogeneous phase, the high shear-rate phase.[102]

For a salt/surfactant combination such as cetylpyridinium chloride (CPCl) and sodium salicylate (NaSal), increasing salt concentration past a critical threshold can also result in a change in wormlike micelle structure, where branch points develop and branched networks form.[104,105] This structure change has been observed with Cryo-TEM.[106–108] As Gaudino *et al.* observed, the change in structure is also reflected in the rheology—relaxation time increases with increasing salt concentration, reflecting increasing micelle length, until a maximum is reached, after which there is a rapid decrease in relaxation time. The maximum relaxation time occurs at the concentration at which the branches begin to form, and the subsequent decrease in relaxation time corresponds to where micelle branching rather than chain lengthening occurs (Fig. 1-4).[107]

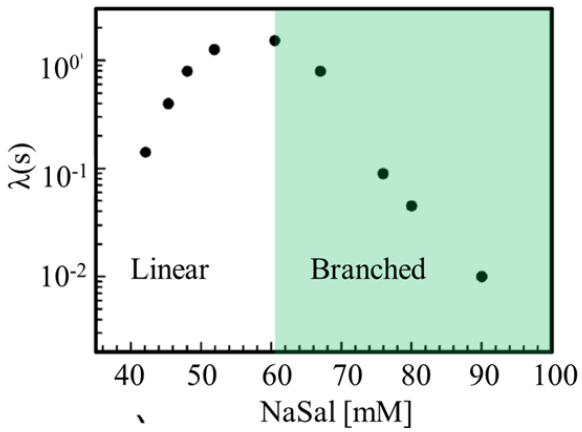

Figure 1-4. Relaxation time as a function of NaSal concentration for NaSal-CPCl solutions, where [CPCl] = 100 mM. White fill indicates [NaSal] where the wormlike micelles are linear; green fill indicates branched wormlike micelle structure. Modified from Gaudino *et al.*[107]

With these complex rheological and structural properties, WLM solutions have been used to examine viscoelastic instabilities in both macroscale geometries such as Taylor-Couette cells[109–111] and microscale geometries such as expansion/contractions[112] and cross slots.[113–115] The instability of the interface between shear bands has been examined experimentally in macroscale in the Taylor-Couette geometry, where two bands formed above a critical shear rate and eventually undulated.[110,116–119] Fardin *et al.* observed the development of first undulation at the

band interface at $\dot{\gamma}$=35 s^{-1}, then Taylor-like vortices in CTAB/sodium nitrate ($NaNO_3$) solution above $\dot{\gamma}$=65 s^{-1}, resulting in 3D flow. However, they could not isolate the effect of the vortices from the interfacial instability.[116] They suggested that the onset of instability occurred above a critical Wi based on the shear rate in the high shear-rate band and the thickness of that band, where the 3D disturbances in a geometry with curved streamlines were driven by elastic instability.[109] Fardin *et al.* examined the effect of temperature, salt and surfactant concentration, and effective gap width on flow stability. They summarized a large set of Taylor-Couette experiments into three categories of shear banding, based on stability.[117]

The majority of macroscale experiments on WLM solutions have been on simple shear or shear-dominated flows with curved streamlines. In contrast, planar microdevices allow for exploration of instabilities that develop from a combination of shear or extensional flow. Using a microfluidic cross-slot geometry, Pathak and Hudson studied instabilities in CTAB/NaSal and in CPCl/NaSal solutions, and reported the development of sharp birefringence bands at moderate Wi.[115] Pathak and Hudson also observed that at high Wi, the flow becomes asymmetric, but the velocity profiles did not show shear banding. Haward *et al.* also examined CPCl/NaSal solutions in a deep cross slot, finding three regimes of flow behavior: steady symmetric flow at Wi < 1, steady asymmetric flow at Wi > 1, and time-dependent aperiodic flow at Wi > 350. Similar series of transitions were also observed in a deep cross-slot for linear polymer solutions and CTAB/NaSal WLM solutions.[16,114]

Microfluidic expansion/contraction geometries have also been studied for their capability to generate strong extensional flows as well as for their similarity to flows found in nature, such as flow through pores in rocks. Computationally, Stukan and co-workers examined the effects of micelle size, channel dimensions, and fluid nature on the distribution and orientation of wormlike micelles.[112,120] Experimentally, Ober *et al.* combined pressure drop measurements, micro-particle image velocimetry, and birefringence measurement to characterize viscoelastic effects of a CPCl/NaSal system in a hyperbolic contraction geometry.[121] Overall, extension dominated viscoelastic instabilities have been widely studied in microfluidic systems, but there are few experimental studies done in microfluidic shear-dominated flows.

1.4 Dissertation Overview and Objectives

The main objective of this work is to leverage microfluidics to examine the dynamics of complex fluids, specifically microparticle suspensions and wormlike micellar solutions. The characteristic length scales facilitate the examination of flow with low inertia and high elasticity. Furthermore, microfluidics allows for clear visualization of individual suspension component movement and deformation in flow. With low fabrication costs and rapid prototyping capabilities, microfluidic platforms provide a host of potential applications, and Chapter 2 describes the different devices used, ranging from flow focusing devices for generating microparticles to long microchannels used for migration studies. In addition, a capillary micromechanics technique for quantifying microparticle moduli is described and validated. Finally, the

experimental procedures for characterization of solutions in flow are presented. Careful consideration is also given to the image capture and image analysis needed to characterize flow.

1.4.1 Generation and Examination of Microparticles in Flow

Because the effect of suspension parameters—particularly size, deformability, and shape—and their interactions on lateral migration and component flow behavior is not fully understood, it is necessary to perform controlled studies where each property is varied while all others are held constant. To isolate variable effects, it is ideal to run a microfluidic model system as opposed to blood. Thus, one aspect of this project is to characterize the dynamics of suspension flows in microchannels and examine how individual suspension properties affect flow. Microfluidics provides two main advantages for investigating suspension migration. First, microfluidic devices are capable of monodisperse, deformable particle generation, which is advantageous for making suspensions of desired components. Second, particle migration has long length scales. Nott and Brady have shown that in a rigid sphere suspension of finite volume fraction, the focusing length scales as $\frac{L_f}{H} \sim \left(\frac{H}{d}\right)^2$, where L_f is focusing length, H is half the height of the channel, and d is particle diameter.[54] As a basic comparison, with an H/d ratio of 10, entry length L_f would need to be proportional to $100H$, which can be on the order of meters in a macroscale set-up, but with microfluidics, this ratio is easily obtainable (order of centimeters).

Table 1-1. Parameters characterizing suspension flow experiments and suspension component properties.

Category	Symbol	Definition	Units
Fluid properties	ρ	Density	[kg/m^3]
	μ	Viscosity	[Pa·s]
	λ_1	Longest relaxation time	[s]
	σ	Interfacial surface tension	[N/m]
Experimental parameters	h	Channel height	[m]
	w	Channel width	[m]
	q	Flow rate	[m^3/s]
	L_f	Focusing length	[m]
Suspension component parameters	D	Particle diameter for a circular particle	[m]
	D_{max}	Maximum particle diameter	[m]
	G	Shear modulus	[Pa]
	K	Compressive modulus	[Pa]

To control and systematically vary component properties used in the study of suspension dynamics, we first focus on developing a library of fully characterized, monodisperse soft particles, targeting shear moduli ~10 to 100 Pa. Table 1-1 above enumerates the relevant variables and their definitions. Chapter 3 details the application

of a basic flow-focusing geometry to obtain alginate and poly(N-isopropylacrylamide) (pNIPAM) soft particles of varying polymer concentrations. The on-chip gelation design (Fig. 1-5(a)) was optimized for long-term particle generation and control of particle size. Capillary micromechanics, where the particle is trapped in a tapered tip and deformed at a variety of hydrostatic pressures, was used to obtain the range of moduli attainable. Finally, off-chip gelation in an external bath (Fig. 1-5(b)) was considered for generating non-spherical particles and controlling particle shape.

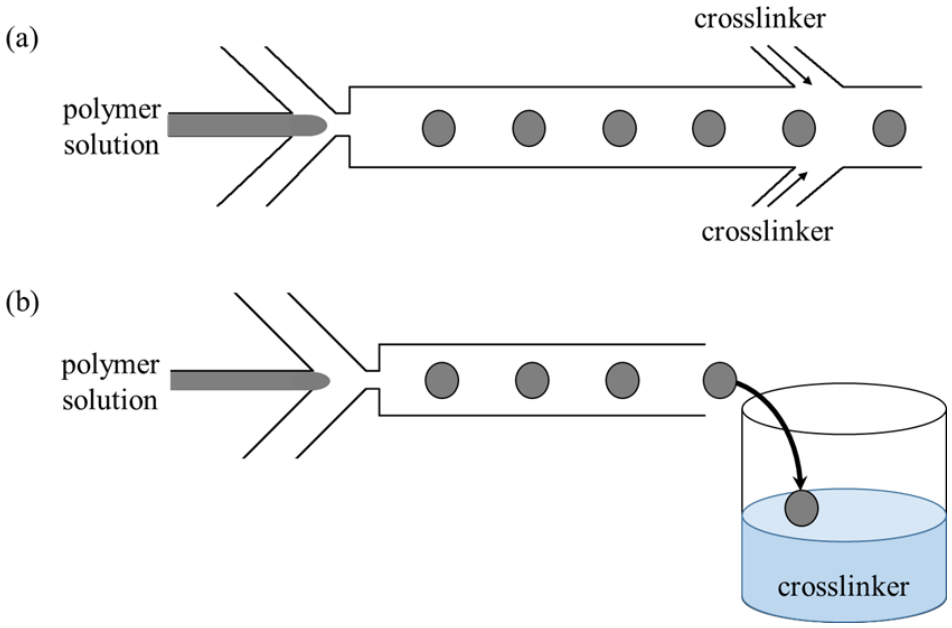

Figure 1-5. Schematic depicting (a) on-chip and (b) off-chip gelation techniques. A flow-focusing design generates polymer solution drops (gray), which are crosslinked further downstream as indicated.

Once the suspensions were generated, their behavior was then examined in microchannels, as described in Chapter 4. The softest pNIPAM particles could reach finite Ca numbers, allowing for the exploration of particle deformation in confined rectangular microchannels. The shape profiles that developed as Ca was increased were characterized with an edge detection procedure. Using dimensionless quantities, the thresholds between each shape category were identified. We present the new shapes for soft elastic particle deformation, noting that they are distinct from those reported in literature for capsules and vesicles.[95,122,123] Finally, we propose the use of particle deformation in flow as a measure of particle shear modulus.

1.4.2 Stability of Wormlike Micelle Solutions in a High El Flow

Although considerable microfluidic studies have been performed with viscoelastic fluids in cross slots and abrupt expansion/contractions, these geometries generate primarily extensional flow. The particular geometry we explore is a sharp 90 degree bend; with strong shear at the walls and a lack of channel constrictions, the flow is shear-dominated flow. In addition, sharp corners are designed into many microfluidic devices and, as such, are good to characterize for a variety of fluid flows. Previous studies in our laboratory by Gulati *et al.*[21,22] studied the microfluidic-bend geometry for the first time, examining the flow of viscoelastic, shear-thinning solutions of DNA and polyethylene oxide/polyethylene glycol/water (PEO/PEG/water), accessing El >>1. Beyond a critical threshold, they observed the formation of a steady lip vortex upstream of the corner. However, this secondary flow never developed with the flow of a non-shear thinning viscoelastic PEO/PEG/water solution. In Chapter 5, the results of work exploring wormlike micellar solutions made of cetylpyridinium chloride and sodium salicylate are reported in a sharp bend. The rheological characterization methods are also briefly discussed in this chapter. First, a comparable shear thinning, viscoelastic PEO/PEG/water polymer solution is discussed as a baseline and for comparison with Gulati *et al.*,[21] as the geometric parameters of the device are slightly different. Next, the onset and regimes of secondary flows in CPCl/NaSal solutions with two salt to surfactant ratios are discussed. Notably, the two WLM solutions have different rheological behavior (shear-banding versus shear thinning) and micelle structure (linear versus branched). Finally, we report on the new transitions and instability regimes that were observed.

Lastly, the major conclusions and suggestions for future work are summarized in Chapter 6. The appendices predominantly expand on Chapter 2 regarding the experimental procedures, providing detailed protocols for a number of techniques. Appendix A provides a detailed description of microfluidic device fabrication techniques, including standard soft lithography and master fabrication. Appendix B then provides specific guidelines for generating a range of microparticles. Appendices C and D describe set-up and recommendations for capillary micromechanics and suspension flow experiments, respectively. All MATLAB and ImageJ codes used for suspension characterization are contained in Appendix E. Finally, Appendix F details the experimental set-up and analysis of sharp bend experiments.

2 Experimental Methods for Suspensions

Parts of this section are reproduced or modified with permission from:

Hwang, M. Y., Kim, S. G., Lee, H. S., and Muller, S. J., "Generation and characterization of monodisperse deformable alginate and pNIPAM microparticles with a wide range of shear moduli." *Soft Matter*, 2017, DOI: 10.1039/C7SM01079F. Copyright 2017 The Royal Society of Chemistry (RSC).

Hwang, M. Y., Kim, S. G., Lee, H. S., and Muller, S. J., "Elastic particle deformation in rectangular channel flow as a measure of particle stiffness." In preparation.

2.1 Introduction

This chapter describes the methods used to fabricate microfluidic devices and run microscale experiments examining suspensions. This includes fabrication of polydimethylsiloxane (PDMS) microfluidic devices, microparticle generation, particle characterization, and flow experiments using the generated suspensions. Experimental methods for the work with wormlike micellar solutions, including details on rheological characterization and flow visualization, are discussed in Chapter 5.

2.2 Generating Particles

2.2.1 Microfluidic Device Fabrication and Experimental Set-up

Microfluidic devices were fabricated from polydimethylsiloxane (PDMS) with standard soft lithography methods. Inlet and outlets were punched using a 16G blunt tip needle. 0.020" Tygon tubing was inserted and connected to 23G blunt tip needles, which were then threaded onto plastic syringes (BD 1 mL or 3 mL). Flow was controlled using three syringe pumps (two Harvard Apparatus PHD 2000 and one Harvard Apparatus Picoplus).

2.2.2 Alginate Hydrogel Particles

For spherical alginate particle generation, 0.2 to 2 wt% sodium alginate (Modernist Pantry) was dissolved in nanopure water for the aqueous-phase solutions. Oil-phase solutions were made of 1-undecanol (Spectrum Chemical) and 0.1 to 0.5 wt% calcium iodide (Sigma-Aldrich). When softer cored alginate particles were generated

by sheathing a viscous central stream, the viscous aqueous stream was 25 or 50 wt% glycerol in nanopure water. For visibility of the final alginate microparticles, 0.025 v/v% 1 μm fluorescent polystyrene spheres (Fluoro-Max™ green fluorescent polymer microspheres) or 0.67-2 wt% commercially available water soluble paint (Crayola) was added to the aqueous alginate solution. For visualization of alginate concentration gradients, 25 wt% of the alginate was replaced with a fluorescein-labeled alginate (low viscosity alginate fluorescein, Creative PEGWorks). All spherical alginate particles were collected in a pure 1-undecanol quenching bath before being rinsed with water.

2.2.3 pNIPAM Particles

For pNIPAM particle generation, the aqueous phase was composed of 7.92 wt% NIPAM monomer (N-isopropylacrylamide, Sigma-Aldrich), 0.15-1.2 wt% crosslinker (N,N'-methylenebisacrylamide, Sigma-Aldrich), and 1 wt% initiator (ammonium persulfate, Sigma-Aldrich) in water. Drops of the monomer solution were produced in an oil phase made of 1 wt% polyglycerol-3 polyricinoleate and sorbitan isostearate (Radia 7887, Woosung CNT) in heavy paraffin oil (EMD Millipore); 1 wt% accelerator (N,N,N',N'-tetramethylethylenediamine, Sigma Aldrich) in paraffin oil was introduced after the drops were formed to make pNIPAM hydrogel microparticles. All solutions were degassed under vacuum for 10 minutes, then purged with nitrogen and used immediately.

2.2.4 Non-spherical Alginate Particles

Non-spherical alginate particles were generated by allowing 1.0 and 1.5 wt% aqueous alginate droplets, generated with the same flow-focusing device design as the spherical particles, to fall into an external 20 mL aqueous bath containing 15 wt% barium acetate (Spectrum Chemical). For these non-spherical particles, 10-70 wt% glycerol was used to change the viscosity of the bath and change the resulting particle shape.

2.2.5 Inertial Effects During Particle Generation

Inertial effects were negligible for all particle generation techniques. The continuous phase flow rate per channel $q_c/2$ in a device with a height of 140 μm ranged from 279 to 303 μL/hr, and the dispersed phase flow rate q_d ranged from 5 to 100 μL/hr. We define Reynolds number for the continuous phase as:[27]

$$Re_C = \frac{\rho_C q_c}{h\mu_c} \qquad \text{(Equation 2-1)}$$

where ρ_C and μ_c are the continuous phase density and viscosity. Re_C was between 0.052 and 0.056 if only accounting for the drop formation region, and $0.10 < Re_C < 0.12$ in the gelation region. Similarly, the continuous phase Reynolds number in a device with a height of 70 μm is 0.074 during drop formation and 0.15 during gelation.

2.3 Flow Visualization

Flow visualization during microparticle generation, for characterization, and during onfined particle flow experiments were conducted using brightfield microscopy. Two microscopes were used: a Nikon OPTIPHOT-POL and a Leica DMIRE2 inverted microscope with an external light source (Leica EL6000). The alginate concentration, characterized by intensity of fluorescence from fluorescently labeled alginate, was imaged using a confocal microscope (Carl Zeiss Inc, LSM710). Videos were taken with a high speed camera (Vision Research, Phantom Miro M310) at capture rates between 24 and 1000 fps during particle generation and between 50 and 8000 fps with an exposure time of 30 μs during confined particle flow. Image analysis for particle characterization was done with ImageJ (NIH) and MATLAB (MathWorks).

2.4 Characterizing Particle Moduli with Capillary Micromechanics

Particle shear (the ratio of shear stress to shear strain) and compressive (the ratio of an applied pressure increase to the resulting decrease in volume) moduli were obtained by applying a range of hydrostatic pressures on a particle at the tip of a tapered microcapillary and analyzing the resulting particle deformation via a force balance on the particle, a method introduced by Guo and Wyss.[124] 1.2 to 1.5 mm diameter glass capillaries were pulled using a Sutter P-30 micropipette puller. The glass capillary was attached to flexible Tygon tubing with a 1/16 inch inner diameter and attached to the bottom of a petri dish filled with water. The hydrostatic pressure p was controlled by altering the height of the inlet reservoir. A schematic of the set-up, with sample images of a trapped deformable particle, is shown in Figure 2-1.

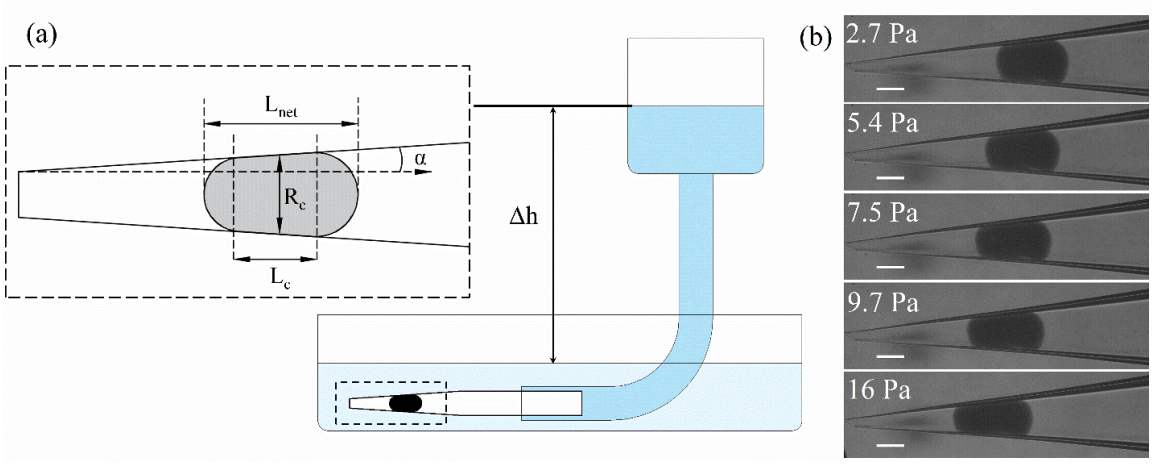

Figure 2-1. (a) Schematic of tapered capillary set-up for measuring particle shear and compressive moduli, with an inset of the deformed particle with relevant variables. (b) Sample pNIPAM particle, dyed with ink, trapped in the taper at five different hydrostatic pressures. Scale bar indicates 100 μm.

Guo and Wyss determined that for a particle of initial radius R_0, the radial strain ($\varepsilon_r = (R_c - R_0)/R_0$) and longitudinal strain ($\varepsilon_z = (L_c - R_0)/R_0$) can be related to the average wall pressure by balancing the pressure-induced external stresses on the particle with the internal elastic stresses:

$$p_{wall} = \frac{1}{\gamma_f \cos\alpha + \sin\alpha} \frac{R_c}{2L_c} p \qquad \text{(Equation 2-2)}$$

where γ_f is the friction coefficient, α is the taper angle of the capillary, p is the applied pressure, and L_c and R_c are the length and radius of the portion of the particle that is in contact with the taper walls (Fig. 2-1(a)), to obtain compressive modulus K (Equation 2-3) and shear elastic modulus G (Equation 2-4).

$$K = \frac{\frac{1}{3}(2p_{wall} + p)}{2\varepsilon_r + \varepsilon_z} \qquad \text{(Equation 2-3)}$$

$$G = \frac{\frac{1}{2}(p_{wall} - p)}{\varepsilon_r - \varepsilon_z} \qquad \text{(Equation 2-4)}$$

Before applying the analysis to newly generated particles, the method developed by Guo and Wyss was verified with commercially available 2% agarose beads (GoldBio). Representative plots for obtaining the shear and compressive moduli for a 2% agarose bead using this method are shown in Figure 3. The mean and standard deviation of the shear modulus was 15.0 ± 2.9 kPa and of the shear modulus was 18.1 ± 7.2 kPa (n = 7). The compressive modulus is more commonly reported in literature, with comparable values ranging from ~ 14 kPa (obtained with bulk 2.0% agarose gels using AFM[125] and stress-relaxation tests[126]) to 38 kPa (unconfined compression[127]). The shear modulus is also comparable to the range of 10-20 kPa obtained in a 0.1 to 120 Hz frequency sweep using a dynamic mechanical analysis (DMA).[128]

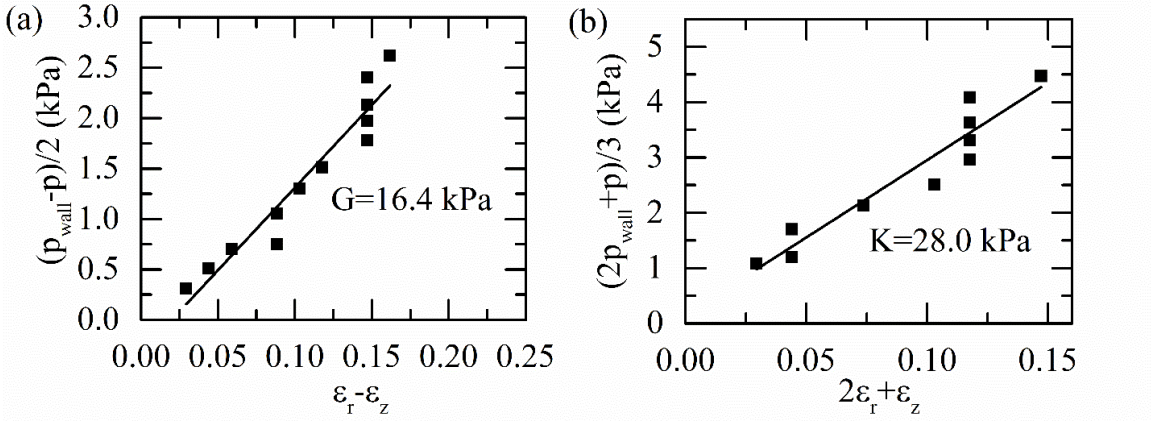

Figure 2-2. Sample plot used to determine shear modulus of commercially available 2% agarose particles (GoldBio). (a) Characteristic stress for shear deformation, (p_{wall} - p)/2, as a function of ε_r-ε_z, resulting in a slope of 16.4 kPa, the shear elastic modulus G. (b) Characteristic stress for compression, ($2p_{wall}$ + p)/3, as a function of $2\varepsilon_r+\varepsilon_z$, resulting in a slope of 28.0 kPa, the compressive elastic modulus K.

2.5 Flow Experiments for Confined Particle Deformation

2.5.1 Experimental Set-up

pNIPAM particles made with 0.15 wt% and 0.5 wt% crosslinker were examined in confined flow. The particles were nearly monodisperse in size; for a typical batch, the mean particle diameter μ was 249 μm and the standard deviation σ of the particle diameters was 19 μm, resulting in a polydispersity of 1.006, defined as polydispersity index, $PDI = 1 + (\sigma/\mu)^2$. Particles used in the present experiment were characterized by mean diameters of 249 ± 19 μm for the softer particles (n = 92) and 241 ± 13 μm for the stiffer particles (n = 78). The pNIPAM particles were suspended in a solution of de-ionized water with 10 wt% polyethylene glycol (PEG) (M_W = 8000 g/mol, Sigma-Aldrich).

The suspensions were flowed through glass capillaries with rectangular cross sections (width w=400 μm, height h=800 μm, and 100 mm long, VitroCom) that were attached to flexible Tygon tubing with 1/16 inch inner diameter using a fast curing two part epoxy (Devcon 5 Minute Epoxy, ITW Devcon, Danvers, MA). 3-mL plastic syringes threaded with 22-gauge plastic dispensing tips were inserted into the tubing. The flow was controlled with a syringe pump (Harvard Apparatus, PHD 2000). For better visualization, the glass capillaries were submerged in glycerol to match the refractive index, and the pNIPAM particles were dyed with blue ink (Pilot blue-black fountain pen ink) by allowing the particles to sit 10-20 minutes in the dye, and then centrifuging and exchanging the dyed water with deionized water. Figure 2-3 shows representative images of the dyed particles in the rectangular channels at different flow rates. Images were taken at the central plane of the channel (~400 μm from the bottom wall), with a measurement depth of ~10 μm (calculated with the depth of field equation from Inoué and Spring[129]). To check the reversibility of the deformation, the suspension was injected forward at 400,000 μL/hr, then immediately withdrawn backward at 10,000 μL/hr, all of which was captured in a single video. Each deformed particle in the first half of the video was then matched with its corresponding relaxed state in the reversed flow.

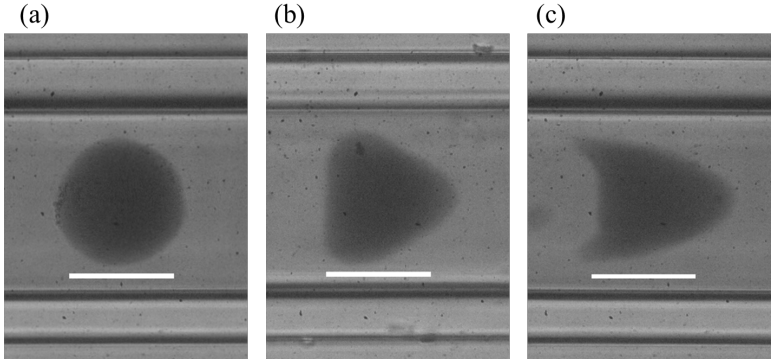

Figure 2-3. 0.15 wt% crosslinker pNIPAM particles observed in channel flow at shear rates of (a) 8.1 1/s, (b) 163 1/s, and (c) 326 1/s. Flow direction is left to right, and the scale bar is 200 μm in each image.

2.5.2 Image Analysis for Shape Deformation

For optimal analysis, the frame rate used to capture movies at each flow rate was selected to produce 8 to 20 images per particle while the particle remained within the field of view. Fig. 2-4(a) shows a single image of a particle. For the stack of images for each particle, ImageJ (NIH) was used to subtract a background image, implement an automatic binary thresholding using Otsu's method,[130] and calculate the particle centroid for each individual frame. Using MATLAB (MathWorks), each frame was then shifted so that the particle was centered in the image. The intensities of each frame's individual pixels were then summed to obtain a representative single image for the movie (Fig. 2-4(b)). The edge contour was detected using the Sobel operator, and a cubic spline fit was then interpolated (Fig. 2-4(c)).

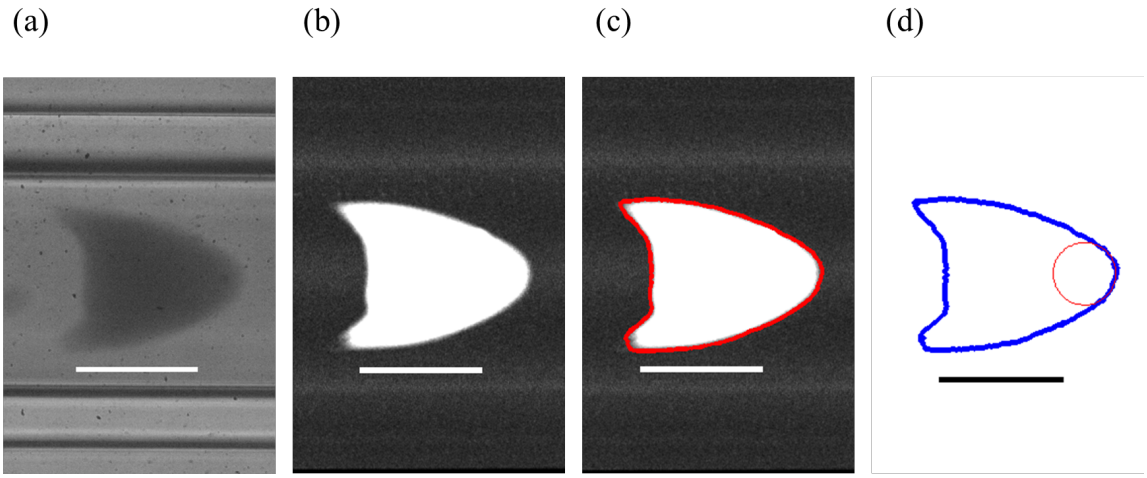

Figure 2-4. Edge fitting procedure for a sample image. (a) a single raw image (b) after background subtract and summing the intensities (c) Sobel edge detection and cubic spline fit (d) radius of curvature circle fitting at the front tip. The scale bars are 200 μm in each image.

Figure 2-5 shows a schematic illustrating the parameters used to characterize the deformation, which include the maximum axial length L_{max}, maximum radial (transverse) length R_{max}, and the minimum axial length L_{dimp} once the shape becomes concave at the rear. The radius of curvature R_C was determined for the front tip of the particle by fitting a circle to the cubic spline fit (Fig. 2-4(d)). Using the cubic spline fit, the area of the observed shape A was calculated with MATLAB's polyarea function (discretized Green's Theorem), and the perimeter P was calculated from the distance between 2500 vertices from the fit. For any shapes that a cubic spline could not resolve well, ImageJ was used to automatically threshold (Otsu's method) and convert the summed image to binary, and area and perimeter were then determined using the built-in particle analysis function. The ImageJ built-in perimeter function calculates edge length based on the pixels, counting each edge pixel as 1 and each corner pixel as $\sqrt{2}$. This method was more sensitive to image noise and edge roughness resulting from the binary threshold selection. The overall particle deformation was quantified by several non-dimensional parameters: non-dimensional radius of curvature R_C/R_{max}, the dimple

depth $D_{dimp} = (L_{max}-L_{dimp})/L_{max}$, the elongation $E = L_{max}/2R_{max}$, and circularity C as defined in Equation 2-5, which is the two-dimensional equivalent to the reduced volume used to characterize vesicles. The confinement of the particle is defined as $\alpha=2R_{max}/w$.

$$C = \frac{4\pi A}{P^2} \qquad \text{(Equation 2-5)}$$

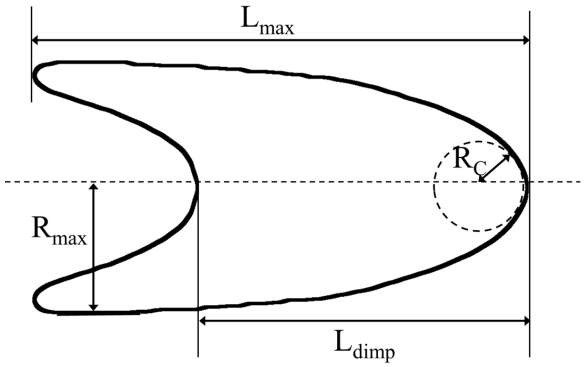

Figure 2-5. Schematic of a deformed particle with the relevant parameters indicated. L_{max} is the longest axial length from tip to tail, L_{dimp} is the axial length from the center of the dimple to the tip, R_{max} is the maximum radial distance from the shape centerline, and R_C is the radius of curvature at the tip.

3 Generation and Characterization of Monodisperse Deformable Alginate and pNIPAM Microparticles with a Wide Range of Shear Moduli

3.1 Abstract

Monodisperse particles of varying size, shape, and deformability were produced using two microfluidic strategies. For both strategies, monodisperse emulsion droplets of a crosslinkable solution were generated via flow-focusing. Subsequently, droplets were crosslinked either on chip or in an external bath. On-chip gelation resulted in spherical particles; varying the degree of crosslinking varied the deformability systematically. The optimized flow-focusing device design separated the production of monodisperse aqueous alginate droplets and the on-chip introduction of crosslinking ions. Two features were then adapted to target softer particles: the dispersed-phase design and the polymer choice. The alternative design used a sheathed dispersed phase, with the polymer solution surrounding an unreactive viscous core, which generated alginate particles with a softer core. Poly(N-isopropylacrylamide) (pNIPAM) allowed access to a broad range of moduli. The resulting spherical particles were characterized using capillary micromechanics to determine the shear (G) and compressive (K) moduli. Particles with G=0.013 kPa to 26 kPa and K=0.221 kPa to 34.9 kPa were obtained; the softest particles are an order of magnitude softer than those previously reported.[131] The second approach, based on earlier work by Hu *et al*.,[31] produced axisymmetric, non-spherical particles with fore-aft asymmetry. Alginate drops were again formed in a flow-focusing device but were crosslinked off-chip in an external gelation bath. By changing the bath viscosity, crosslinker concentration, and outlet height, the falling droplets deformed differently during gelation, resulting in a variety of shapes, such as teardrop, mushroom, and bowl shapes.

3.2 Introduction

Microparticles have a diversity of applications; depending on the size, shape, and material, they can be used in drug delivery, cell encapsulation, biosensing, and cell separation.[132–134] Suspensions of particles used for these applications have properties and flow dynamics that vary widely. For example, previous studies have shown that lateral migration of suspension components occurs in flow and is driven by a range of parameters including particle rigidity,[135] suspension concentration,[53] Reynolds number,[59,68] and particle shape and size.[47] However, how each of these parameters—and their combination—affect migration is not fully understood. The effects of each property can be investigated in isolation by developing a library of fully characterized, monodisperse soft particles; this library facilitates systematic studies of suspension dynamics.

Generating monodisperse particle populations is key to controlling and characterizing size, a parameter that affects migration behavior. A wide range of microfluidic systems generate monodisperse emulsion drops on the order of tens or hundreds of microns in diameter,[26,43,136,137] which are often used as precursors to microparticles.[138] A particularly versatile strategy for drop generation is a flow-focusing geometry, a schematic of which is shown in Figure 3-1.[26,27,40–43] The phase to be dispersed into a drop is in the center channel. Flow of the continuous phase, in the two outer channels, exerts shear stress on the dispersed phase, forcing it into a thread that breaks into drops. This study uses a planar flow-focusing geometry to generate a broad range of particles of varying size, deformability, and shape.

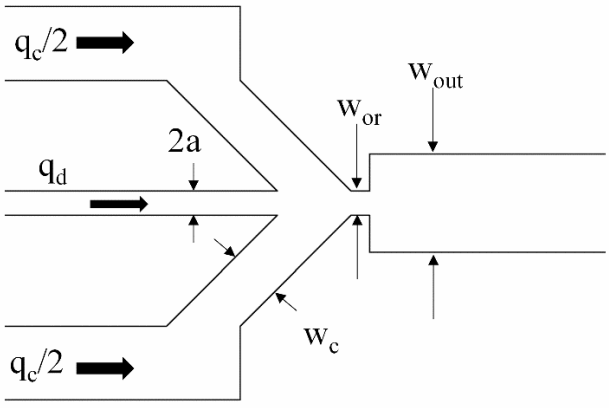

Figure 3-1. Flow-focusing geometry. Continuous phase enters in the channels at a flow rate of q_c and pinches the dispersed phase (flow rate q_d) into drops at the orifice, with a width of w_{or}.

The drop formation regime is dependent on the capillary number (Ca), defined for flow-focusing geometries by Anna and Mayer[27] as:

$$\mathrm{Ca} = \frac{\mu_c q_c a}{\sigma h \Delta z}\left(\frac{1}{w_{or}} - \frac{1}{2w_c}\right) \qquad \text{(Equation 3-1)}$$

where μ_c [Pa·s], q_c [m^3s^{-1}], a [m], σ [N/m], h [m], Δz [m], w_{or} [m], and w_c [m] are the continuous phase viscosity and flow rate, half the dispersed phase channel width (see Figure 1), interfacial tension, device height, distance from the downstream end of the dispersed phase channel to the orifice entrance, width of the orifice, and width of the continuous phase channel, respectively. At low Ca (< 0.5), drop formation is in the squeezing or geometry-controlled regime, where droplets are formed upstream of or in the orifice. At Ca~0.5, in the presence of surfactants, thread formation occurs, resulting in a thin thread of liquid between the larger droplets formed. At Ca ~ 1-3, drop formation transitions to the dripping regime inside or slightly beyond the orifice. At Ca>~5, jetting occurs, where a jet of liquid forms before droplets are produced well downstream of the orifice.[27,40] The experiments in our study remain in the squeezing regime for optimal control of drop formation and monodispersity.

To generate microparticles of a desired size, control of the initial emulsion drop is vital. Drop size depends on several parameters, including the continuous-phase flow rate, the characteristic length scale of the device, the ratio of the dispersed to continuous phase flow rates, and viscosity ratio of the two phases.[40,41] The first two parameters, flow rate and characteristic lengths, scale with the capillary number. Droplet diameter d decreases with Ca, as $d \propto Ca^{-1/3}$.[40] The volume of the drop V_d is also related to the flow-rate ratio of the dispersed to continuous phases $\varphi = q_d/q_c$ in a manner that depends on the model used to determine droplet breakup: $V_d \propto \varphi^1$ in rate-of-flow controlled drop formation or $V_d \propto \varphi^3$ in a shearing model.[41] In general, to generate smaller drops, the flow-rate ratio and length scale of the device should be small.

Using flow focusing as a basis, it is straightforward to make monodisperse deformable particles of controllable properties by crosslinking monodisperse emulsion drops containing polymers. Alginate, in particular, is well studied both in the macro- and microscale as a platform for drug delivery, food products, and cell encapsulation.[139,140] Alginate is a naturally occurring polysaccharide made up of two monomers, β-D-mannuronic acid (M) and α-L-guluronic acid (G). Gels form by the "egg-box" model, where the G residues pair up around divalent cations (Fig. 3-2);[141] consequently, the ratio of M to G residues and the sequence of the residues will affect the gel properties. Because alginate is derived from sea algae, the ratio of M to G varies with the organic source material. Resulting alginate hydrogel properties depend on the algae type and the vendor.[142–145] Bulk samples have resulted in shear moduli ranging from 0.2 to 50 kPa;[146–148] the moduli vary with alginate source and concentration, crosslinker type and density, and the presence of other ions.[142,146,149]

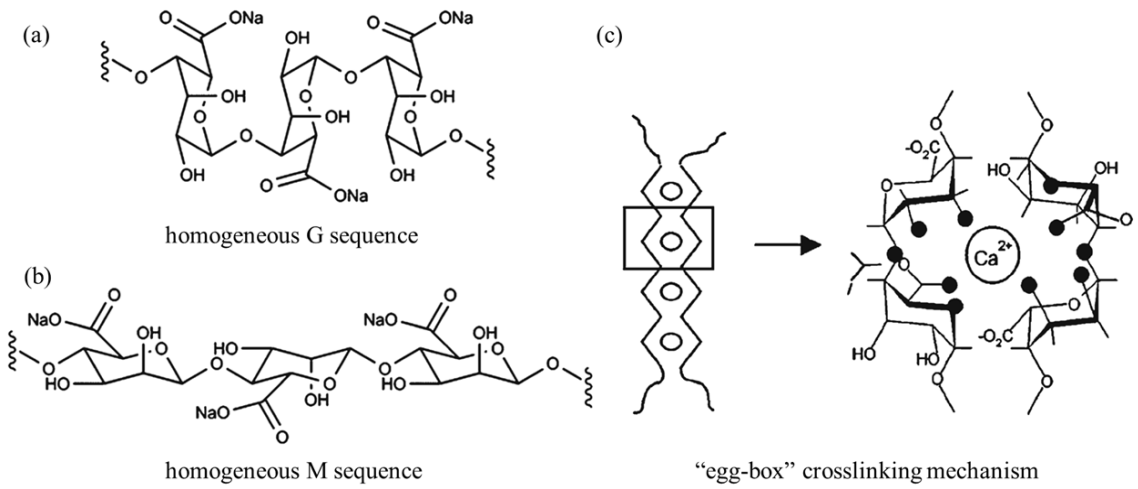

Figure 3-2. Sodium alginate sequences with (a) homogeneous G residues and (b) homogeneous M residues. (c) Illustration of the "egg-box" mechanism showing the interaction between the Ca^{2+} ion and the G residues. Modified from Fu *et al.*[144]

Monodisperse alginate microparticles are easily formed by crosslinking monodisperse aqueous sodium alginate drops with divalent cations, such as barium or calcium, and microfluidic production of alginate microparticles is well established.[29,150–152] In these published designs, the crosslinking cations are introduced on-chip in the continuous oil phase while the dispersed phase is an aqueous alginate solution. For example, in a design developed by Zhang *et al.*, aqueous sodium alginate is introduced as the dispersed phase in a flow-focusing device.[29] The undecanol oil phase introduced in the continuous phase channels has a low concentration of calcium iodide (CaI_2), which diffuses into and gels the emulsion drop as it moves down a long channel, resulting in spherical alginate microparticles. Although bulk alginate gel moduli have been widely characterized for a range of alginate concentrations, a systematic study of moduli in microparticles has not been performed. We are interested in quantifying the range of deformabilities obtainable with alginate microparticles, particularly the minimum. In addition, the flow-focusing device may require modifications for protracted particle generation, as long-term exposure of the alginate stream to crosslinking ions may result in inconsistent drop formation.

As alginate gel is limited in accessible moduli, different schemes were examined to obtain softer particles. The first approach involves changing the device design to modify the particle structure. Capsules consisting of a crosslinked polymer membrane around a liquid core are commonly generated with double emulsion templates, where a single drop consists of an inner droplet of fluid (core) emulsified in a thin layer of a middle fluid (shell); the middle fluid is then polymerized.[134,153] Double emulsions can also be used to generate core-shell particles, where both the core and the shell are solid.[154] The microfluidic devices needed to fabricate double emulsions, however, are sensitive to wetting and often need careful control of the hydrophobicity of the surfaces. Here, we have examined a route to generating lower shear moduli

alginate particles by introducing a softer core without switching to a double emulsion device.

An alternate route to more deformable particles is to use different polymer systems, such as poly(N-isopropylacrylamide) (pNIPAM). pNIPAM hydrogels are particularly interesting due to their thermal sensitivity: pNIPAM gels are swollen and hydrophilic at room temperature but shrink and become hydrophobic above a critical temperature.[155,156] Because they can be modified to be responsive to other stimuli,[157–159] pNIPAM hydrogels are used for a wide range of applications, including sensors, drug delivery, and color-tunable crystals. pNIPAM is straightforward to synthesize by free-radical emulsion polymerization,[160] although more difficult to work with than alginate. It can also be used to generate microparticles and has the potential to make thermally responsive microparticles.[30,161] Because pNIPAM is chemically synthesized, rather than naturally occurring, the chemistry is better defined and can be produced with a broader range of moduli than alginate.[30,162] In addition to obtaining softer particles, switching polymer systems also confirms the universality of the flow-focusing device previously used to generate solid alginate particles.

As controlling the mechanical properties of microparticles is relevant for determining their final application, quantifying the range of accessible moduli is crucial. The deformability affects the viability of the gel as a potential substrate for encapsulating cells, as the stiffness and material of the gel matrix can affect cell shape, stem cell differentiation, and stem cell function regulation.[163–165] In addition, mechanical properties of suspension components can significantly impact the bulk suspension properties such as viscosity[166] and also the behavior of the components themselves in flow.[56,65] However, experimentally determining the deformability of ~10-100 μm sized particles individually is not straightforward. For cells and other micro-sized objects, methods for determining shear or bending moduli include atomic force microscopy (AFM),[86] micropipette aspiration,[87,88] and optical stretching.[89] The majority of these techniques result in a localized modulus strongly affected by the particle surface, and the resulting measurements vary based on the technique used. A more recent method developed by Guo and Wyss uses capillary micromechanics to determine the shear and compressive moduli of soft particles.[124] When a particle is trapped in the tip of a tapered microcapillary and there is no flow, the applied pressure difference is balanced by the elastic stresses in the particle. This method differentiates the shear and compressive moduli while measuring them simultaneously and provides an effective modulus for the entire particle.

While spherical microparticles are straightforward to generate, various techniques have been studied to generate non-spherical microparticles. Methods include two-step generation where emulsion drops are formed then gelled while deforming externally,[31,167] stop-flow lithography,[168,169] gelation in geometrically-controlled confinement,[32,170] and transient liquid molding methods.[171,172] A two-step process introduced by Hu *et al*. leverages falling drop dynamics to deform emulsion droplets as they fall into an external bath containing crosslinking ions.[31] By changing the properties of the bath, the shape of the resulting particles was altered. The parameters unique to the external gelation bath set-up included the viscosity of the

gelation bath, addition of surfactant, crosslinking ion concentration, and the height of tubing exit in relation to the bath interface, all of which affected final particle shape. This design is particularly interesting due to its uncomplicated set-up, which uses a standard emulsion drop generation microfluidic device before the external gelation bath; however, the particles are limited to the axisymmetric shapes that can result from falling drop dynamics.

The main objective of this work is to obtain a library of monodisperse particles of varying but controllable size, shape, and deformability. We first examine the versatility of a basic flow-focusing geometry by considering an alginate and a pNIPAM system and optimizing the on-chip crosslinking device for long-term drop formation and control of particle properties, particularly size, targeting final particle sizes similar to biological cells and larger (diameter ~ 10 to 100 μm), with an upper limit determined by the length scales of the microfluidic devices. The minimum shear modulus obtainable with solid polymer microparticles is also investigated using the capillary micromechanics approach of Guo and Wyss,[124] with a target shear moduli on the order of 10 to 100 Pa to allow future studies of the deformation of soft particles in high Ca flows in microchannels. We also briefly consider off-chip gelation using the approach of Hu *et al*.[31] to explore control of particle shape. The library of particles will ultimately be useful for a broad range of studies of suspension dynamics and for model studies of cell separation based on modulus, size, and shape.

3.3 Results and Discussion

3.3.1 Alginate Particles

As monodisperse alginate microparticles have been generated by Zhang *et al.*, we based our initial on-chip design on their flow-focusing device,[29] shown in Figure 3-3(a), which generates particles with a reported polydispersity of 3.8%. Two values are used to quantify polydispersity of the generated alginate particles: polydispersity index, $PDI = 1 + (\sigma/\mu)^2$, and coefficient of variance, $CV=(\sigma/\mu)*100$,[132] where μ is the mean and σ is the standard deviation of the distribution of particle diameter d. On prolonged use of this initial device, however, the resulting particles had a bimodal distribution, as shown in Figure 3-4, and a high polydispersity, with a PDI of 1.05 and a CV of 22%. Upon careful examination, the edges of the alginate dispersed phase tip were seen to gel, resulting in a pseudo-jetting phenomenon. Figure 3-5 illustrates this behavior as it developed over time. Initially, drop formation was in the squeezing regime (Figure 3-5(a)), but the slowly gelling interface of the alginate stream affected the drop generation, evident in Figure 3-5(b), showing the transition between the squeezing and pseudo-jetting regime at 30 minutes. After 60 minutes, the flow was fully in the new regime (Figure 3-5(c)), with the alginate-phase tip extending well downstream of the orifice. This phenomenon affected particle generation, especially when the flow transitioned slowly between regimes. To avoid the inconsistent drop formation that resulted from pseudo-jetting, a modified device was designed, where a second set of inlets was used to introduce Ca^{2+} to the system (Figure 3-3(b)). This modified design introduces the crosslinking agent after emulsion drops have been formed, preventing

early gelation of the dispersed phase stream. With this modified gelation-on-chip design, it was possible to generate reliably monodisperse spherical particles for periods of hours. A representative image and size distribution of a typical spherical particle population, with a polydispersity index of 1.001 and a coefficient of variance of 3.5%, can be seen in Figure 3-6. This size distribution is consistent with what is obtained with short time operation of the initial design (Figure 3-3(a)). The observed productivity of the modified device was 600-1000 particles/minute, depending on the flow rate ratio.

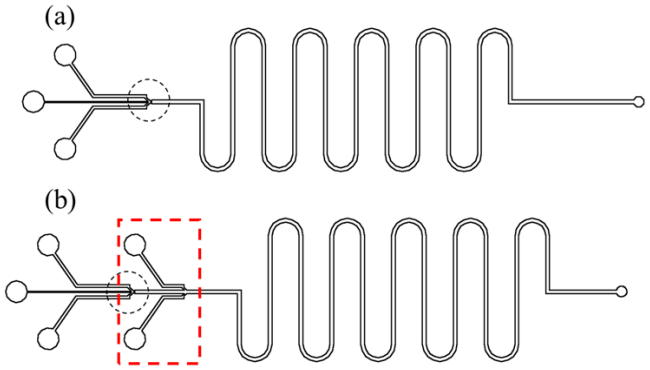

Figure 3-3. Gelation on a chip design: (a) based on Zhang et al.[29] (b) modified for long-term particle generation. The circled first junctions are similar to the flow-focusing orifice shown in Figure 3-1. The red box indicates the modification made to the original design, where a second set of continuous phase inlets are used to introduce the crosslinking Ca^{2+} ions.

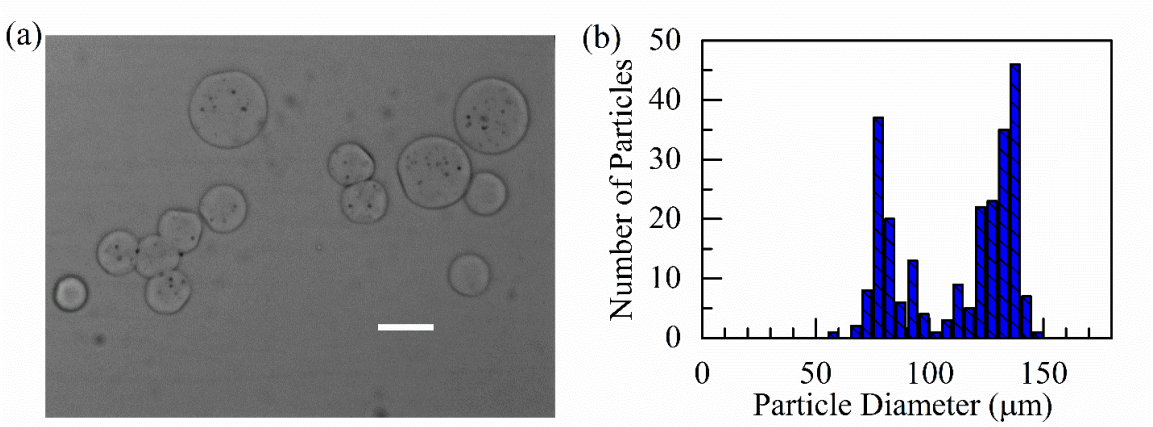

Figure 3-4. (a) Alginate particles generated with original literature design.[29] Scale bar indicates 100 μm. (b) Size distribution of generated alginate particles after 2 hours of collection.

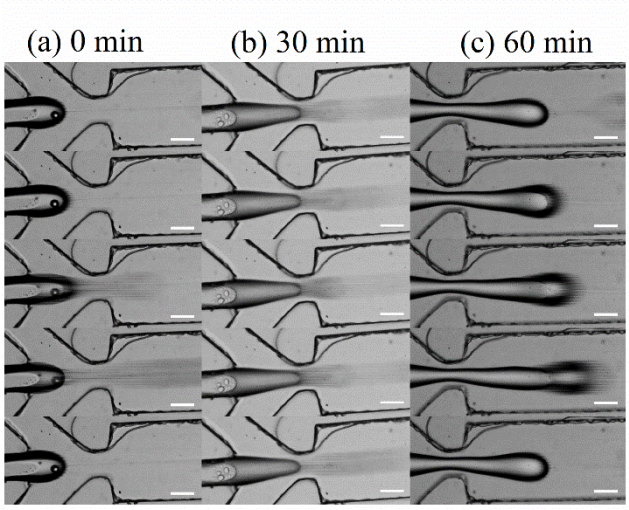

Figure 3-5. Development of drop formation over time after introduction of Ca^{2+} crosslinking ions. Time indicated is time after alginate begins to crosslink in the outlet. Frames in each column are ~0.03 s apart. Scale bars indicate 100 μm.

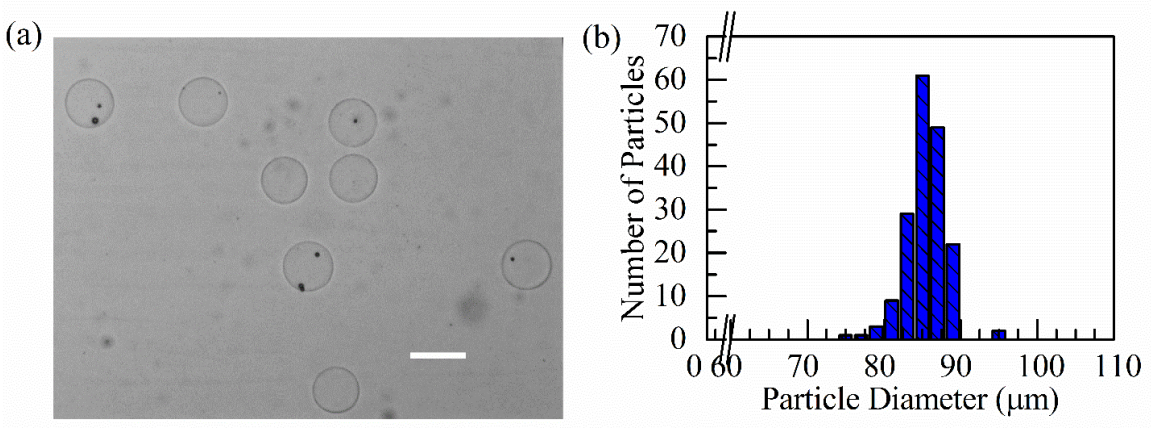

Figure 3-6. (a) Alginate particles generated with the modified design. (b) Distribution of generated alginate particles. Scale bar indicates 100 μm.

Literature on flow-focusing devices shows that reducing the ratio of dispersed phase flow rate to continuous phase flow rate reduces the drop size.[27,40] This trend was observed when the residence time and CaI_2 concentration were held constant, as shown in Figure 3-7(a). Due to the dependence of droplet size on viscosity ratio and capillary number and the altered flow-focusing geometry (Figure 3-1) used for particle generation, direct quantitative comparison of our results with literature is difficult. Using Anna and Mayer's definition of Ca (Equation 3-1), all Ca were ~ 10^{-2}, placing drop formation in the squeezing regime.[27] The volume of the drop formed, approximated by $V_d=4/3\pi(d/2)^3$, as a function of the flow-rate ratio $\varphi=q_d/q_c$ was fitted, yielding $V_d \propto \varphi^{0.66}$. This is comparable to the results in Nie *et al.*, where drop volume followed the rate-of-flow controlled break-up law $V_d \propto \varphi^1$ for lower viscosity ratios, while higher viscosity ratios reduced the dependence of volume on φ.[41] In addition to

flow-rate ratio, as Lee *et al.* noted,[40] the droplet size is proportional to the characteristic device diameter $D_h = 2w_{or}h/(w_{or} + h)$; consequently, by changing the height of the device from 140 μm to 70 μm, the particle diameter was also approximately halved (Figure 3-7(b)).

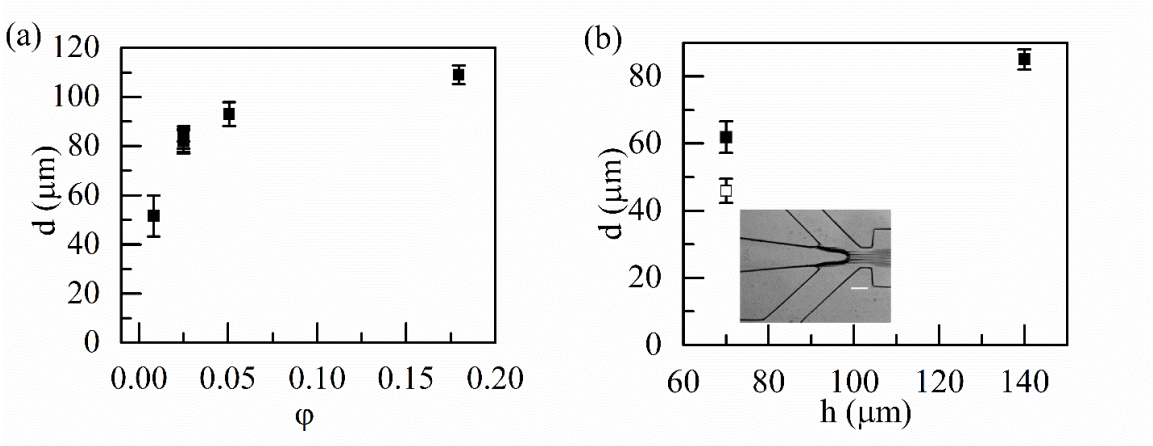

Figure 3-7. (a) Average particle diameter with varying flow rate ratio $\varphi=q_d/q_c$. (b) Average particle diameter as a function of device height. Open square indicates a tapered channel leading to the orifice, shown in the inset. Filled squares indicate standard device design (Fig. 3-1).

Although the particle size relationships were determined with 1 wt% alginate crosslinked with 0.5 wt% CaI_2, lower concentrations of alginate resulted in lower moduli. To obtain the minimum alginate possible, dispersed phases from 0.1 to 0.5 wt% alginate solutions were tested. Alginate particles of each concentration were crosslinked with 0.25 wt% CaI_2 to ensure that the particles fully gelled. Once the particles were rinsed with water, the vials were centrifuged and decanted to concentrate the solution, and then imaged. Using this method, the lowest concentration of sodium alginate for which resulting particles remained gelled when rinsed with water was 0.3 wt%; below this concentration, the particles appeared broken open or had dissolved altogether.

The shear elastic and compressive moduli for solid elastic alginate particles are shown in Table 3-1. The range of shear and compressive moduli is similar to literature results on bulk hydrogels; the 1 wt% alginate microspheres had G = 25.9 ± 7.5 kPa and K = 43.9 ± 8.7 kPa, which are comparable to the shear modulus ~25 kPa obtained with 1 w/v% high molecular weight alginate gel by Kong *et al.*[147] and the compressive moduli 25-58 kPa obtained with 0.9 wt% alginate crosslinked with a range of calcium carbonate concentrations.[173] The lowest concentration in the table, 0.3 wt% alginate, resulted in the lowest moduli obtainable with uniform alginate particles, with G = 1.3 ± 0.2 kPa and K = 2.8 ± 0.5 kPa. It is also important to note that the alginate particles degraded over time if stored in water; freshly made 1 wt% alginate particles had an average shear modulus of 25.6 kPa, but after being stored in water for six months, the

particles had an average shear modulus of 6.2 kPa. However, we saw little change in moduli over the time scale of one week. The degradation is most likely due to the diffusion of Ca^{2+} ions from the ionically crosslinked gel matrix.[174–176] As Bajpai and Sharma found, the introduction of monovalent cations, such as storage in a phosphate-buffered saline, can expedite the degradation due to the ion exchange process between sodium and calcium ions, causing calcium-alginate beads to dissolve in ~3 hours.[174] They concluded that the swelling of the gel and release of Ca^{2+} was diffusion controlled and followed a Fickian release pattern. Storage in a low Ca^{2+} concentration solution would prevent degradation over time.[146] Lastly, the moduli of alginate particles was not affected by moderately low concentrations of additives such as 1 μm rigid polystyrene spheres or commercially available water soluble paint, demonstrated by the three types of 0.5 wt% alginate particles in Table 3-1. This indicates that tracers or particles used for visualization do not significantly impact the mechanical properties of alginate hydrogels.

Table 3-1. Shear (G) and compressive (K) moduli for fully gelled, uniform concentration alginate particles. For each modulus measurement, the mean and standard deviation are given.

Sodium alginate concentration	G (kPa)	K (kPa)	n
1 wt%	25.9 ± 7.5	43.9 ± 8.7	9
1 wt%, stored for 6 months	6.2 ± 2.1	16 ± 3.6	7
0.5 wt%	6.1 ± 1.1	16.7 ± 4.8	10
0.5 wt%, 0.7 wt% paint	8.9 ± 2.4	9.7 ± 2.8	10
0.5 wt%, 1 μm spheres	7.7 ± 3.4	11.5 ± 2.2	10
0.3 wt%	1.3 ± 0.2	2.8 ± 0.5	8

3.3.2 Particles with an Alginate Concentration Gradient

Because the shear moduli of uniform alginate particles was limited to ~1 kPa and greater, non-uniform concentration particles, effectively a simplified core-shell design, were examined to target lower moduli. Deformable particles with softer cores were generated using a two-component dispersed phase. A viscous core of aqueous glycerol was surrounded by an aqueous alginate layer, and the entire aqueous stream was then pinched into emulsion drops at the flow-focusing junction (Fig. 3-8). The throughput of this design for the flow rates used ranged from 1000-1300 particles/minute. Due to the mixing that occurred as drops were pinched off, there was a gradient in the alginate concentration within the final particle. This can be seen in Figure 3-9, where the alginate was fluorescently labeled and the fluorescence intensity of the resulting particle was averaged azimuthally; the alginate concentration is higher at the edge and lower in the center of the gradient particle, whereas the fluorescence intensity is essentially uniform from the center to the edge of a homogenous particle.

This sheathing method generates softer particles with a gradient in alginate concentration. However, the particles are not capsules with a gelled shell and liquid center, as they do not wrinkle or deform noticeably in flow, or rupture and expel liquid when broken.

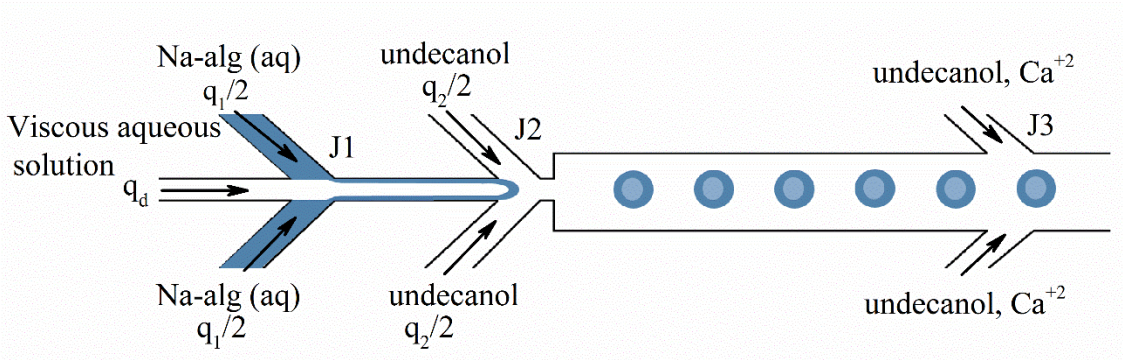

Figure 3-8. Schematic of flow-focusing device design with sheathing stream at J1, drop formation at J2, and introduction of the crosslinking ions at J3.

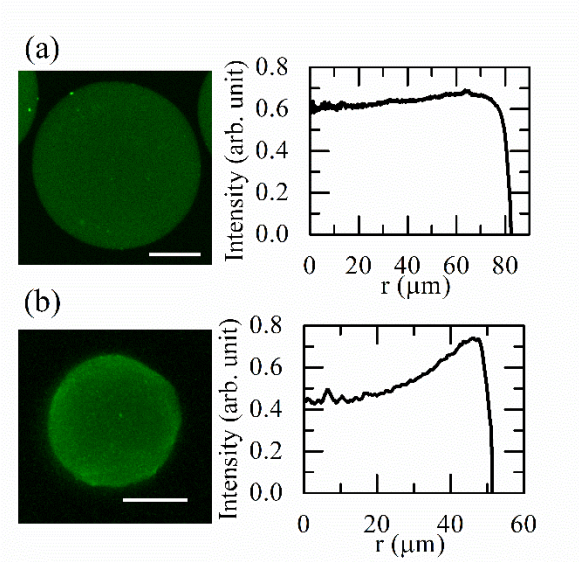

Figure 3-9. Confocal image and azimuthally averaged fluorescence intensity in arbitrary units across the particle radius r (μm), where the particle center is at r=0, for (a) homogeneous alginate particle and (b) soft-cored particle. Scale bar indicates 100 μm.

The alginate particles with a concentration gradient were softer than the fully gelled, uniform alginate particles, with a minimum effective shear modulus of 0.63 ± 0.1 kPa, which is half the minimum of 0.3 wt% alginate. Three factors contributed to the moduli: glycerol concentration in the viscous core, sodium alginate (Na-alg) concentration in the sheathing layer, and the ratio of the flow rates between the two solutions that made up the dispersed phase. As summarized in Table 3-2, as glycerol concentration or sodium alginate concentration increased, both G and K increased. The

flow rate ratio between the sheathing alginate layer (q_1) and the viscous core (q_d) effectively controlled the overall amount of alginate in the particle as well as the sheathing layer thickness. The lower the ratio q_1/q_d, the thinner the sheathing layer and the lower the overall alginate concentration. Consequently, a lower ratio resulted in a softer particle.

Table 3-2. Effective shear (G) and compressive (K) moduli for soft-cored particles with a gradient in alginate concentration. For each modulus measurement, the mean and standard deviation are given.

Na-alg concentration (wt%)	glycerol concentration (wt%)	q_1/q_d	Effective G (kPa)	Effective K (kPa)	n
1	50	1.0	3.1 ± 0.5	7.4 ± 1.8	10
1	25	1.0	2.3 ± 0.5	5.4 ± 1.3	10
1	50	0.5	1.5 ± 0.3	3.9 ± 0.2	9
1	25	0.5	1.2 ± 0.5	3.7 ± 1.6	9
0.5	25	1.0	0.99 ± 0.3	3.4 ± 1.6	6
0.5	25	0.5	0.63 ± 0.1	1.8 ± 0.2	10

3.3.3 pNIPAM Particles

In addition to changing the device design, a different polymer system was also examined to generate softer particles. pNIPAM hydrogel was selected due to its straightforward crosslinking chemistry[160] and moderately low bulk shear modulus of 1 to 10 kPa at room temperature.[30] The modified microfluidic design optimized for alginate particles (Fig. 3-3(b)) was successful in generating pNIPAM particles with 7.9 wt% monomer and varying concentrations of crosslinker from 0.15 to 1.2 wt% with size distributions comparable to those for alginate particles (Fig. 3-10). For the representative sample shown in Figure 11, the PDI was 1.0001 and the CV was 1.2%. This demonstrates the versatility of the optimized chip design, which needed no alteration between the two systems, both of which are based on water-in-oil emulsion drops. As the flow rate ratio was higher for pNIPAM particle generation, the throughput observed was also higher, ranging from 600 to 1800 particles/minute.

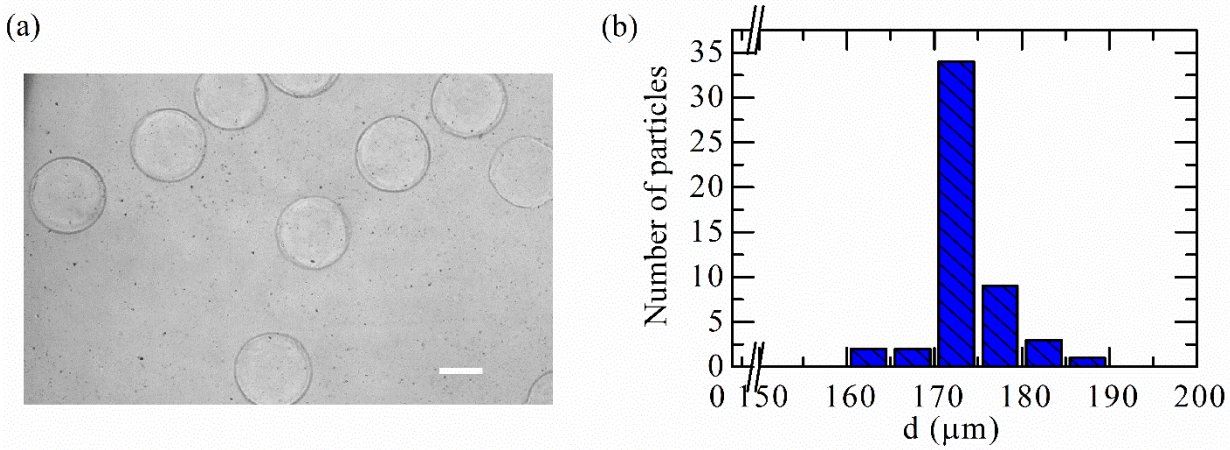

Figure 3-10. (a) Sample image and (b) size distribution of pNIPAM particles made with 7.9 wt% monomer and 0.9 wt% crosslinker. Average size is 172.9 μm, CV=1.2%, PDI=1.0001. Scale bar indicates 100 μm.

As shown in Table 3-3, pNIPAM particles are far more deformable than the previously generated particles, with moduli up to two orders of magnitude lower than 0.3 wt% alginate particles. A lower crosslinker density corresponded to a lower modulus, with all the shear moduli lower than the alginate moduli minimum. These highly deformable particles allow for higher differentiation (i.e., a broader range of Ca) among types of particles for suspension dynamics experiments. These moduli are lower than standard microparticle populations, which tend to have moduli ranging from ~1-100 kPa,[30,51,93] and one order of magnitude lower than the softest microparticles found in the literature, 0.225 kPa for poly(ethylene glycol) diacrylate nanoparticles generated by nanoemulsion[50] and 0.190 kPa for polydisperse poly(ethylene glycol) diacrylate microparticles.[131] A 0.15 wt% crosslinker pNIPAM particle trapped in a taper is shown in Figure 2-1, where notable deformation was observed as the applied pressure increased from 2.7 to 16 Pa. For contrast, Figure 3-11 shows a 0.5 wt% alginate particle at the same hydrostatic pressure as a 0.15 wt% crosslinker pNIPAM particle—the pNIPAM particle was much more dramatically deformed. Because the pNIPAM particles are covalently rather than ionically bonded, they do not seem to undergo the same degradation in moduli that the alginate particles do when stored in distilled water. pNIPAM particles characterized after eight months had comparable moduli to those measured within a few days of generation.

Table 3-3. Shear (G) and compressive (K) moduli for pNIPAM particles. For each modulus measurement, the mean and standard deviation are given.

Crosslinker wt%	G (kPa)	K (kPa)	n
1.2	0.221 ± 0.06	0.384 ± 0.08	11
0.9	0.096 ± 0.03	0.254 ± 0.09	10
0.6	0.041 ± 0.01	0.117 ± 0.04	10
0.15	0.013 ± 0.005	0.096 ± 0.05	13
0.15, stored for 8 months	0.013 ± 0.004	0.061 ± 0.02	10

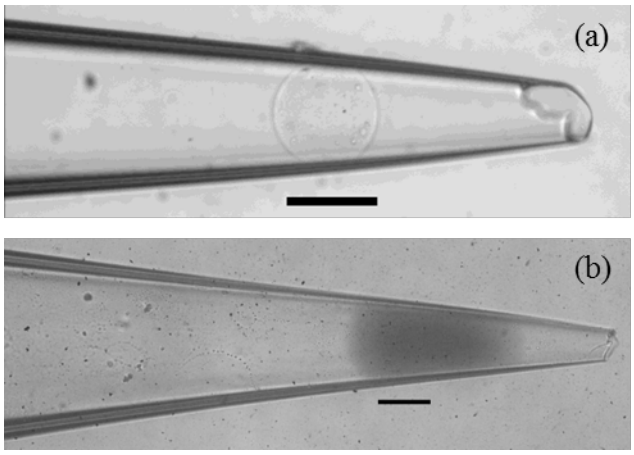

Figure 3-11. (a) homogeneous 0.5 wt% alginate particle and (b) 0.5 wt% crosslinker pNIPAM particle at an applied pressure of 98 Pa. Scale bar indicates 100 μm.

3.3.4 Axisymmetric, Non-spherical Alginate Particles

Non-spherical alginate particles were generated using an external gelation bath, based on the approach of Hu *et al.*[31] 1 wt% and 1.5 wt% alginate emulsion drops were generated in a flow-focusing device and dropped into an aqueous bath containing crosslinking ions of barium acetate ($Ba(OAc)_2$) (Fig. 3-12(a)). The productivity for non-spherical particle generation ranged from 150 to 600 particles/minute, which is lower compared to spherical particles because the flow rates were optimized to increase the spacing between exiting drops and avoid coalescence. By varying the bath viscosity using glycerol, crosslinking-ion concentration, and exit tubing height z, the emulsion drop deforms into different shapes as it gels. The resulting axisymmetric, non-spherical particles, including those with fore-aft asymmetry, are shown in Figure 3-12. Rather large increases in bath viscosity, from 1 mPa-s to 23.3 mPa-s, were investigated. Consistent with Hu et al.[31], we find that rather extreme changes in bath viscosity were needed to affect a change in the particle aspect ratio. We also varied the concentration of sodium alginate in the drop, and, as expected, lower alginate concentrations resulted in a modest enhancement of the effect of bath viscosity due to the lower viscosity of the alginate phase. Notably, the more viscous 1.5 wt% alginate emulsion drops may result in more exaggerated fore-aft asymmetry compared to the 1 wt% alginate (Fig. 3-12(b)). Changing tubing height relative to the bath interface proved more effective in changing drop shape; by varying the tubing outlet from 1 mm below the interface to 8 mm below the interface, we were able to change the particle shape from nearly-spherical to cap shaped. Furthermore, surface tension can affect the final shape of the particle, particularly with higher viscosity gelation baths. Even with the tubing outlet under the oil/water interface that forms, the emulsion drops occasionally remained entrained on the interface, rising along the edge of the tube as the interface does. This resulted in dimpled, non-axisymmetric, or otherwise asymmetric particles that were less uniform in shape, as the crosslinking occurred along the interface rather than

evenly (Fig. 12(d,e)). Overall, falling drop dynamics produced non-spherical microparticles that could be interesting for future studies.

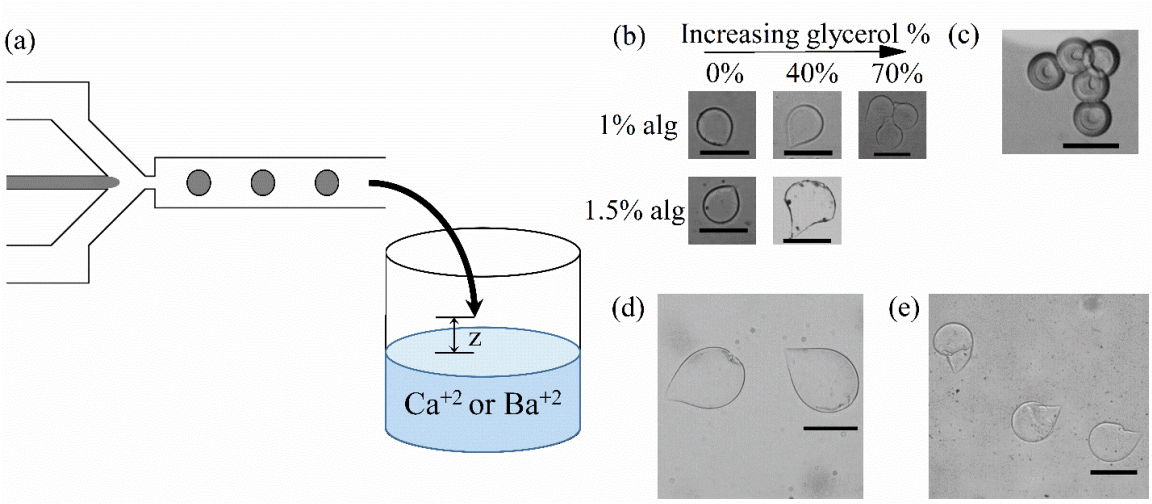

Figure 3-12. (a) Schematic of flow-focusing device leading to the external gelation bath. The images show resulting non-spherical alginate particles for: (b) Varying alginate concentration emulsion drops falling into external baths with 15 wt% $Ba(OAc)_2$ and varying glycerol concentrations, z=~0 mm. (c) 1.5 wt% alginate emulsion drops falling into an external bath with 15 wt% $Ba(OAc)_2$, 70 wt% glycerol, z= - 6 mm (d) 1.5 wt% alginate emulsion drops falling into an external bath with 15 wt% $Ba(OAc)_2$ and 40 wt% glycerol, with interfacial interactions where the drops linger on the interface (e) 1.5 wt% alginate emulsion drops falling into an external bath with 15 wt% $Ba(OAc)_2$ and 40 wt% glycerol, with interfacial interactions where the drops move along and rise up the interface.

Table 3-4. Experimental ranges of each varied parameter for alginate particle generation using an external gelation bath

Property	Parameter	Values examined
Bath viscosity	glycerol wt%	0 to 80
Exit tubing height	z [mm]	-6, 0, 5
Dispersed phase	alginate wt%	1.0, 1.5
Exit flow rate	q_c [μLh^{-1}]	1800 to 2200

3.4 Conclusions

In this study, we investigated approaches to producing libraries of monodisperse particles of controlled size, deformability, and shape. We have modified a standard flow-focusing design for on-chip drop generation and crosslinking to avoid gelling of the interface of the dispersed phase stream; this allows prolonged use of a single, reusable device. The modified design produced large populations of spherical, monodisperse particles for a range of device heights, flow-rate ratios, polymer and crosslinker concentrations, and for two different polymer systems (alginate and pNIPAM). A second modification to the design allowed the production of drops consisting of an unreactive viscous core sheathed in a layer of crosslinkable polymer solution. This design was tested with glycerol-water solutions as the core and sodium alginate solutions as the sheath; mixing of the two streams during drop pinch-off resulted in a gradient of alginate so that solid particles with soft, lightly-crosslinked cores (rather than capsules) were produced. These particles were softer than the original alginate particles but stiffer than the pNIPAM particles. Particle shear and compressive moduli were characterized via the capillary-micromechanics method of Guo and Wyss;[124] ultimately, particles were produced with shear moduli that varied over several orders of magnitude, from 0.01 to 26 kPa, and compressive moduli that varied from 0.1 to 35 kPa. The lowest moduli pNIPAM particles are the softest reported to date, with the advantage of also being monodisperse.[131] As the focus of this work has been to obtain the softest particles possible, the upper end of the range of accessible moduli was not explored further; however, more rigid alginate particles could easily be generated by increasing the alginate concentration. The use of a strategy proposed by Hu et al.,[31] in which drops are crosslinked in an external bath and drop dynamics are leveraged to control particle shape, was also explored with the alginate system. Collectively, a large library of particles has been generated, including spherical particles ranging from 45 μm to 121 μm in diameter, particles with shear moduli encompassing several orders of magnitude, ranging from 0.01 to 26 kPa, and non-spherical, fore-aft asymmetric particles.

3.5 Acknowledgements

This work was supported by a grant from the National Science Foundation (Award CBET 1066334). MYH was also supported through a National Science Foundation Graduate Research Fellowship. Research reported in this publication was supported in part by the National Institutes of Health S10 program under award number 1S10RR026866-01. The content is solely the responsibility of the authors and does not necessarily represent the official views of the National Institutes of Health.

4 Elastic Particle Deformation in Rectangular Channel Flow as a Measure of Particle Stiffness

Reproduced with permission from:

Hwang, M. Y., Kim, S. G., Lee, H. S., and Muller, S. J., "Elastic particle deformation in rectangular channel flow as a measure of particle stiffness." In preparation.

4.1 Abstract

In this study, we experimentally observed and characterized soft elastic particle deformation in confined flow in a rectangular microchannel. Hydrogel microparticles of poly(n-isopropylacrylamide) (pNIPAM) were produced using two different concentrations of crosslinker. This resulted in particles with two different shear moduli of 13.3 ± 5.5 Pa and 32.5 ± 15.7 Pa as measured by capillary micromechanics. Under flow, the particle shapes transitioned from circular to egg, triangular, arrowhead, and ultimately parachute shaped with increasing shear rate. The shape changes were reversible, and deformed particles relaxed back to circular/spherical in the absence of flow. The thresholds for each shape transition were quantified using a non-dimensional radius of curvature at the tip, particle deformation, circularity, and the depth of the concave dimple. The observed shapes were distinct from those previously reported in the literature for vesicles and capsules; the elastic particles had a narrower leading tip and a lower circularity. Due to variations in the shear moduli between particles within a batch of particles, each flow rate corresponded to a small but finite range of capillary number (Ca) and resulted in a series of shapes. By arranging the images on a plot of Ca versus circularity, a direct correlation was developed between shape and Ca and thus between particle deformation and shear modulus. As the shape was very sensitive to differences in shear modulus, particle deformation in confined flow may allow for better differentiation of microparticle shear modulus than other methods.

4.2 Introduction

The flow behavior of suspensions is complex due to the range of component properties, including concentration,[177] deformability,[50,82] size relative to the characteristic length scale of the flow,[47,178] and shape,[179,180] that affect component motion and interactions as well as the rheology of the overall suspension. For example, although a single rigid particle in flow with negligible inertia will not undergo lateral migration across streamlines due to the reversibility of Stokes flow, soft objects can

deform in flow, resulting in fore-aft asymmetric shapes that can migrate laterally.[82,181–183] By using sufficiently dilute suspensions, the mechanics of a single particle in flow may be examined, and the effects of properties such as shape and deformability may be studied independently, without component-component interactions or concentration effects.

The common soft objects used in suspension experiments—solid particles, capsules, and vesicles—can be differentiated. Here we focus on particles that are gelled and solid throughout, whereas capsules and vesicles have a liquid core. A capsule has a thin solid membrane surrounding the liquid, and the membrane can stretch while maintaining a constant internal volume. A vesicle has a phospholipid bilayer wall, where the membrane has a constant area even when taking on different conformations[184,185]. Because the forces driving deformation in flow depend on the component interface, the type of object affects the shapes that develop.[122] The forces driving deformation are characterized by the capillary number (Ca), defined as the ratio of the viscous shear force to the particle's restoring forces. As Ca increases, the viscous shear forces become more dominant, and the deformation increases. The primary restoring forces depends on object type, so the corresponding Ca definitions vary, e.g. for a vesicle Ca is the ratio of viscous to bending forces, characterized by the vesicle bending modulus[44] whereas for a capsule Ca is the ratio of viscous to elastic forces, characterized by the surface shear modulus of the membrane.[185] In this study, we focus on solid elastic particles deformation, for which

$$Ca = \frac{\mu\dot{\gamma}}{G} \qquad \text{(Equation 4-1)}$$

where μ is the viscosity of the suspending fluid, $\dot{\gamma}$ is the characteristic shear rate, and G is the particle bulk shear modulus.[186]

Flowing suspensions through confined channels, where the particle size is similar to the channel size, introduces wall shear. The resulting deformation is biologically relevant, as the motion and deformation of red blood cells in the microcirculation in capillaries plays a fundamental role in gas transfer.[187] Red blood cells change from standard biconcave disks to parachute, bullet, or slipper-like shapes in microcirculation *in vivo*[188] and also in microcapillary experiments *in vitro.*[189,190] In addition, the deformation and rupture of capsules and particles in capillary flow is relevant to drug delivery particle design; while targeted rupture of microcapsules is ideal for pulsed drug release, which entails a rapid release after a time lag,[191] understanding and controlling particle deformation to prevent rupture is important for diffusion-driven sustained drug release.[192]

Experimental and computational studies examining soft object deformation in flow have focused on those with liquid cores, including capsules and vesicles. Vesicles in shear flow exhibit different types of motion, similar to those seen in red blood cells: 1) tumbling, where the entire vesicle rotates periodically, 2) trembling, where the vesicle shape fluctuates asymmetrically and the vesicle orientation oscillates aperiodically, and 3) tank-treading, where the membrane rotates around the inner contents while the vesicle maintains a constant shape.[193–199] The transitions between

behaviors depend on parameters such as flow rate, vesicle reduced volume ν, and interior-to-exterior fluid viscosity ratio $\lambda = \eta_{in}/\eta_{out}$. Mader *et al.* experimentally examined the effect of changing the viscosity ratio on tumbling, noting that tank-treading occurs at lower viscosity ratios and tumbling occurs at higher viscosity ratios, with periodic rotation. They then compared their observations to the theory proposed by Keller and Skalak (KS),[200] finding reasonable agreement at low Ca; however, at high Ca>10, deformability effects are non-negligible and experimental results deviate from those determined by the KS model. Kantsler and Steinberg first experimentally observed trembling, occurring at high vesicle deformability with Ca ~1.[197] This oscillatory behavior was also computationally examined by Noguchi and Gommper, who called this mode the swinging mode and generated phase diagrams indicating the transition from tumbling to swinging.[199] Analytically, Misbah noted a behavior termed vacillating-breathing, where the orientation angle and shape deformation oscillated with the same period.[201] Deschamps *et al.*[202] concluded that tumbling and trembling behavior also appear in mixed flows, with vesicle shapes in the trembling regime that were very different from those predicted computationally for vacillating-breathing from Misbah.[201] With a phospholipid membrane and similar motion in flow, vesicles can be used as models for biological cells, e.g. red blood cells, so understanding vesicle flow behavior is relevant to a range of topics such as understanding blood rheology in microcirculation.

Capsules have also been studied in shear flow in a number of computational[203–211] and experimental[135,212–215] works, where deformation and orientation are characterized as a function of several parameters: initial capsule shape,[209] viscosity ratio of inner and outer fluids,[211] and membrane viscosity. Chang and Olbricht experimentally examined the behavior and breakup of macroscopic capsules in a Couette cell, noting that the deformation generally followed those from small-deformation theory,[216] but unlike theory, which proposes a steady shape, the capsule shape oscillated about a mean deformation.[212] They also found that capsule breakup occurred at the point of maximum extension in the membrane. The effect of initial capsule shape on capsule behavior was studied in a computational work by Ramanujan and Pozrikidis, which started with spherical, oblate, and biconcave capsules.[206] Initially spherical capsules undertook steady inclined ellipsoidal shapes above a critical shear rate while the membrane tank-treads. However, an initially non-spherical capsule had slight oscillations in deformation shape and orientation. Walter *et al.* combined numerical and experimental work to examine shape oscillations and shear induced membrane folding, also concluding that even minor deviations of the initial capsule shape from spherical could result in capsule-shape oscillations.[214] Koleva and Rehage observed polysiloxane microcapsules, identifying three types of motion: tumbling at low shear rates, tank treading with swinging (oscillating shape and orientation about positive values) at high shear rates, and an intermittent region transitioning between tumbling and tank-treading.[215]

The presence of a wall in shear flow can result in a lift force away from the wall, which has been experimentally observed in vesicle flow and predicted computationally for capsules as well.[217–221] Abkarian and Viallat characterized the effect of a wall on vesicle behavior in shear flow.[219] As shear was applied, a deflated vesicle initially in

contact with the wall exhibited a tilted shape with tank-treading; with increasing wall shear, the angle between the vesicle and the wall increased until the shear rate was high enough that the vesicles could detach, after which the shape was steady even far from the wall. This behavior was not observed for quasi-spherical vesicles or polystyrene spheres. The lateral migration of elastic capsules in shear flow has primarily been examined computationally. Singh, Li, and Sarkar studied a capsule in wall-bounded shear with varying Ca and viscosity ratio, and compared its behavior to that of a viscous drop, finding that capsules deform and break symmetry, resulting in migration away from the wall, with slip and migration velocity scaling relationships similar to those of a viscous drop.[221] The wall lift force can also cause lateral migration in Poiseuille flow for deformable objects.[82,222–225] Kaoui *et al.* computationally investigated the migration of a vesicle in Poiseuille flow, finding that vesicles deformed and migrated to the center of flow due to the non-linear nature of Poiseuille flow. As it migrated, the shape of the vesicle changed from elliptical, to tilted, to its final parachute shape, which it obtained at its equilibrium lateral position.[223] Vesicle migration was also examined by Coupier *et al*. in a combination of experimental and numerical studies.[82] They observed lateral migration of particles toward the center of the channel, finding that vesicles quickly moved away from the wall, then slowed as they approached the centerline; the shape of the vesicle also changed from tilted ellipsoid to a symmetric bullet shaped. Capsules are also expected to migrate in Poiseuille flow, as shown by Doddi and Bagchi with 3D numerical simulations on capsules in plane Poiseuille flow.[222] They found that migration velocity depended on Ca, capsule location, and size ratio of the capsule to the channel width. The presence of walls introduces new forces that can result in shape deformation and different flow behaviors.

Capsules,[94,95,122,226,227] vesicles,[198,228,229] and red blood cells[189,190,230,231] in Poiseuille flow at high confinement have been examined in cylindrical capillaries as well as microchannels with square and rectangular cross sections. In approximately axisymmetric channels such as cylindrical or square cross-section, capsules and vesicles that were initially spherical elongated in the axial flow direction into axisymmetric slugs, bullet-like, and parachute-like shapes, with shape transitions driven by Ca and confinement (size ratio of capsule radius to channel radius or half width).[94,123,190,227] Hu *et al.* examined synthetic capsules numerically and experimentally in cylindrical and square pores, observing that with increasing Ca, the capsule transitioned to slug-like, then parachute-like shape. They also noted that with decreasing confinement, higher values of Ca were necessary to see significant deformation.[94,95] Red blood cells, however, have different transitions in microcapillary flow. McWhirter, Noguchi, and Gompper computationally investigated red blood cell (RBC)-like vesicles—vesicles with elastic rather than fluid membranes—in capillary flow.[230,231] For a single isolated RBC, they characterized the shape changes: at low flow rates, the RBC remained biconcave and oriented itself in the direction of the flow, but at sufficiently high flow rates, the red blood cell transitioned directly to a parachute shape.[231] They found that at high hematocrits, there were three distinct phases; RBCs will either retain a biconcave shape, form parachute-like shapes and align, or form slipper-like shapes and order in parallel rows. In rectangular channels, the evolution of shapes differed between vesicles and capsules. Coupier *et al.* both experimentally observed and numerically simulated vesicles in rectangular channels with varying

channel aspect ratios, finding that in channels where the height was not equal to the width, the vesicles would form croissant shapes that were wider along the more-confined axis, rather than bullets or parachutes. They also presented their results in phase diagrams of shapes based on the vesicle reduced volume and Ca or channel aspect ratios.[123] In contrast, Kuriakose and Dimitrakopoulos computationally examined an elastic capsule in a rectangular channel and concluded that the capsule extended more along the less-confined axis as it deformed.[122] Kuriakose and Dimitrakopoulos also found that capsule response to flow rate changes was identical for size ratios of 0.8, 0.9 (moderately sized capsules smaller than the channel width), and 1.1 (capsules slightly larger than the channel width).[122]

The shape changes that have been reported for red blood cells, capsules, and vesicles demonstrate the wide range of deformation possible, and several methods of characterizing and quantifying deformation have been proposed. The Taylor parameter D = (L-B)/(L+B) is often used, where L and B are the longest and shortest particle axes,[185] but it is most useful for small deformation in simple shear flow, where the shape is approximately ellipsoidal. For slugs and parachute-like profiles, essential measurements include the axial and radial lengths, dimple depth, and radius of curvature at the front and back of the object.[95,190,226] Risso *et al.* discussed the general effects of increasing Ca on the evolution of capsule shape, noting that once the curvature of the rear leveled out around Ca=0.08, the deformation seemed to slow down. The curvature at the tip and radial length also reached constant values at sufficiently large Ca.[226]

Quantifying capsule deformation is essential to characterizing capsule properties; for example, deformation in flow has been proposed as a viable method for measuring membrane properties.[94,95,212,232,233] Chang and Olbricht[212] obtained membrane elastic moduli from macroscale capsule deformation in shear flow and compared the values to those obtained from squeezing particles between two parallel plates with a given force,[234] finding good qualitative and order of magnitude agreement. On the microscale, Lefebvre *et al.* used a combination of experimental results from flowing capsules in confined microchannels and numerical modeling to calculate the membrane elastic modulus.[232] They obtained the deformation profile of a capsule in a cylindrical channel and used an inverse analysis, dependent on constitutive law, to calculate the modulus, resulting in agreement within 15-20% to values obtained from large capsules. The same technique could also be adapted to a microchannel with a square cross-section. Hu, Salsac, and Barthès-Biesel further examined this technique, characterizing the 3D effects in channels with circular and square cross-sections and using neo-Hookean law to calculate the membrane modulus.[57] Hu *et al.* later examined the effect of the membrane constitutive law on the results, concluding that it is possible to also determine whether the membrane is strain-hardening or –softening based on the model.[95] Kuriakose and Dimitrakopoulos also evaluated computationally a microfluidic device design that could combine computational and experimental findings to determine the membrane shear modulus independent of the area dilatation modulus.[233] For this technique, a capsule was examined as it flowed through two different-sized capillaries with square cross-sections, the larger one upstream and the smaller downstream, connected by a converging middle section. By comparing the

experimental transient maximum capsule elongation ("elongational overshooting") that occurred when the capsules moved from the constriction into the smaller channel to the computational results they reported, it is possible to determine the Ca and corresponding shear modulus. Although determining the modulus of capsules and other soft objects on the order of 10s to 100s of microns is not straightforward, characterizing their properties is key to designing suspension components with desired properties.

While deformation in confinement has been characterized with red blood cells, vesicles, and capsules, few studies have been done for confined soft elastic particles. Most literature on elastic particles has been computational studies of deformation and motion in shear flow.[186,210] Gao and Hu found that for elastic particles in shear flow, deformation as described by the Taylor parameter varied linearly with Ca when Ca<0.3.[186] Experimentally, Hur *et al.* studied inertial migration of silicone oil emulsion drops and polydimethylsiloxane elastic particles in a microchannel, in which inertial lift drives lateral migration of particles to distinct focusing positions.[77] They concluded that while deformable droplets focused to equilibrium positions closer to the center of the channel, elastic particles with Young's modulus ranging from 0.5-1000 kPa all behaved as rigid particles. The approximate Ca was ~0.01 for a 0.5 kPa modulus elastic particle at Re=21, indicating that softer particles would be necessary for significant deformation. Using poly(N-isopropylacrylamide) (pNIPAM) hydrogel, it is possible to obtain microparticles with shear moduli as low as ~15 Pa,[235] which allows access to higher Ca and a wider range of particle deformation in flow. pNIPAM is particularly appealing because it is responsive to environmental cues such as temperature[30] and solvent;[155] it could potentially be optimized to change modulus and/or size as appropriate depending on the desired application, e.g. drug delivery or sensors.

The objective of this work is to investigate the effect of increasing capillary number, controlled by increasing shear rate, on the deformation of a single soft particle in a rectangular microfluidic channel. First, we discuss the suspension flow experiments and the edge detection procedure used to characterize pNIPAM particle deformation. The shape profiles that developed as Ca was increased from 0.004 to 0.64 are then summarized with non-dimensionalized measurements, identifying the critical parameters for the transitions between each shape. Next, we compare soft particle shapes to literature results for capsules, showing that elastic particle deformation results in distinct shapes unlike those observed in capsules.[95,122] Finally, we consider the use of particle deformation in flow as a method of determining shear modulus.

4.3 Results and Discussion

In this section, we present results for confined particle deformation of two populations of pNIPAM particles, each prepared using a different crosslinker (CL) concentration, resulting in two populations that are each characterized by a distinct shear modulus. The confinement of the two populations was α_S= 0.62 and α_H=0.60 for the softer (0.15% CL) and stiffer (0.6% CL) particles, respectively. To obtain a range of Ca, as defined in Equation 4-1, the shear rate $\dot{\gamma}$ was controlled by changing the flow rate. The characteristic shear rate was defined as the average channel velocity U

(determined from the volumetric flow rate imposed by the syringe pump) divided by the channel hydraulic diameter $D_h=(2wh)/(w+h)$. The deformation is characterized by four dimensionless quantities: non-dimensional radius of curvature R_C/R_{max}, the dimple depth $D_{dimp} = (L_{max}-L_{dimp})/L_{max}$, the elongation $E = L_{max}/2R_{max}$, and circularity C (Equation 2-5). See Figure 2-5 for a schematic with relevant experimental parameters.

4.3.1 Characterization of Observed Shapes

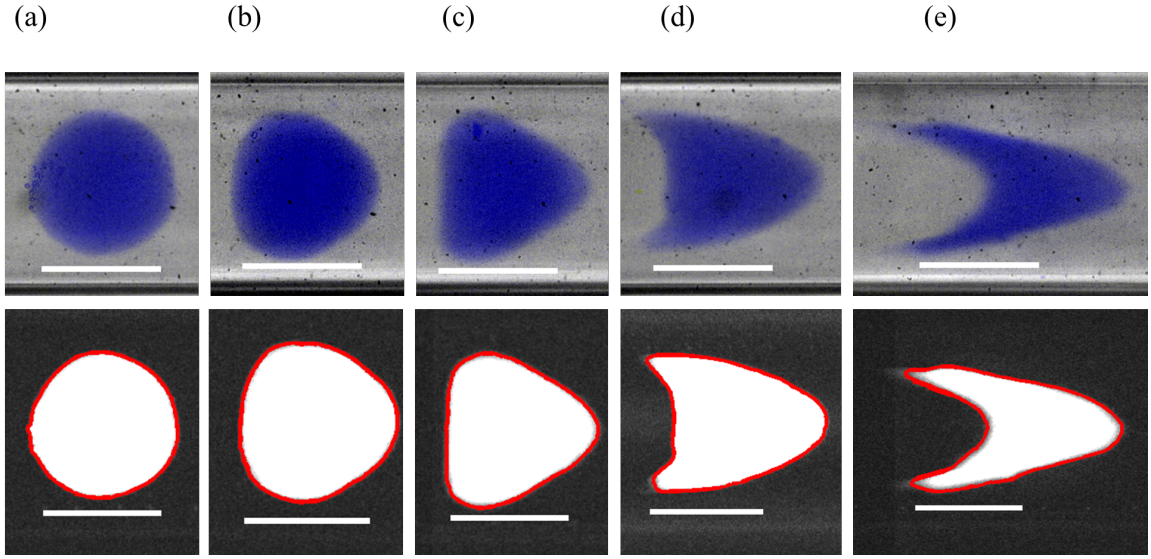

Figure 4-1. Raw images with false coloring (top row) and edge fitting (bottom row) for the range of shapes observed for elastic particles in flow with increasing flow rate and Ca, going from left to right: (a) circular (b) egg (c) triangular (d) arrowhead (e) parachute. The channel has a rectangular cross-section, with a height of 800 μm and a width of 400 μm. The scale bar is 200 μm.

With increasing Ca, particles underwent several shape transitions, resulting in circular, egg, triangular, arrowhead, and parachute shapes, as shown in Figure 4-1. The edge fitting protocol described above provided a quantitative method of distinguishing the whole range of shapes. These shapes, when organized by category rather than flow rate, can be differentiated by the appropriate non-dimensional parameters, namely radius of curvature, dimple depth, elongation, and circularity. Both types of pNIPAM particles, generated using 0.15 wt% and 0.60 wt% crosslinker, developed the same shape types with comparable average parameter values and thresholds. As shear rate and Ca increased, R_C/R_{max} and C decreased, although C decreased very gradually until the dimple formed at the rear ($D_{dimp} > 0$) and the shape became concave. Particle elongation only deviated significantly from 1 once the particle transitioned to an arrowhead or parachute shape. The tip radius of curvature for the triangular, arrowhead, and parachute shapes had similar ranges, and the average values of R_C/R_{max} were comparable for the concave shapes; the change in the deformation that occurred at the rear was more significant than that at the tip.

As the particles began to deform at low Ca, their circularity remained close to 1. However, the radius of curvature at the front tip changed significantly. The first threshold between circular to egg was characterized by the tip curvature and identified as the point where the particle was noticeably narrower at the leading edge compared to the rear, $R_C/R_{max} < 0.8$. The transition between egg and triangular was identified as $R_C/R_{max} < 0.6$. With this threshold, all the circularities for the triangular shapes were also more than one standard deviation lower than the average circularity for the circular particles ($C<0.969$ for 0.15 wt% crosslinker, $C<0.958$ for 0.6 wt% crosslinker), but otherwise still close to 1. At this point, the change in R_C/R_{max} values was minimal, and circularity started decreasing. The arrowhead shape was identified when the dimple started to form at the rear, $0 < D_{dimp} < 0.2$, with a critical circularity of C~0.88. Once $D_{dimp} > 0.2$, the particle was far more elongated and parachute shaped and $C < \sim 0.55$. The arrowhead and parachute shapes have similar tip curvature but distinct C. Table 4-1 and 4-2 summarize these parameters for each shape for both types of particles.

Table 4-1. Average values of the characteristic parameters for each shape observed using 0.15 wt% crosslinker particles, with the standard deviations and population size n.

Shape	R_C/R_{max}	C	D_{dimp}	E	n
Circular	0.93 ± 0.07	0.99 ± 0.004	0	0.987 ± 0.024	25
Egg	0.71 ± 0.06	0.98 ± 0.011	0	0.981 ± 0.018	27
Triangular	0.52 ± 0.07	0.94 ± 0.024	0	0.986 ± 0.022	22
Arrowhead	0.37 ± 0.09	0.71 ± 0.108	0.12 ± 0.063	1.207 ± 0.179	18
Parachute	0.32 ± 0.07	0.42 ± 0.068	0.32 ± 0.050	1.612 ± 0.231	21

Table 4-2. Average values of the characteristic parameters for each shape observed using 0.60 wt% crosslinker particles, with the standard deviations and population size n.

Shape	R_C/R_{max}	C	D_{dimp}	E	n
Circular	0.92 ± 0.09	0.98 ± 0.024	0	1.005 ± 0.018	13
Egg	0.68 ± 0.06	0.97 ± 0.012	0	1.996 ± 0.029	18
Triangular	0.49 ± 0.08	0.92 ± 0.033	0	1.011 ± 0.029	30
Arrowhead	0.35 ± 0.06	0.75 ± 0.086	0.11 ± 0.045	1.143 ± 0.124	30
Parachute	0.31 ± 0.06	0.49 ± 0.096	0.30 ± 0.060	1.730 ± 0.319	24

The shape transitions were reversible, even when the particles underwent significant shear and deformation. This is illustrated in Figure 4-2, where the particles in the left column were deformed significantly at $\dot{\gamma}$ = 651 s^{-1} into triangular and parachute shapes. The same particles are shown in their subsequently relaxed state ($\dot{\gamma}$ = 16 s^{-1}) in the right column, returning back to circular once the shear stress was reduced sufficiently.

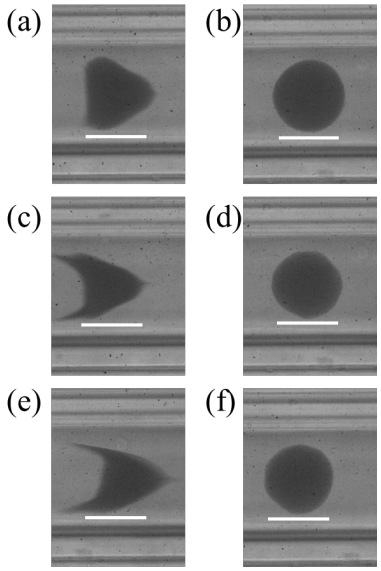

Figure 4-2. 0.5% pNIPAM particles (a, c, e) in high shear rates (Ca=0.4), flow going from left to right and (b, d, f) at low shear rates, (Ca=0.01), flow going from right to left. The scale bar in each image is 200 μm.

4.3.2 Comparison to Previously Reported Results on Capsules

The shapes that the solid elastic particles developed are distinct from the bullet and parachute shapes observed in experiments and simulations for other particle types. When the same analysis is done for the experimental and computational results for capsules previously reported in literature, the difference between the equivalent shapes is evident (Table 4-3). Kuriakose and Dimitrakopoulos[122] computationally increased the Ca of a confined capsule (α=1.1) in a rectangular channel from 0.05 to 0.1 to 0.2. They observed qualitatively similar transitions to those we observe, but the shapes differed quantitatively – in terms of tip curvature and other metrics described above – from those reported here for soft elastic particles. Figure 4-3 shows an example comparison between a parachute-shaped capsule at Ca=0.2 [122] and a corresponding arrowhead-shaped particle at Ca=0.2. Because the confinement of the soft particles is lower than those in literature (Table 4-3), higher Ca may be needed to reach equivalent deformation[94]. However, Kuriakose and Dimitrakopoulos noted that for α = 0.8, 0.9, and 1.1, confinement did not change the effect of flow rate on capsule behavior, so a qualitative comparison of analogous shapes is reasonable.[122] The biggest difference between capsules and particles was the tip curvature and the circularity—both R_C/R_{max} and C for computational and experimental results on capsules were much higher than those for equivalent soft particle shapes. The computational results for capsules also

showed capsules elongated more than the particles, as E > 1 for all capsule shapes, including convex shapes.

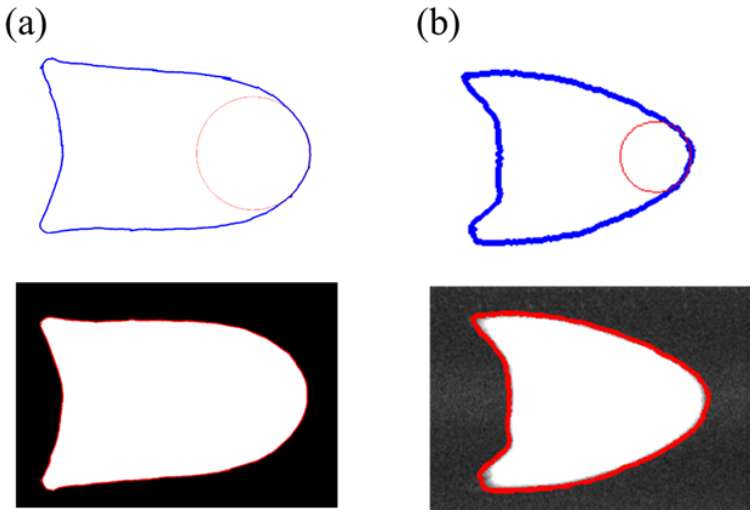

Figure 4-3. Comparison of computational results from Kuriakose and Dimitrakopoulos[122] for capsules with experiments on soft particles with similar deformations at Ca=0.2. Radius of curvature at the tip (top) and edge detection (bottom) for (a) Kuriakose and Dimitrakopoulos capsule in rectangle (C=0.74, D_{dimp} = 0.083, R_C/R_{max}=0.648,E = 1.548) and (b) 0.15 wt% pNIPAM particle (C=0.595, R_C/R_{max}=0.433, D=0.153, E=1.331)

Table 4-3. Parameters for representative pNIPAM particles and for confined capsules[95,122] from literature.

Type	Shape	α	R_C/R_{max}	C	D_{dimp}	E
Soft particle	Experimental, Ca=0.05	0.62	0.525	0.958	0	0.98
	Experimental, Ca=0.1	0.62	0.361	0.905	0	0.99
	Experimental, Ca=0.2	0.62	0.433	0.595	0.153	1.331
Capsule	Computational, Ca=0.05[122]	1.1	0.822	0.906	0	1.288
	Computational, Ca=0.1[122]	1.1	0.723	0.854	0	1.353
	Computational, Ca=0.2[122]	1.1	0.648	0.744	0.083	1.548
	Experimental, v_0=7.3 mm/s[95]	1.05	0.711	0.765	0.139	1.074

4.3.3 Variation in Intrabatch Particle-to-Particle Shear Modulus Affects Shape Variation

There was a notable spread in the shapes observed at a single flow rate for the same type of particle, particularly for the 0.6 wt% crosslinker particles (Fig. 4-4). This could be attributed to the variation in the particle moduli. The shear moduli obtained for the 0.15 wt% and 0.6 wt% CL pNIPAM particles suspended in water were G = 13.1

± 4.7 Pa and 40.5 ± 9.7 Pa, respectively.[235] As the range of moduli within each population was non-negligible, this could affect the particle deformation. The capillary micromechanics characterization was repeated with 10 wt% 8000 MW PEG, the solution used for the channel experiments in this work. In the PEG solution, the 0.15 wt% CL particles had a shear modulus of 13.3 ± 5.5 Pa (mean and standard deviation, n = 10) and the 0.6 wt% CL particles had a shear modulus of 32.5 ± 15.7 Pa (n = 10); both populations had similar variation in moduli compared to those characterized in water. It has been reported that pNIPAM can respond to environmental cues,[30,155] indicated in this case by the difference in shear moduli. Furthermore, the particles shrank noticeably in the 10 wt% PEG solution, from 321 ± 9.8 μm diameter in water to 249 ± 19 μm in PEG. To avoid uncertainty resulting from the hydrogel sensitivity to the suspending fluid, the shear moduli should be measured in the experimental solvent. The moduli responsiveness to the environment also demonstrated the potential of using pNIPAM for environmentally controlled drug delivery, as the modulus directly affects the deformation shape, changing the diffusion from the particle and consequently the rate of drug release.

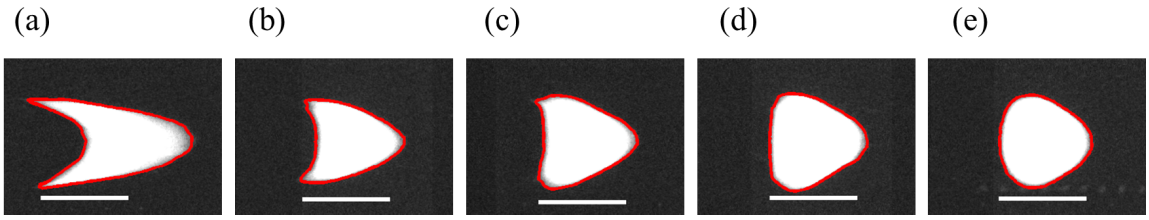

Figure 4-4. Variation of shapes at one flow rate, for 0.6 wt% CL pNIPAM particles at shear rate of 507 1/s, Ca=0.14 based on the mean particle modulus. Scale bar indicates 200 μm.

The standard deviation in the particle modulus for both types of particles corresponds to a range of Ca for each flow rate, with overlapping boundaries. The resulting overlap in shapes between flow rates when organized by circularity reflects the overlap in Ca resulting from variation in shear modulus. This is shown in Figure 4-5, where Ca is plotted as a function of C for each shear rate; the vertical bars indicate the variation in Ca due to the shear modulus and the horizontal bars indicate the minimum to maximum circularity observed.

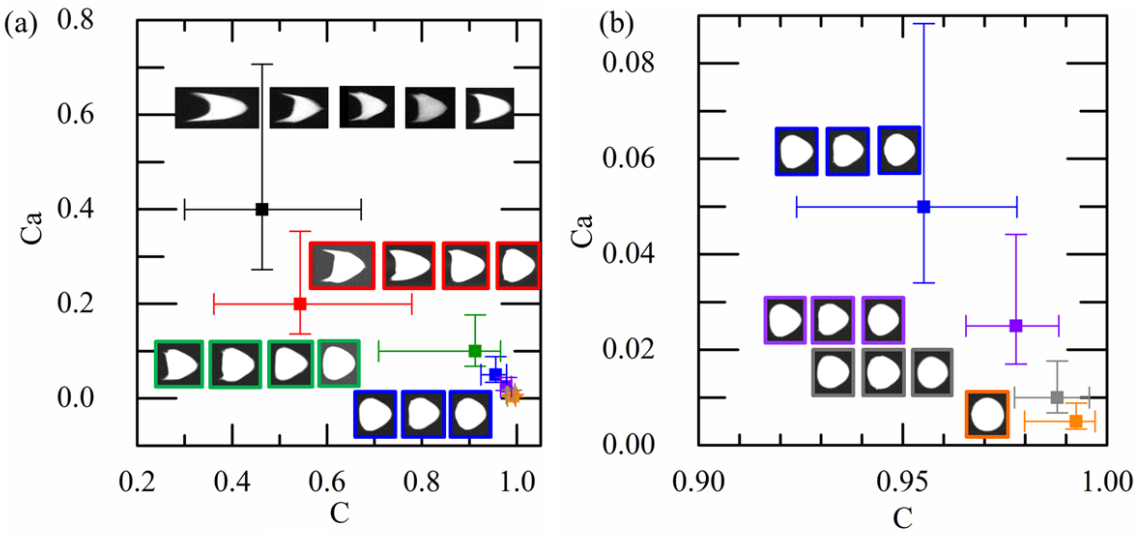

Figure 4-5. (a) Complete Ca vs C plot and (b) Ca vs C plot for Ca < 0.1 for 0.15 wt% pNIPAM particles, where each point indicates a single flow rate. The vertical bars indicate the Ca ranges expected due to the variation in shear modulus. The horizontal bars correspond to the observed ranges for C for that flow rate (minimum to maximum). The set of images for each flow rate are representative of the range of shapes observed within each flow rate.

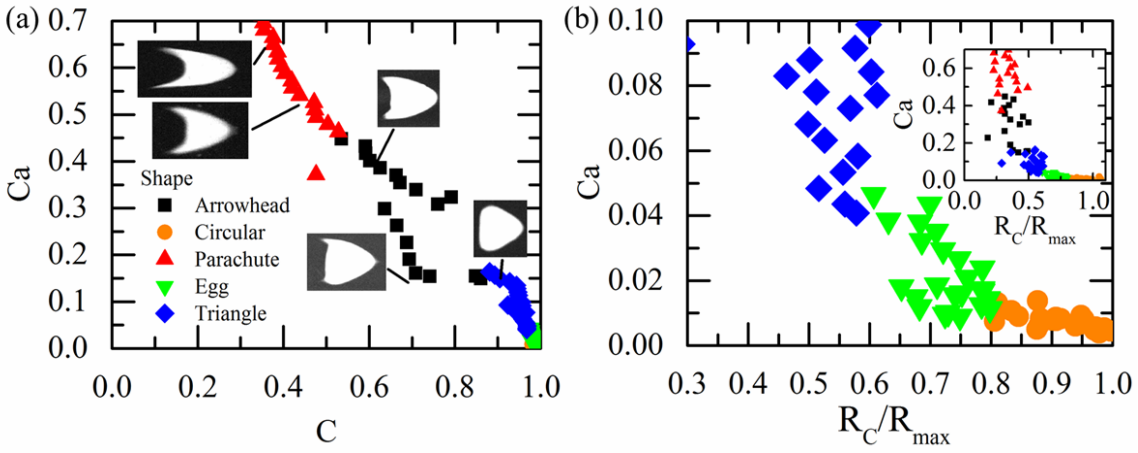

Figure 4-6. Phase diagrams of particle shape on (a) Ca vs. C and (b) Ca vs R_C plots for pNIPAM particles with 0.15 wt% CL. The inset in (b) shows the full distribution, while the main plot focuses on Ca < 0.1. The shapes indicate the same particle deformation on both diagrams.

The comparison of the shapes near the boundaries of the Ca ranges can give an approximate Ca for the transitions between shapes. The most elongated parachute shaped particle has a circularity of C=0.35, corresponding to a Ca~0.74. The transition from parachute to arrowhead occurs between Ca~0.3 and 0.4, where the deformation at Ca~0.3 is distinctly arrowhead shaped and parachute shaped at Ca~0.4, and the

corresponding circularity is around 0.55. Similarly, the transition from arrowhead to triangular occurs at around Ca~0.15, C~0.85, then to egg-shaped at Ca~0.05, C~0.97, then to circular at Ca~0.01, C~0.99. These last two transitions, where circularity and elongation are close to 1, are difficult to distinguish based on C and are better characterized by R_C/R_{max}. Using R_C/R_{max}, the transition between triangular to egg occurs at $R_C/R_{max}>0.6$, Ca < 0.04, and circular shapes are characterized by $R_C/R_{max} > 0.8$, Ca < 0.01.

When the shapes were arranged on the Ca versus C plot with the most deformed particle (lowest C) at each flow rate placed at the upper Ca bound, the least deformed particle placed at the lower Ca bound, and the intermediate shapes linearly spaced based on C in between, the images collapsed onto a phase diagram of shapes based on Ca vs. C (Figure 4-6(a)). Based on this plot, the particle deformation in confinement may be an effective method of determining the shear modulus of individual particles, with the capability of quickly characterizing a large population of particles. Once the shape is categorized, a combination of deformation parameters in addition to the circularity could be used to further identify the Ca and thus the modulus. For example, a particle that became a parachute in flow with C=0.5 would correspond to Ca~0.5. In early transitions when C is close to 1, the circularity varies minimally with changing Ca, so radius of curvature at the front edge gives a better estimate of Ca. Figure 4-6(b) shows Ca plotted as a function of R_C/R_{max}, and the inset demonstrates how the tip curvature levels off at Ca>0.05. For less deformed particles where tip curvature varies significantly, R_C/R_{max} is a better indicator of Ca, but at high deformation when circularity is no longer close to 1, C gives a better estimate of Ca.

4.4 Conclusions

In this work, we have experimentally characterized the deformation and shape transitions of soft elastic microparticles in a confined rectangular channel, which is relevant to developing drug delivery particles. We first generated and characterized two populations of pNIPAM hydrogel microparticles that were soft enough to deform in microchannel flow, with shear moduli of 13.3 ± 5.5 Pa and 32.5 ± 15.7 Pa. The two populations underwent similar deformation for equivalent Ca with confinement ratio $\alpha = 0.62$, resulting in five observed shapes: circular, egg, triangular, arrowhead, and parachute. Using our edge fitting protocol, characteristic non-dimensional parameters (radius of curvature at the tip, dimple depth, circularity, and elongation) were obtained for each shape. The thresholds for transitions between shapes were also quantified, where the shape changed from circular to egg when $R_C/R_{max}<0.8$, then to triangular when $R_C/R_{max} < 0.6$ as shear rate increased. For these shapes, circularity varied minimally. Afterward, the shape became concave at the rear ($D_{dimp}>0$, $C<0.88$), forming the arrowhead shape until $D_{dimp} > 0.2$, $C<0.55$, and the shape became parachute-like. These shapes were unique from those observed with similar experimental and computational results done on capsules, with a smaller radius of curvature at the tip and lower circularity for analogous shapes. The deformation was reversible, with even the highly deformed particles relaxing back to a circle after the shear was eliminated. As solid elastic particles were robust even in significant shear,

elastic particles would have a different mode of drug delivery compared to capsules, which are expected to rupture for delivery. The different shapes would affect the rate at which the drug diffused out, allowing for sustained or environmentally triggered release.

Because the shear moduli for each particle population had variation, each flow rate had a range of Ca and resulting shapes, where the boundaries overlapped with the adjoining flow rates. When all the shapes from every flow rate were combined and quantified, it was found that there were two limiting cases: lower deformation, where both circularity and elongation were close to 1, and higher deformation, where C and E start decreasing rapidly. In the first scenario, with circular and egg shapes, the radius of curvature at the tip decreased significantly with Ca, so R_C/R_{max} was the primary criterion. Once the particle becomes triangular, arrowhead, or parachute shaped, the deformation was better characterized by C. In this case, the Ca versus C phase diagram combined to generate a direct Ca to C comparison. A combination of these two parameters was used to determine the Ca thresholds for each shape transition. The shape transition from circular to egg to triangular to arrowhead to parachute occurred at Ca~0.01, Ca~0.04, Ca~0.15, and Ca~ 0.45, respectively. The Ca can be further differentiated within the shapes as a function of circularity when $C < 0.9$ based on the phase diagram. For circularity close to 1, the phase diagram comparing Ca to R_C/R_{max} can be used to determine Ca instead. Due to the sensitivity of the shape to variations in particle modulus, deformation in flow may be a good measure of particle deformability. By determining the Ca from the particle shape, circularity, and particle tip curvature, the shear modulus can be obtained for a suspension of soft particles.

4.5 Acknowledgements

This material is based on work supported by the National Science Foundation under Grant No. CBET 1066334. Any opinions, findings, and conclusions or recommendations expressed in this material are those of the authors and do not necessarily reflect the views of the National Science Foundation.

5 Flow of Viscoelastic Fluids around a Sharp Microfluidic Bend: Role of Wormlike Micellar Structure

5.1 Abstract

We examine the flow and instabilities of three viscoelastic fluids — a semi-dilute aqueous solution of polyethylene oxide (PEO) and two wormlike micellar solutions of cetylpyridinium chloride (CPCl) and sodium salicylate (NaSal) — around a microfluidic 90^0 bend, in which shear deformation and streamline curvature dominate. Similar to results reported by Gulati *et al.* [Phys. Rev. E **78**, 036314 (2008) and J. Rheol. **54,** 375 (2010)] for PEO solutions, we report a critical Weissenberg number (Wi) for the onset of lip vortex formation upstream of the corner. However, the decreased aspect ratio (channel depth to width) results in a slightly higher critical Wi and a vortex that grows more slowly. We consider wormlike micellar solutions of two salt to surfactant concentration ratios, R = 0.52 and R = 0.75. At R = 0.52, the wormlike micelles are linear and exhibit strong viscoelastic behavior, but at R = 0.75, the wormlike micelles become branched and exhibit shear banding behavior. Microfluidic experiments on the R = 0.52 solution reveal two flow transitions. The first transition, at Wi = 6, is characterized by the formation of a stationary lip vortex upstream of the bend; at the second transition, at Wi = 20, the vortex fluctuates in time and changes size. The R = 0.75 solution also exhibits two transitions. The first transition at Wi = 4 is characterized by the appearance of two intermittent vortices, one at the lip and one at the far outside corner. Increasing the flow rate to Wi > 160 results in a transition to a second unstable regime, where there is only a lip vortex that fluctuates in size. The difference in flow transitions in PEO and wormlike micellar solutions presumably arises from the additional contribution of wormlike micellar breakage and reformation under shear. The flow transitions in wormlike micellar solutions are also significantly affected by chain branching.

5.2 Introduction

Newtonian flows in microfluidic devices are typically laminar due to the small characteristic dimensions that render Reynolds numbers (Re) small. However, adding a small amount of polymeric material has been shown to introduce new secondary flows in microfluidic geometries at low Re.[15,23,236–239] The underlying physics behind the secondary flows at vanishing Re is attributed to a coupling of the curvature of the flow streamlines and the elastic nature of long, flexible polymer chains that stretch in flow[240]. These secondary flows have been reported in a variety of microfluidic geometries, including planar expansions and contractions, cross-slot geometries, wavy channels, and sharp 90^0 micro-bends.[16,19,22,23,238,239] A general criterion for the onset of purely elastic instabilities in two-dimensional geometries was suggested by McKinley *et al.*[241,242], who predicted that the onset occurs beyond a dimensionless parameter M_{crit} with the following form:

$$M_{crit} \le \left[\frac{\lambda U}{R_C} \frac{\tau_{11}}{\eta_0 \dot{\gamma}} \right]^{1/2}, \qquad \text{(Equation 5-1)}$$

where λ, U, R_c, τ_{11}, η_0, and $\dot{\gamma}$ are the relaxation time of the polymer, characteristic velocity, radius of curvature, normal stress in the direction of the flow, zero shear viscosity, and shear rate, respectively. This criterion was developed based on Upper Convected Maxwell and Oldroyd-B models, and, in a range of two-dimensional geometries with streamline curvature, McKinley and co-workers showed that flow of viscoelastic fluids that are well-described by these models become unstable to infinitesimal perturbations for $M_{crit} \sim 4.6 - 8.4$.[241,242] They also showed that the criterion could be re-written to account for shear-thinning as:

$$M_{s,crit} \le \left[\frac{U\dot{\gamma}}{R_C} \frac{\Psi_1(\dot{\gamma})^2}{4\eta_p{}^2} 2(1-\beta) \right]^{1/2}, \qquad \text{(Equation 5-2)}$$

where $\Psi_1(\dot{\gamma})$, η_p, and β are the shear-rate dependent first normal stress coefficient, polymer contribution to the viscosity, and the solvent viscosity ratio η_s/η_0, respectively.

Elastic instabilities have been extensively studied in microfluidic flows composed of a combination of shear deformation and planar extension[15,18,23,236–239,243,244]. Sudden contraction and expansion microfluidic devices are one example of such flows. Rodd and co-workers studied the flow of aqueous polyethylene oxide (PEO) solutions in planar, symmetric contraction and expansion micro-geometries and reported three instability regimes[15,236]. For moderately shear-thinning viscoelastic solutions, the base flow becomes unstable beyond a critical Weissenberg number Wi ~ 50, where Weissenberg number is defined as $Wi = \lambda\dot{\gamma}$. For the range of $50 < Wi < 100$, stationary vortices formed, and for higher Weissenberg numbers, asymmetric vortices were evident. Rodd *et al.* reported similar transitions for non-shear thinning viscoelastic

fluids based on polyethylene oxide/water/glycerol[236]. In addition, Gulati and co-workers studied the flow of shear thinning semi-dilute λ-DNA solutions in sudden contraction microfluidic devices for a wide range of elasticity (El) numbers ($6.4\times10^3 <$ El = Wi/Re $< 1.4\times10^6$)[238]. The Reynolds number (Re) is defined here as $\mathrm{Re} = \rho U D_h / \eta(\dot{\gamma})$, where ρ is solution density, U the average velocity in the downstream channel, D_h the hydraulic diameter of the channel (2wh/(w+h)), and $\eta(\dot{\gamma})$ the shear dependent viscosity. Gulati *et al.* observed that vortices that are symmetric about the centerline form upstream of the contraction and increase in size as Weissenberg number increases[238]. Other researchers have also studied the effect of fluid rheology, aspect ratio, and polymer concentration on instabilities and transitions in micro-contraction geometries[239,244].

Another microfluidic geometry that has received considerable attention is the cross-slot geometry. A cross-slot consists of perpendicular channels with opposing inlets and opposing outlets at 90 degrees to the inlets. Near the walls, the flow is predominantly shear deformation, whereas closer to the stagnation point, the extensional flow becomes dominant. Arratia *et al.*[23] observed a series of purely elastic transitions in the flow of polyacrylamide/glycerol/water solutions in a cross-slot geometry at vanishing Reynolds numbers. Defining a Deborah number in terms of the extension rate $\dot{\varepsilon}$ as $\mathrm{De} = \lambda\dot{\varepsilon}$, these authors found that the symmetric base flow undergoes instability to a steady, asymmetric flow at De = 1.8, followed by an unsteady regime characterized by non-periodic fluctuations at De > 12.5. At the highest flow rates (De ~ 26.4), the formation of vortices near the corners that fluctuate in space and time was reported. Subsequent studies investigated the effects of inertia, aspect ratio, and polymer concentration on the flow stability in viscoelastic polymer solutions in a cross-slot[16,18,245]. Most recently, Haward *et al.*[246] performed detailed velocimetry and birefringence experiments on an optimized-shape cross slot extensional rheometer that eliminates the sharp corners of the traditional cross slot and moves the steamlines of highest curvature close to the stagnation point. These authors found new instabilities at lower De than those in traditional cross slots and determined a value of the criterion M_{crit} (for non-shear-thinning viscoelastic fluids) for the first instability that was close to values reported in shearing flows.

Although there are numerous studies that demonstrate viscoelastic instabilities in simple shear or shear-dominated flows with curved streamlines in macro-scale flows[240,247–252], there are few available experimental studies in microfluidic geometries. Gulati *et al.*[21,22] studied the flow of viscoelastic, shear-thinning solutions of DNA and of polyethylene oxide/polyethylene glycol/water (PEO/PEG/water) in a sharp 90^0 microfluidic bend geometry for the first time. In earlier macroscale studies, Chono and Iemoto reported a slight shift of the fluid streamlines for conditions near Re ~ 1 and Wi ~ 1 that was consistent with their 2D numerical simulations[251,252]. In their microfluidic studies, Gulati *et al.* were able to access the purely elastic limit (i.e., El >>1), and they showed that beyond a critical threshold ($M_{s,crit} \sim 0.73$, where $M_{s,crit}$ is defined in Equation 5-2) above), the base flow becomes unstable. The instability is characterized by the formation of a steady lip vortex upstream of the corner that increases in size as Weissenberg increases. However, in a similar range of Wi and Re, flow of a non-shear

thinning viscoelastic polyethylene oxide/polyethylene glycol/water solution never displayed any secondary flow. Therefore, they concluded that shear-thinning behavior is a necessary feature for the presence of such secondary vortices.

Instabilities have also been reported in a shear-dominated microfluidic geometry that consists of wavy microfluidic channels[19,253]. Pathak *et al.* studied flow of a non-shear-thinning, viscoelastic solution (a Boger fluid) based on a high molecular weight polyacrylamide (PAA) in a solvent of water/sucrose in a microfluidic geometry with a zig-zag pattern and showed that secondary flows enhance fluid mixing[253]. Zilz *et al.*[19] also used a combination of experimental, numerical, and theoretical analyses to study purely elastic instabilities in microfluidic serpentine channels. Zilz *et al.* adapted Pakdel and McKinley's scaling analysis to serpentine channels and found good agreement with their experimental findings for the onset of purely elastic instabilities.

In microfluidic experiments, the depth of the device is fixed during the microfabrication process, and the aspect ratio (AR), that is the ratio of the depth to a characteristic width, can be an important factor. Numerical studies have considered the effects of aspect ratio for a range of geometries, including contraction-expansion flows[254,255], T-junctions[256], and serpentine channels.[19,20] One of the best documented cases is that of the cross-slot[16,245]. Cruz and co-workers[245] simulated the creeping flow of an Upper Convected Maxwell fluid and a simplified Phan-Thien Tanner fluid in 3-dimensional planar cross slots that varied in aspect ratio from near the Hele-Shaw flow (low aspect ratio) limit to the two-dimensional (high aspect ratio) flow limit. For deep channels, where AR > 1, two flow transitions were observed with increasing Weissenberg number: the steady, symmetric flow at low Wi is replaced first by a steady asymmetric flow at intermediate Wi, then by an unsteady flow at high Wi. For shallow channels, where AR < 1, a single transition from steady, symmetric flow to unsteady flow was predicted, and the critical Wi varies linearly with AR. Since square channels (AR = 1) sit at the intersection of these two regimes, the authors conclude that the sequence of transitions for AR = 1 is unclear. In addition, they note that the depth at which a channel may be considered to provide a good approximation of 2D flow is strongly dependent on the rheological properties of the fluid. The experiments of Sousa *et al.*[16] are consistent with these predictions in terms of the appearance of the intermediate steady, asymmetric flow only at AR > 1. In general, when the aspect ratio decreases, the walls stabilize the flow, preventing the occurrence of the asymmetric flow and delaying the transition to unsteady flow to higher Wi. Sousa *et al.* also note the presence of a small, upstream lip vortex at AR = 0.5 and low Wi when the flow is steady and symmetric. As Wi is increased at AR = 0.5, the lip vortex grows, and a time dependent flow is observed.

Although the studies referenced above have focused on solutions of linear, flexible polymers, surfactant-based viscoelastic solutions have received a lot of attention in the past decade due to their wealth of interesting fluid dynamics and rheological behavior[98,101,257,258]. These fluids are made by dissolving surfactants and salts in water. Beyond a critical micelle concentration, the addition of salt transforms spherical micelles into wormlike micelles that, at sufficiently high concentration, entangle and in turn induce a viscoelastic response[98,101]. Similar to polymeric solutions,

wormlike micellar fluids have shown signs of instabilities in rotational shear flows with curved streamlines as well as extensional flows in macro-scale studies[110,111,118,259,260]. Studies of wormlike micelles in micro-scale flows have focused mainly on cross-slot and contraction-expansion geometries that involve a combination of planar extensional and shear deformations at different points throughout the flow[112–115,120,121,261,262].

Pathak and Hudson first used a microfluidic cross-slot geometry to study instabilities in wormlike micellar solutions based on cetyltrimethylammonium bromide and sodium salicylate (CTAB/NaSal) and on cetylpyridinium chloride and sodium salicylate (CPCl/NaSal) systems[115]. These authors reported the presence of bright birefringent bands in the vicinity of the stagnation point and noted an asymmetric flow due to the high elasticity of the wormlike micelles. Haward *et al.*[261] also studied the flow of CPCl/NaSal solutions in a deeper microfluidic cross-slot geometry over a wider range of Weissenberg numbers and reported three regimes of flow behavior: steady, symmetric flow at $Wi < 1$, steady asymmetric flow as Wi is increased beyond $Wi = 1$, and the onset of time-dependent, rapidly fluctuating aperiodic flow at $Wi > 350$. Thus, the sequence of transitions for this wormlike micellar fluid appear similar to those observed for linear, flexible polymers in a deep microfluidic cross-slot. In addition, these authors present the first evidence of a lip vortex forming in a wormlike micellar fluid. Dubash *et al.* presented a similar study of a series of wormlike micellar solutions based on the CTAB/NaSal system[114] in flow in a cross slot and presented their results in terms of a phase diagram based on controlling parameters (Wi-Re). Dubash *et al.*[114] also reported formation of lip vortices near the walls of the cross-slot geometry. They found similar flow transitions to Haward and co-workers but observed that the development of the lip vortex occurred before the onset of asymmetric flow for one fluid and after asymmetric flow onset for a different solution.

Wormlike micellar fluids have also been studied in contraction-expansion geometries both experimentally and numerically. Stukan and co-workers[112,120] used computational modeling to study the effects of micelle size, channel dimensions, and the non-Newtonian nature of the fluid on the dynamics of wormlike micelles through micro-expansion/contractions. In experiments, Ober *et al.*[121] used a combination of pressure measurements and micro-particle image velocimetry to estimate the extensional viscosity of wormlike micelles in a hyperbolic contraction geometry. Additionally, Li *et al.*[263] studied flow transitions and instabilities of viscoelastic surfactant solutions based on cetyltrimethyl ammonium chloride/sodium salicylate (CTAC/NaSal) in three different microfluidic geometries: flow past a cylinder, sudden contraction and expansion, and serpentine microchannels. Li *et al.*[263] reported formation of secondary flows due to coupling between the curvature of the streamlines and elasticity of the viscoelastic surfactant solutions. For a more comprehensive survey on these studies, readers may consult the recent review by Zhao *et al.*[264]

The main objective of this work is to study the flow and instabilities of wormlike micellar solutions in microfluidic flows under the influence of shear deformation and streamline curvature. Although other geometries, such as the cross-slot and contraction-expansions, provide a mixture of shear deformation and extensional flow, the abrupt 90^0 micro-bend geometry provides a shear-dominated

deformational flow. We are particularly interested in characterizing the transitions and instabilities in wormlike micellar solutions with different structures. It has long been known that the structure of wormlike micelles has a pronounced effect on the flow behavior and rheology of these systems.[265] The structure of the wormlike micelles can be manipulated by varying the ratio of the salt to surfactant concentration.[106–108] The addition of salt to surfactant solutions converts the behavior of the solution from a Newtonian to a viscoelastic solution that, under appropriate conditions of concentration and temperature, displays single mode Maxwell model behavior in small amplitude oscillatory shear flow. This transformation is mainly due to the change in the topology of micelles from spherical to wormlike. However, beyond a critical threshold, a further increase of salt concentration results in the formation of branched networks. The change in the structure of different wormlike micellar systems has been directly evidenced by Cryo-TEM images[106–108,266]. In this paper, we study the effect of wormlike micellar structure on the transitions and instabilities in the micro-bend geometry by varying the ratio of the salt to surfactant as well as the strength of the flow. For this purpose, we use a very well-studied wormlike micellar system based on CPCl/NaSal with different salt/surfactant ratios. We also note that the geometrical parameters of this microfluidic device are slightly different from the similar geometry used in prior work by Gulati and co-workers[21,22]. Therefore, we also conduct experiments with a semi-dilute viscoelastic PEO solution. This allows us to consider the effect of aspect ratio on the onset of secondary flows for PEO solutions; additionally, the results for the PEO solution serve as a benchmark to compare with the results of wormlike micellar solutions.

5.3 Materials and Methods

The flow of viscoelastic solutions is studied in a sharp, 90^{o} micro-bend, schematic diagrams of which are shown in Figure 5-1. The device has two 6-mm long rectangular channels, both 110 μm wide and 70 μm deep, meeting in a sharp 90° corner. Each channel is connected to a reservoir with two through-holes. The micro-bends are fabricated in silicon using deep reactive ion etching and sealed by anodically bonding a 170 μm thick Pyrex glass wafer to the silicon device. Details of the fabrication process have been reported elsewhere[21]. Flexible Tygon tubing with 1/16 inch inner diameter is attached to the through-holes of the reservoirs with a fast curing two part epoxy (Devcon 5 Minute Epoxy, ITW Devcon, Danvers, MA). 2.5-mL gastight glass syringes (Hamilton) are threaded with a 22G plastic dispensing tip (McMaster-Carr) and attached to the tubing. To ensure that the device is cleared of any previous solution, filtered (Acrodisc, 0.2-μm PVDF membrane) soapy water, then filtered de-ionized water is run through the device. Once the device is flushed, the polymer or wormlike micellar solution is introduced and the vent opened until debris and air bubbles are flushed. Once the vent is closed, each flow rate is maintained for at least 30 minutes before videos are taken. Flow is controlled with a Harvard Apparatus PHD 2000 syringe pump.

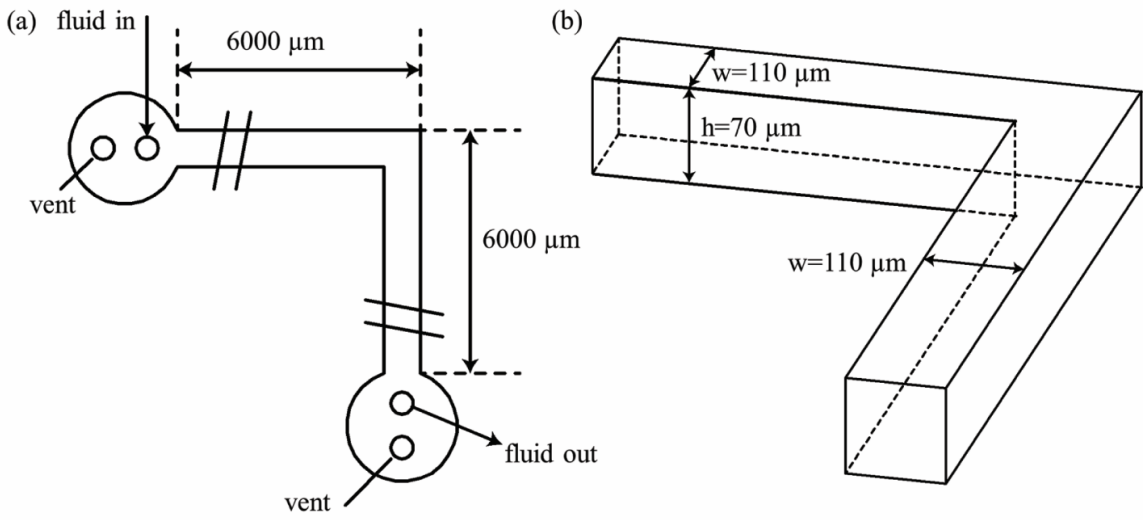

Figure 5-1. Schematics of (a) the top view of the 90° abrupt micro-bend device and (b) the micro-bend geometry where h is the depth and w is the channel width of the device. In all experiments, h = 70 μm and w =110 μm.

Flow visualization experiments in the micro-bend are conducted using fluorescence microscopy. A Leica DMIRE2 inverted microscope with a 20x objective is used with an external light source (Leica EL6000). The optimal filter for our system is a dual band excitation/emission filter (Chroma 51004v2, 460-500/510-560 nm). Videos are taken with a high speed camera (Vision Research, Phantom Miro M310) at capture rates between 24 and 1000 fps. Analysis of videos is done with ImageJ (NIH) and MATLAB (MathWorks). Streak images are obtained in MATLAB in two steps. A background image is generated by taking the arithmetic mean of the pixel intensities for a stack of 20 to 2000 frames, which is then subtracted from the original stack. The resulting frames are then overlaid to form the final streak images, using the highest intensity value for each pixel from the entire stack of frames.

Semi-dilute PEO and wormlike micellar solutions based on cetylpyridinium chloride (CPCl) and sodium salicylate (NaSal) are explored in this microfluidic geometry. Polyethylene oxide with a molecular weight of 2×10^6 g/mol is obtained from Sigma Aldrich; CPCl and NaSal are obtained from Spectrum Chemical. The semi-dilute PEO solution is formulated by mixing 3390 ppm of PEO in a viscous solvent that contains 60 % by weight de-ionized water and 40 % by weight polyethylene glycol (PEG) with a molecular weight of 8×10^3 g/mol (Alfa Aesar).

We have also formulated two surfactant solutions with a constant surfactant concentration ([CPCl] = 100mM) and two salt to surfactant ratios (R= [NaSal]/[CPCl] = 0.52 and 0.75). These solutions are selected such that they result to two different structures for wormlike micelles; i.e., linear and branched chains. Gaudino *et al.*[107] showed that similar wormlike micellar solutions based on CPCl/NaSal have a linear structure if the ratio of salt to surfactant R (=[NaSal]/[CPCl]) < 0.6 and have a branched

structure for ratios higher than this value. The two solutions in the present study, corresponding to R = 0.52 and R = 0.75, also lie on opposite sides of a maximum in zero-shear viscosity as a function of R. Oelschlaeger *et al.*[106] have examined the system we study here in detail and concluded that this viscosity maximum corresponds to a transition from linear to branched micelles. Therefore, we expect a linear wormlike micellar structure for our solution with R = 0.52 and a branched structure for R = 0.75. To visualize the flow of the solutions in the bend, we seeded each solution with 0.005-0.02 v/v% 1-μm fluorescent polystyrene spheres (Fluoro-Max™ green fluorescent polymer microspheres).

5.4 Fluid Characterization

All viscoelastic solutions are characterized in a stress-controlled Malvern Gemini rheometer that is equipped with a cone and plate as well as Couette co-axial cylinder geometries. Small amplitude oscillatory shear (SAOS) and steady shear rheology experiments are carried out to measure the longest relaxation time of viscoelastic solutions and the shear viscosity, respectively. Figure 5-2(a) shows the results of SAOS measurements for the PEO solution. The best fit to the experimental results is given by a three-mode Maxwell model, shown by the solid curves in Figure 5-2(a). The m-mode generalized Maxwell model can be expressed as follows:

$$G'(\omega) = \sum_{i=1}^{m} \frac{G_i \lambda_i^2 \omega^2}{1+\lambda_i^2 \omega^2}, \qquad G''(\omega) = \sum_{i=1}^{m} \frac{G_i \lambda_i \omega}{1+\lambda_i^2 \omega^2}, \tag{3}$$

where G', G", G_i , ω and m are the storage modulus, loss modulus, relaxation modulus for mode i, angular frequency, and number of modes, respectively.

Figure 5-2(b) shows the shear dependent viscosity of the moderately shear thinning PEO solution. Experimental results are fit to a power-law fluid model that can be represented as $\eta(\dot{\gamma}) = \kappa \dot{\gamma}^{n-1}$, where κ is the consistency factor and n is the power-law index. Figure 5-2(b) also shows the first normal stress coefficient Ψ_1 as a function of shear rate. As Ψ_1 remains fairly constant, a non-shear thinning averaged value of Ψ_1 = 0.030 Pa·s^2 is used. These results are similar, although not identical, to the results on a comparable PEO solution (PEO2 in Gulati *et al.* [21]) used in an earlier study of flow in a micro-bend from our laboratory. In particular, the PEO solution used in the present study is *slightly* less shear-thinning and has a slightly longer relaxation time λ_1.

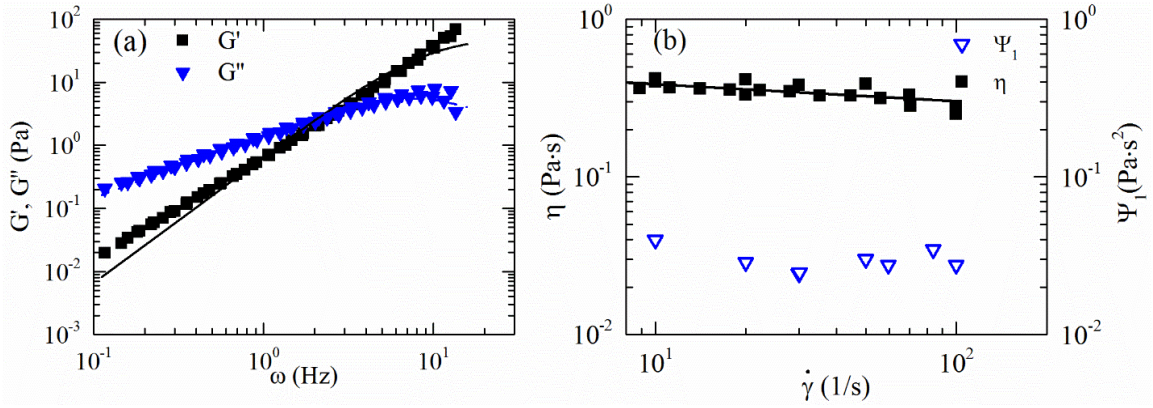

Figure 5-2. (a) G' and G" versus angular frequency for the PEO solution. The lines are the fit to a three mode Maxwell model; parameters are given in Table 5-1. (b) Shear rate dependent viscosity on the left axis and first normal stress coefficient rate on the right axis versus shear. Power-law parameters are listed in Table 5-1.

We also characterized the wormlike micellar solutions with different salt to surfactant ratios. Figure 5-3(a) shows the results of small amplitude oscillatory shear on the two samples used for the flow experiments. For the sample with R = 0.52, the best fit is given by a two-mode Maxwell model. However, for R = 0.75, the best fit is given by a single-mode Maxwell model. Figure 5-3(b) shows the shear stress versus shear rate for the two wormlike micellar solutions. The inset of Figure 5-3(b) also shows the shear-rate-dependent viscosity of these solutions. It is evident that the wormlike micellar solution with R=0.75 exhibits a stress plateau within a shear rate range of $3.5 < \dot{\gamma} < 26$ (1/s), indicated in Figure 5-3(b) by the arrows, while the solution with R=0.52 does not show a similar stress plateau. Therefore, only the wormlike micelles with R=0.75 is a shear-banding solution. The list of relaxation times and plateau moduli for all solutions is given in Table 5-1. Of particular interest is that the longest relaxation times, λ_1, are comparable for all three solutions and nearly identical for the two wormlike micellar solutions. As a result, we are able to access comparable Weissenberg numbers for all solutions in our micro-bend device. Figure 5-4 shows the first normal stress coefficient as a function of shear rate for the wormlike micellar solutions, along with the power-law fit.

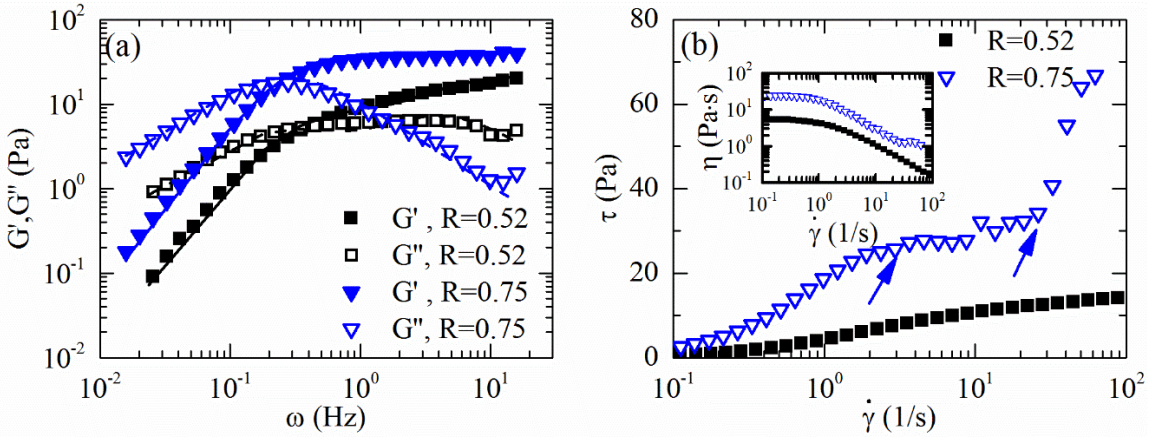

Figure 5-3. (a) G' and G'' as a function of angular frequency for wormlike micellar solutions of CPCl /NaSal; lines are best fits to the Maxwell model. (b) Shear stress versus shear rate for the two CPCl/NaSal systems. Blue arrows indicate the stress plateau for R=0.75. Inset shows the viscosity as a function of shear rate.

5.5 Results and Discussion

In this section we present the results for different viscoelastic solutions in the micro-bend geometry. As noted before, in addition to wormlike micellar solutions, we have tested a semi-dilute PEO solution similar to one used in Gulati *et al.*[21] In the following, we present our results for the PEO solution first and compare them with prior results on this system with a similar geometry that has slightly different dimensions. Then, we describe the results of the wormlike micellar systems. Finally, we compare flow transitions and instabilities in wormlike micellar solutions to the semi-dilute polymer solutions based on PEO.

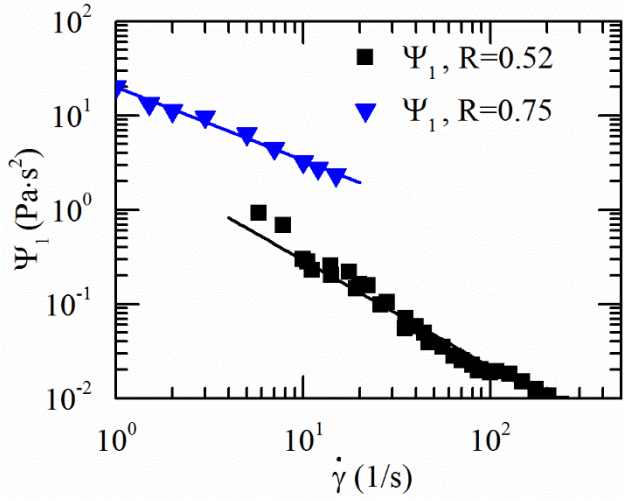

Figure 5-4. First normal stress coefficient versus shear rate and power law fit for the two CPCl/NaSal systems. For R = 0.52, $\Psi_1(\dot{\gamma})=3.942\dot{\gamma}^{-1.131}$, and for R = 0.75, $\Psi_1(\dot{\gamma})=20.083\dot{\gamma}^{-0.778}$.

Table 5-1. List of power law parameters, relaxation times, relaxation moduli, and the viscosity ratio for the viscoelastic solutions studied in this work; also included are data for a similar PEO solution (PEO2) used in Gulati *et al.*[21]

Fluid	PEO	PEO2[21]	CPCl/NaSal (R = 0.52)	CPCl/NaSal (R = 0.75)
Power law index, n	0.889	0.878	0.188	0.124
Consistency factor, κ (Pa·s^n)	0.496	0.498	6.555	22.35
λ_1	0.328	0.287	0.62	0.61
λ_2	0.0036	0.0266	0.049	
λ_3	0.002	0.00063		
G_1	0.26	0.403	7.81	41.12
G_2	763	4.901	12.85	
G_3	0.002	416		
β	0.26		1.9×10^{-4}	7.0×10^{-5}

In the following, we define the Weissenberg number as $\mathrm{Wi} = \lambda_1\dot{\gamma}$, where λ_1 is the longest relaxation time of the solution and $\dot{\gamma}$ is the characteristic shear rate. We define the characteristic shear rate as the average channel velocity U divided by the channel half-width, w/2. Based on our earlier results, in which shear thinning was shown to play a critical role, we use the version of the stability criterion given in Equation 5-2 that is generalized for a shear-thinning viscoelastic fluid [cf. Equation (23) of McKinley *et al.*[241]] that we refer to as $M_{s,crit}$. Here, we define R_c as the radius of curvature for a streamline at the midline of the bend, which is measured to be about 105 μm, and τ_{11} is the normal stress in the streamwise direction calculated from the fit of the normal stress measurements in steady shear. As noted in the introduction, the

Reynolds number is defined as $Re = \rho U D_h / \eta(\dot{\gamma})$, and the elasticity number is El = Wi/Re.

5.5.1 Semi-dilute PEO Solution

Figure 5-5 shows streak images of the flow of the PEO solution in the sharp micro-bend as a function of Wi. We observe a critical threshold for the onset of vortex formation upstream of the corner at Wi ~ 4.7. Beyond this critical condition, the vortex increases in size as Wi increases.

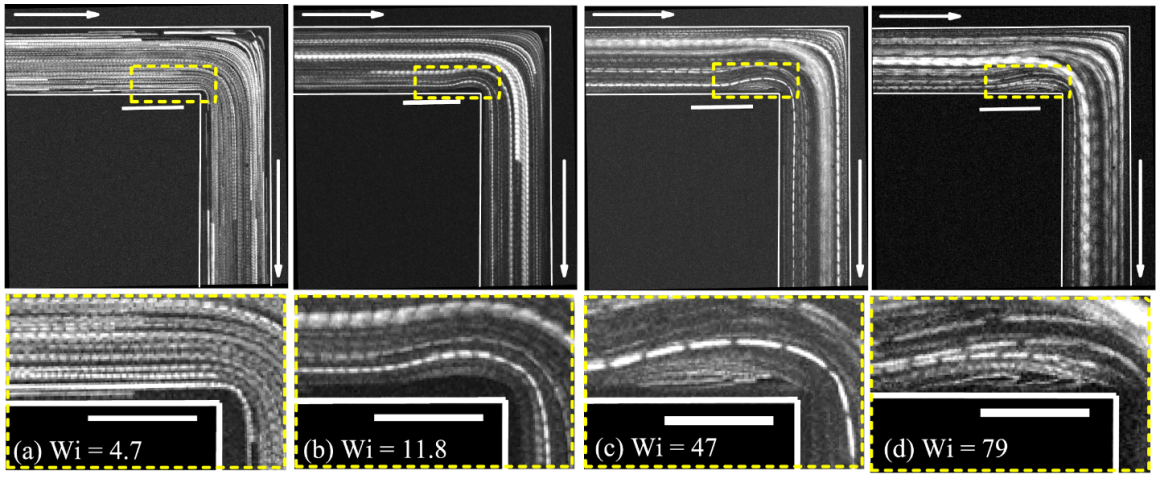

Figure 5-5. Streak images of flow in the 90 degree micro-bend for PEO at (a) Re = 2.8×10^{-4}, Wi = 4.7, El = 1.7×10^{4}, (b) Re = 7.8×10^{-4}, Wi = 11.8, El = 1.5×10^{4}, (c) Re = 3.6×10^{-3}, Wi = 47, El = 1.3×10^{4}, and (d) Re = 6.4×10^{-3}, Wi = 79, El = 1.2×10^{4}. Figure scale bars are 100 μm. Inset scale bars are 50 μm. Flow enters the channel in each image from the top left and exits at the bottom right, as indicated by the arrows.

Figure 5-6(a) shows the dimensionless vortex length χ as a function of Wi for the PEO solution used in the present work. χ is calculated by non-dimensionalizing the vortex length L along the upstream channel by the channel width w = 110 μm. In Figure 5-6(b), we replot the dimensionless vortex length versus M_s. Included in Figure 5-6 are data from both ramps up and ramps down in Wi; we see no evidence of hysteresis in the vortex length or critical conditions. Also included are the data reported for a similar fluid from our previous work.[21]

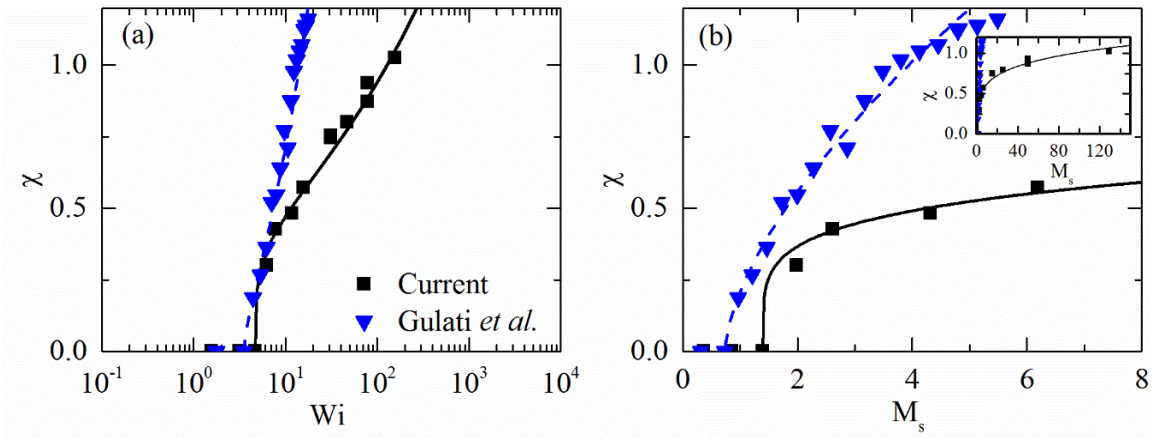

Figure 5-6. (a) Semi-log plot of dimensionless vortex length χ for the PEO solution in a 90° micro-bend with w = 110 and h = 70 µm (current) and a very similar solution (PEO2) in a w = 200 and h = 225 µm micro-bend[21] as a function of Wi. The vortex length in the current geometry follows the functional form $\chi = 0.3165(\text{Wi}-\text{Wi}_{crit})^{0.239}$, where Wi_{crit} is 4.72. (b) Dimensionless vortex length for PEO solutions in a 90° micro-bend as a function of M_s. The vortex length in the current geometry follows the functional form $\chi = 0.406(M_s - M_{s,crit})^{0.199}$, where $M_{s,crit}$ is 1.40.

Our earlier work was in a microfluidic bend with channels of widths w = 200 µm and heights of h = 225 µm, and (as noted in the introduction) considered a highly shear-thinning DNA solution, a PEO solution (PEO2) that was very similar to the present PEO solution, and a non-shear-thinning PEO solution. While the dimensionless vortex growth for the two cases shown in Figure 5-6 is comparable, we note that it is not identical. Both the critical condition $M_{s,crit}$ and the rate of vortex growth with increasing M_s differ. In our earlier work, although shear-thinning was required for the appearance and growth of the corner vortex, we found only a modest dependence of $M_{s,crit}$ on the degree of shear-thinning, with $M_{s,crit}$ varying from 0.54 for the DNA solution with a power law exponent of 0.187, to $M_{s,crit}$ = 0.73 for the solution PEO2 with a power law index of 0.878. Hence, we expect that the difference between the critical conditions for the two PEO solutions shown in Figure 5-6(b) ($M_{s,crit}$ = 0.73 for PEO2 and $M_{s,crit}$ = 1.40 for the PEO solution in the current geometry) is likely due to the difference in aspect ratio (h/w) for these two cases (0.636 in this work versus 1.125 in the work of Gulati *et al.*[21]). The differences in the rate of vortex growth in our previous study of DNA and PEO2 solutions (*c.f.* Figure 11(b)[21]) were comparable to the differences seen here, but given the similarity of the two PEO solutions, we anticipate that the lower vortex growth rate in the present work is also due to the lower aspect ratio. The sensitivity of the critical conditions to aspect ratio is consistent with the results of Sousa *et al.* for the cross-slot geometry,[16] who found that lower aspect ratios stabilize the flow and shift the critical conditions to higher Wi. The slower growth rate of the vortices in the present, lower aspect ratio case is also consistent with the stabilization of the flow by the bounding walls and is consistent with trends observed for the growth of inertial vortices in contraction-expansion flow[254] and T-junctions[256] and for elastic vortex growth in planar contractions[255].

5.5.2 Linear Wormlike Micelles

We next examine a shear-thinning, viscoelastic linear wormlike micellar solution (CPCl/NaSal, R = 0.52). The streak images are shown in Figure 5-7 below.

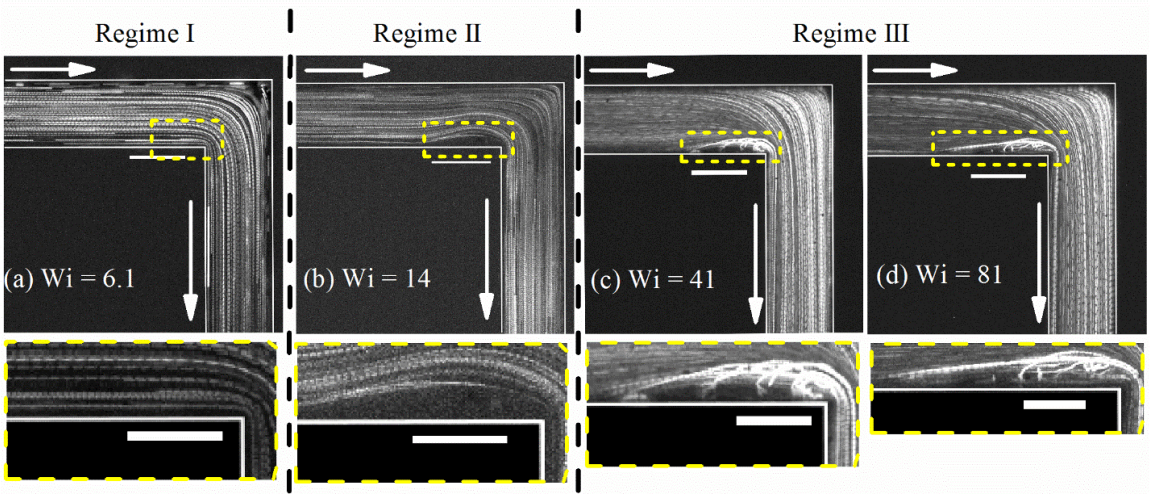

Figure 5-7. Streak images of flow in the abrupt micro-bend for the linear wormlike micellar solution CPCl/NaSal, R = 0.52, displaying three behaviors. (a) Regime I: No vortex, Re = 4.3×10^{-5}, Wi = 6.1, El = 9.2×10^{4}, (b) Regime II: steady vortex at the inner corner, Re = 2.1×10^{-4}, Wi = 14, El = 6.9×10^{4}, and (c-d) Regime III: time-dependent vortex at inner corner, (c) Re = 1.4×10^{-3}, Wi = 41, El = 2.9×10^{4}, (d) Re = 4.97×10^{-3}, Wi = 81, El = 1.6×10^{4}. Figure scale bars are 100 μm. Inset scale bars are 50 μm.

The flow exhibits three different flow regimes as Wi is increased. Initially, the flow is steady and there is no vortex at low flow rates (regime I). Once the critical threshold for the onset of vortex formation is reached, between Wi = 6 and 8, a stable vortex forms (regime II). The vortex grows but remains steady and time-independent through Wi = 20. Unlike in the PEO solution flow, there is a second critical Wi in the range $20 < Wi < 41$. By Wi = 41, the vortex becomes time-dependent and fluctuates in length over time. This can be seen in Figure 5-7(c) and (d), where the vortex is composed of a series of streaks with different leading edges and streak lines that intersect within the vortex (indicating the time-dependent nature of the flow). Figure 5-8 shows the vortex length L over time for five flow rates. Initially, the vortex length L remains steady in time, as shown in Figure 5-8 for Wi = 10 and 14; these measurements of L (as a function of time) have an average standard deviation that is 4% of the mean value of L. For Wi = 41 and above, however, the vortex length variation increases, with the difference between the maximum and minimum values of the vortex length reaching approximately 30% of the mean. This increase in the difference between the maximum and minimum vortex length characterizes the transition from regime II to regime III.

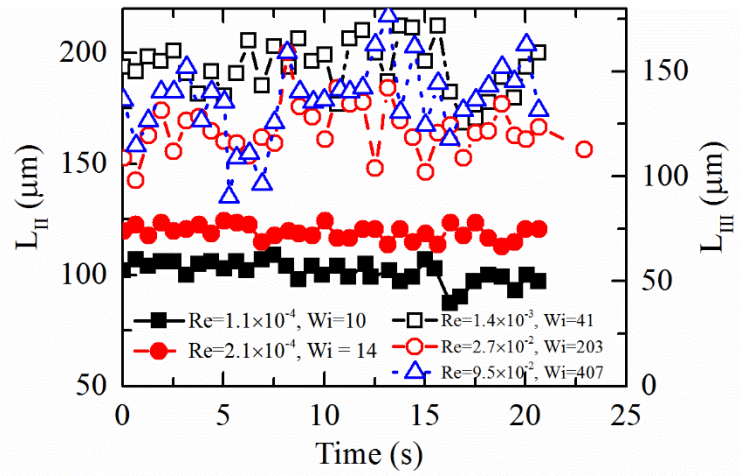

Figure 5-8. Vortex length as a function of time for the linear wormlike micellar solution, CPCl/NaSal, R = 0.52. Stationary (II) and time-dependent (III) vortex behavior plots are offset by 50 μm (as indicated in the left and right vertical axis scales, respectively) for visual clarity. Filled markers indicate steady vortex lengths, read on the left vertical axis. Open markers indicate time-varying vortex lengths, read on the right vertical axis.

Figure 5-9 shows the dimensionless vortex length as a function of Wi and M_s for all three regimes suggested in Figure 5-7. To indicate the steady or unsteady nature of the vortices, the average dimensionless vortex length is plotted with the minimum and maximum on either end of the bars. Over sections I and II, the behavior of the vortex length is similar to that of the PEO solution. The onset of vortex formation occurs at M_s between 0.97 and 1.2, which is very close to $M_{s,crit} = 1.40$ for the PEO solution. However, at higher flow rates (M_s between 2.3 - 3.7), a second transition from a steady vortex to an unsteady vortex (III) is observed for the linear wormlike micellar solution. For regime III, the variation in the vortex length increases dramatically compared to regime II, while the average vortex size remains roughly constant. We note that a similar transition from steady to unsteady vortex dynamics is not reported for the PEO solution at comparable or much higher M_s ($5 < M_s < 129$) in our microfluidic geometry. Similarly, no transition to unsteady vortex flow was observed in our earlier study of a shear-thinning DNA solution at the highest M_s considered (maximum $M_s = 5.2$ for the DNA solution).[21]

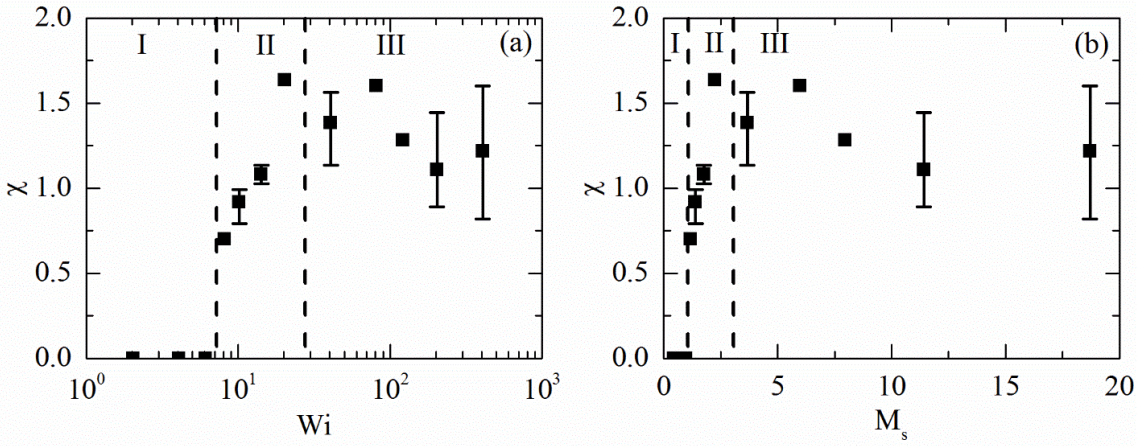

Figure 5-9. (a) Semi-log plot of dimensionless vortex length for linear wormlike micelles, CPCl/NaSal, R = 0.52, in a 90° micro-bend as a function of Wi. (b) Dimensionless vortex length for linear wormlike micelles, R = 0.52, in a 90° micro-bend as a function of M_s. The behavior of the flow is split into three regimes: (I) no vortex formation, (II) stable vortex, and (III) vortex with unsteady behavior. The bars indicate the range of minimum to maximum vortex length measured over a period of ~20 seconds. Data points with no bars are vortex lengths taken directly from a streak image that have been averaged over 0.2 to 4 seconds.

A primary difference between the PEO solution and the linear wormlike micellar solution is that the structure of wormlike micelles has been long known to break and reform under shear.[96] The change in the structure of the wormlike micellar chains under shear should affect the secondary flow of wormlike micelles and, in this case, may result in the variation in the vortex size with time. We suggest a mechanism such as follows: as we increase the flow rate, the wormlike micellar chains break due to the high shear rate experienced locally on the scale of a chain, and this reduces the effective Wi or M_s through lowering the relaxation time and the effective viscosity over a certain period of time. At this point in time, the vortex length goes through a minimum. As the wormlike micellar chains start to reform, the effective viscosity and the relaxation time increase due to the longer chain lengths. This in turn leads to higher effective Wi or M_s values that give rise to a larger vortex size. This explanation at present is speculative and could perhaps be probed through a combination of particle image velocimetry and flow birefringence to examine the relationship between the flow field and micelle reformation.

Another important difference between the PEO and wormlike micelles with R = 0.52 is the ratio of solvent viscosity to the zero shear rate solution viscosity. As shown in Table 5-1, this ratio is roughly 0.26 for the PEO solution and of order 10^{-4} for the two wormlike micellar solutions. Thus, the higher Newtonian solvent contribution to the stress for the PEO solution may play a role in stabilizing the flow against the second transition, although it appears to have little impact on the first transition (where $M_{s,crit}$ values are comparable for the PEO and linear wormlike micellar solution). For comparison, we note that Sousa *et al.*[16] found that for solutions of polyacrylamide, the transitions observed in the cross slot were sensitive to the solvent viscosity ratio. In

those experiments, at high values of the solvent viscosity ratio, the first transition was from steady, symmetric flow to unsteady flow, while for low values, the first transition was to a steady, asymmetric flow. An interesting contrast between the 90º bend studies here and the cross slot results in the literature is that while we observe the second transition from steady to unsteady vortex flows in the micro-bend *only* for wormlike micellar solutions, in the cross-slot a second transition from steady to unsteady flow is observed for both flexible polymers and wormlike micellar solutions under appropriate conditions of aspect ratio and elasticity.[16,23,114,261] We plan to fully explore the role of solvent viscosity ratio and chain breakage time scales in future work.

5.5.3 Branched Wormlike Micelles

A branched wormlike micellar solution (CPCl/NaSal, R = 0.75) is run through the 90º micro-bend at a range of flow rates to obtain Wi from 4 to 400. Unlike the linear wormlike micellar solution and the PEO solution, this solution does not form steady vortices over this range of Wi. The streak images in Figure 5-10 illustrate the three regimes that the flow manifests. At low Wi (regime I), the streamlines reveal no vortices and the flow is consistent with the low Wi behavior of the other solutions. At the first critical Wi (between 4 and 6), intermittent vortices form at the inner lip and outer corner (Figure 5-10, regime II). These vortices cycle through periods of no vortex, a single vortex at the inner lip or outer corner only, and both upstream inner corner (lip) and outer corner vortices being present. This is shown in Figure 5-11(a), which plots regime II lip vortex length L_{II} over time for Wi = 20. Over the 200 seconds included in Figure 5-11(a), vortices form sporadically, with periods of no vortices. The sporadic nature of the vortices continues with increasing Wi. As Wi increases, the vortices are sustained for longer periods of time until the second threshold is reached between Wi of 160 and 180. At this point, the outer corner vortex no longer forms, and the inner (lip) vortex remains unsteady. This is illustrated in Figure 5-10, regime III, where there are three streak images from a series of images taken at the same Wi that show different vortex lengths. An example of the lip vortex length L_{III} over time in regime III is shown in Figure 5-11(b), where the outer vortex has vanished and the length of the lip vortex changes significantly over 45 seconds.

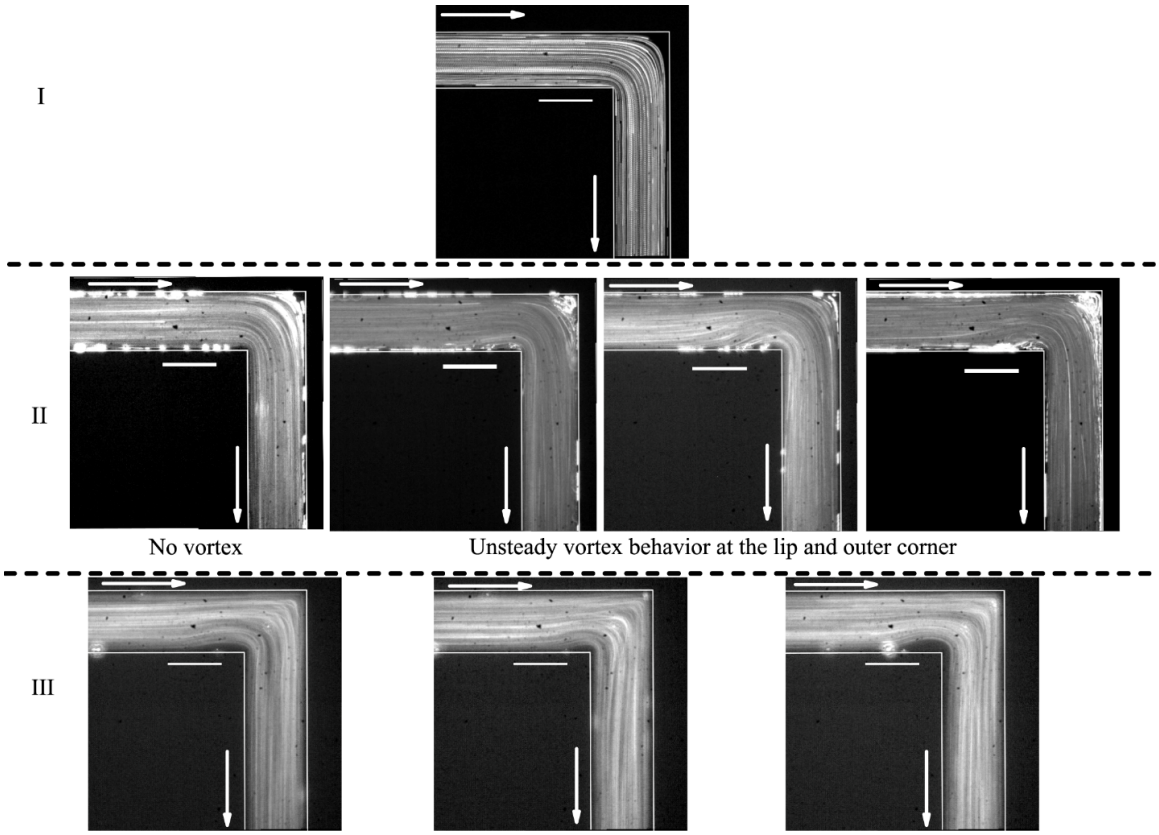

Figure 5-10. Streak images of the branched wormlike micellar solution, R = 0.75, in the sharp micro-bend, which displays three behaviors. I: No vortex (Wi = 4), II: unsteady vortex behavior with lip and outer vortices fluctuating in size (Wi = 100), and III: Unsteady lip vortex at upstream inner corner (Wi = 200) at different times.

The ranges of non-dimensional inner lip vortex lengths observed as a function of Wi and M_s are shown in Figure 5-12, with the three flow regimes indicated. The first transition between no vortex and intermittent vortices occurs between Wi = 4 and 6. This is equivalent to $M_{s,crit}$ between 2.5 and 3.8, which is higher than the $M_{s,crit}$ for both the PEO and the linear wormlike micellar solutions. The second transition occurs between Wi =160 and 180 and M_s = 135 and 153.

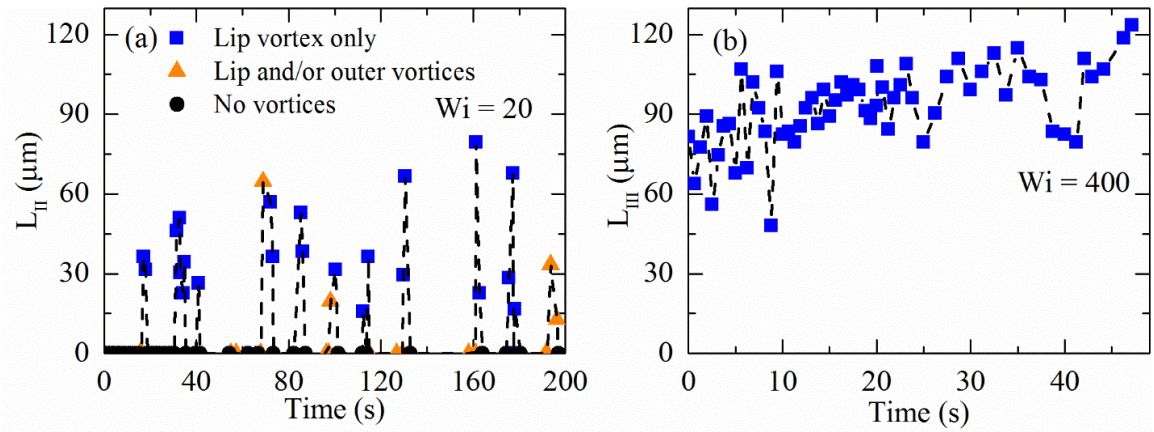

Figure 5-11. Lip vortex length in regime II (L_{II}) or in regime III (L_{III}) as a function of time. Orange triangles indicate the inner (lip) vortex length in the case where an outer corner vortex is also present. In all other cases, only an inner vortex is present. (a) Regime II: unsteady vortex behavior switching among no vortex at all, a single vortex only at the inner edge (lip), a vortex at the outer corner only, and vortices at both the lip and outer corner at Wi = 20. L_{II} is the length of the inner lip vortex. (b) Regime III: length L_{III} of the unsteady lip vortex at the inner corner at Wi=400.

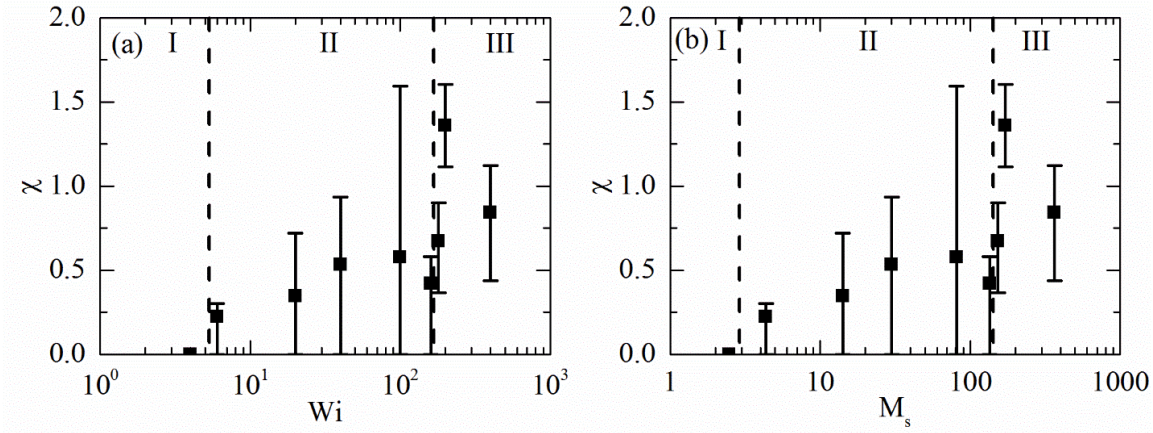

Figure 5-12. (a) Semi-log plot of dimensionless inner lip vortex length for branched wormlike micelles, R = 0.75, in a 90o micro-bend as a function of Wi. (b) Dimensionless inner lip vortex length for branched wormlike micelles, R = 0.75, in a 90o micro-bend as a function of Ms. The bars indicate the range from minimum to maximum inner vortex length measured over a period of 20 to 200 seconds.

As noted before, we expect the wormlike micelles in the CPCl/NaSal solution with R = 0.75 to have a branched rather than a linear structure, and this difference no doubt contributes significantly to the differences in the stability of flow in the micro-bend between the two CPCl/NaSal solutions. The solution with R = 0.75 also clearly shows a plateau in the steady shear rheological measurements, whereas the linear wormlike micelles with R = 0.52 lack such a feature (*cf.* Fig. 5-3(b)). Therefore, the

difference in transitions between these two wormlike micellar solutions in the micro-bend geometry might be attributed to their different mechanical responses in the steady shear measurements. From the steady shear measurements, we can divide the mechanical response of the wormlike micellar solution with R = 0.75 into three regions. The first region corresponds to shear rates that fall below the onset of shear banding, i.e. $\dot{\gamma} < 3.5\ s^{-1}$, Wi < 2.1. The second region corresponds to the shear-banding region, $3.5\ s^{-1} < \dot{\gamma} < 26\ s^{-1}$, 2.1 < Wi < 16, and the third to the high shear rate, shear-thinning region at $\dot{\gamma} > 26\ s^{-1}$, Wi > 16. Thus, while shear banding may influence the first transition between no vortices and intermittent vortices, the characteristic shear rates at the second transition in the micro-bend device are well past the shear-banding plateau. Moreover, although the selection of the two wormlike micellar solutions used in the present work was motivated by our interest in considering the effect of linear versus branched topologies over a comparable range of Wi (and thus we chose two fluids with similar relaxation times), we plan future studies in which we examine the role of shear-banding independent of branching on flow in the micro-bend.

5.6 Conclusions

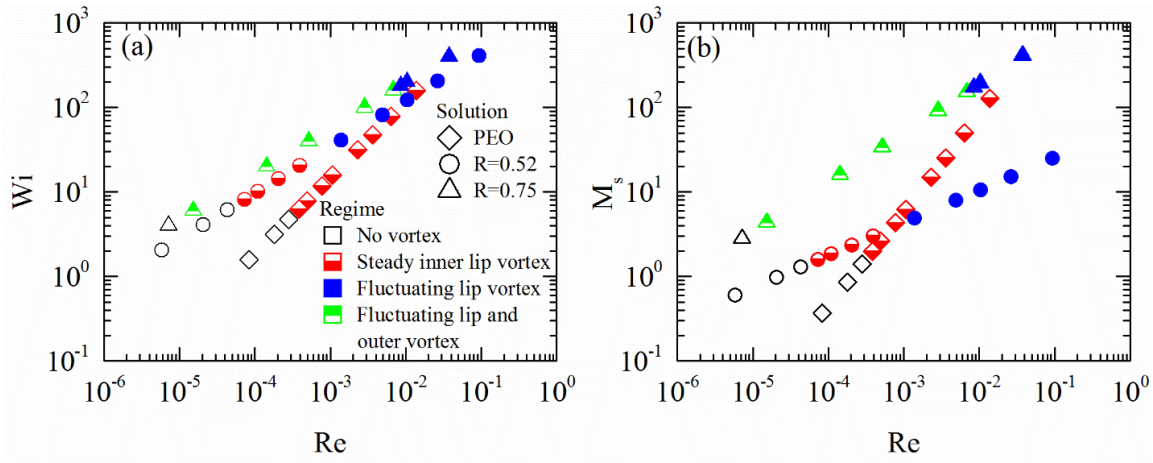

Figure 5-13. (a) Log-log plot of Wi as a function of Re and (b) log-log plot of Ms as a function of Re for all solutions examined. The shape of the symbol indicates the solution while the color and fill of the symbol indicate the flow behavior.

Figure 5-13 summarizes the main results of our study and offers a direct comparison of the three fluids examined. From Figure 5-13(a), it is apparent that a) we have covered a comparable range of Wi for all fluids, b) that the degrees of shear thinning of the viscosity (and hence the slopes of the curves on Wi versus Re coordinates) are comparable for the two wormlike micelle solutions (although differences in the magnitudes of the viscosity between these two fluids result in the two curves being shifted slightly horizontally), and c) that the first transition occurs at comparable Wi for all three fluids, namely Wi in the range of 4 to 8.

For the PEO solution, beyond a critical threshold $Wi_{crit} \approx 4.7$, $M_{s,crit} \approx 1.40$, the steady base flow is replaced by a secondary flow that is characterized by the formation of a stationary lip vortex. Although our results are similar to prior observations by Gulati *et al.*[21] on similar PEO solutions, the critical threshold for the onset of vortices is shifted to slightly higher values, and the growth of the lip vortex with Wi is slower. This is perhaps not surprising since the aspect ratio of this microfluidic geometry is lower than the one used by Gulati *et al.*[21,22] The higher critical threshold and the slower growth rate at lower aspect ratio are consistent with the results of Sousa *et al.*[16] for flow of polymer solutions in cross-slot geometries and are consistent with the stabilization of inertial vortices by the bounding walls as observed in other geometries.[254–256]

As can be seen from Figure 5-13(a), although the nature of the first transition is similar for the PEO and the linear wormlike micelle solution (from no vortex to a steady inner lip vortex), the linear wormlike micelle solution displays a second transition to a fluctuating lip vortex over a range of parameters where the PEO solution continues to show steady vortex behavior. The branched wormlike micelle solution shows very different transitions from the other two solutions, showing first a transition to fluctuating lip and outer corner vortices followed by a transition to fluctuating lip vortices at high Wi. The difference in flow transitions between the two wormlike micellar solutions may originate from their structures (linear versus branched) and from the contrast in their steady shear response (non-shear-banding versus shear-banding).

Figure 5-13(b) displays the same data replotted on M_s versus Re coordinates. Here, the differences in the shear-rate dependence of the first normal stress coefficient and in the ratio of the solvent viscosity to the zero shear rate viscosity between fluids are highlighted by the varying slopes and ranges of M_s covered. It is worth noting that on these coordinates (i.e., in terms of M_s rather than Wi), the variation in the critical condition for the first transition is a bit greater, indicating that our purely elastic criterion is not completely capturing the critical condition across this range of rheological variation. In future studies, we plan to explore the role of the solvent viscosity ratio – which may play a role in the differences between the PEO solutions and the wormlike micellar solutions – and the role of shear banding by examining solutions of linear wormlike micelles that display shear banding.

5.7 Acknowledgements

This work was supported in part by a grant from the National Science Foundation (Award CBET 1335653) and through a grant from ACS PRF (Award 53143-ND9). MYH was also supported through a National Science Foundation Graduate Research Fellowship. The authors are also grateful to Malvern Instruments for the loan of the Malvern Gemini rheometer.

6 Conclusions and Future Work

6.1 Conclusions

The main objective of this work is to explore complex fluid flows with microfluidic systems, specifically exploring the dynamics of suspensions and wormlike micellar solutions. Several aspects have been investigated, including optimization of a flow-focusing design to generate a large library of particles with varying parameters, namely size, shape, and stiffness, the potential of using soft particle deformation in flow to determine particle stiffness, and the development of elastic instabilities of wormlike micelles in sharp corners. The variety of applications explored in this work showcases the versatility of microfluidic approaches. Understanding the flow and behavior of non-Newtonian fluids has important implications for many industries such as oil and pharmaceuticals.

There is an assortment of monodisperse particles generated in this work, including non-spherical, non-symmetric particles such as teardrop or bowl shaped, particles made of different materials (pNIPAM or alginate), and ones with a wide range of moduli spanning three orders of magnitude. The shear and compressive moduli were obtained with capillary micromechanics. The optimized flow focusing device design for particle generation allowed for prolonged use. Of note is the versatility of the device—no modification was needed to generate particles requiring different chemistries. The ability to generate large, well-controlled populations of particles is relevant to fundamental suspension dynamics studies, drug delivery particle development, and model studies for cell separation and characterization.

The generated particles were then used to examine their behavior in flow; particularly, the pNIPAM particles have shear moduli averaging 13 Pa to 384 Pa, which is soft enough to access Ca where particle deformation is significant. The deformation and shape transitions in a confined microchannel with a rectangular cross section were quantified for the two softest pNIPAM particle types. They had similar shape transitions at equivalent Ca, going from circular to egg, triangular, arrowhead, and finally parachute-shaped as Ca increased. These shapes are distinct from those observed for vesicles and capsules in confined flow. At the limit of high circularity (circular and egg-shaped), the curvature at the tip changed considerably with changing Ca. As circularity deviated from 1, though, the changes in radius of curvature decreased and circularity became the defining parameter with respect to Ca. By quantifying the circularity and radius of curvature at the leading edge of the particle, it is possible to obtain the corresponding Ca and thus shear modulus for individual particles. As characterizing stiffness of small objects on the order of tens and hundreds of microns

is more difficult than characterizing macroscale properties, this method of analyzing deformation in flow could be advantageous. In addition, the particles are robust even as they deform dramatically, indicating that their application to drug delivery would be different from those of capsules, which rupture at high shear rates.

Finally, elastic instabilities and flow transitions were examined in a sharp 90º microfluidic bend geometry for a range of shear-thinning, viscoelastic fluids, including a linear flexible polymer solution based on PEO and two CPCl/NaSal wormlike micellar solutions with different salt to surfactant concentration ratios. All three solutions were examined over similar ranges of Wi. The results for the PEO solution were consistent with Gulati *et al.*,[21] where the steady base flow is replaced by a secondary flow characterized by a stationary lip vortex. On the other hand, the flow of both wormlike micellar solutions underwent two transitions; this difference might be due to the wormlike micellar breakage and reformation under flow. The shear-thinning solution of linear wormlike micelles first developed a steady lip vortex which then became time-dependent above a second critical Wi. The shear-banding solution of branched wormlike micelles first transitioned to intermittent formation of inner lip and outer corner vortices. The second transition resulted in only the lip vortex upstream of the bend that fluctuates in size with time. These wormlike micellar solutions had different rheologies and structures that could contribute to the different regime behaviors.

6.2 Future Work

6.2.1 Generation and Examination of Microparticles in Flow

Additional work on generating and optimizing particles could provide a broader range of tunable parameters. For example, generating and characterizing particles on the cellular length scale (~10 μm), additional asymmetric shapes, or capsules with a liquid core and elastic membrane could provide additional insight into suspended component flow behavior. As the pNIPAM particles are sensitive to environmental cues, further work could also be done on characterizing the particle responses to various stimuli such as suspending media and temperature. Controlling these changes would be useful for developing sensors and targeted or environmentally-controlled drug release.

With the library of particles generated, the effect of shape and deformability could be examined in flows other than confined high aspect ratio rectangular channels. First, non-inertial lateral migration can occur when asymmetry breaks the reversibility of Stokes' equation, so particularly non-spherical shapes could potentially display interesting behavior in low Re flow. Further, shape and deformation can couple with inertia and affect equilibrium positions,[48,77] so the variety of shapes and moduli of the particles generated can be used to explore inertial migration and focusing length. Preliminary work has been done in examining the effect of particle deformation and

shape on inertial migration equilibrium positions for a range of Re, summarized in Figure 6-2. In this plot, the non-dimensionalized lateral focusing position X_{eq}, determined for particles at a position far downstream in the channel (~80 mm), is plotted as a function of non-dimensional particle size D_{max}/W, where D_{max} is the maximum diameter of the particle and W is the width of the channel. For flow in the x-direction, the lateral equilibrium position X_{eq} is defined as $d_{wall}/(W/2)$, where d_{wall} is the distance between the particle center and the closest channel wall in the y-direction (Fig. 6-1); X_{eq} is equal to 0 at the wall and 1 at the channel centerline. Hur *et al.*[48] concluded that X_{eq} for rigid particles is generally linearly related to D_{max}/W, with the fit shown as a dotted line on Figure 6-2. The teardrops, shown as red triangles, are slightly below the fit, indicating equilibrium positions slightly closer to the walls than rigid spherical particles of equivalent size, whereas pNIPAM particles, shown as blue squares, focus to a position far closer to the center of the channel than equivalent rigid particles. These preliminary results imply that there may be a combination of shape and deformation effects on equilibrium position, as asymmetry seems to result in the teardrops migrating closer to the wall, but deformation shifts the pNIPAM particles toward the center. More work needs to be done to have a full systematic examination of the effect of shape and deformable but solid elastic particles on inertial migration position and focusing length.

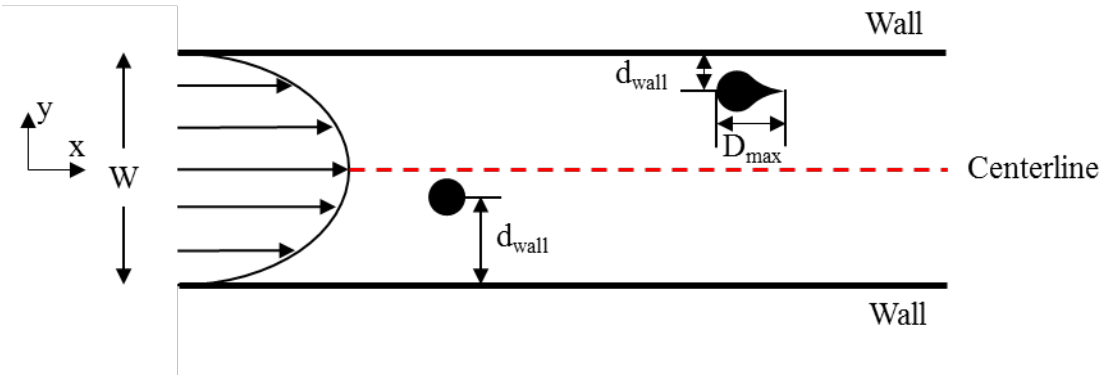

Figure 6-1. Schematic showing the top-down view of a channel and experimental parameters for inertial migration experiments.

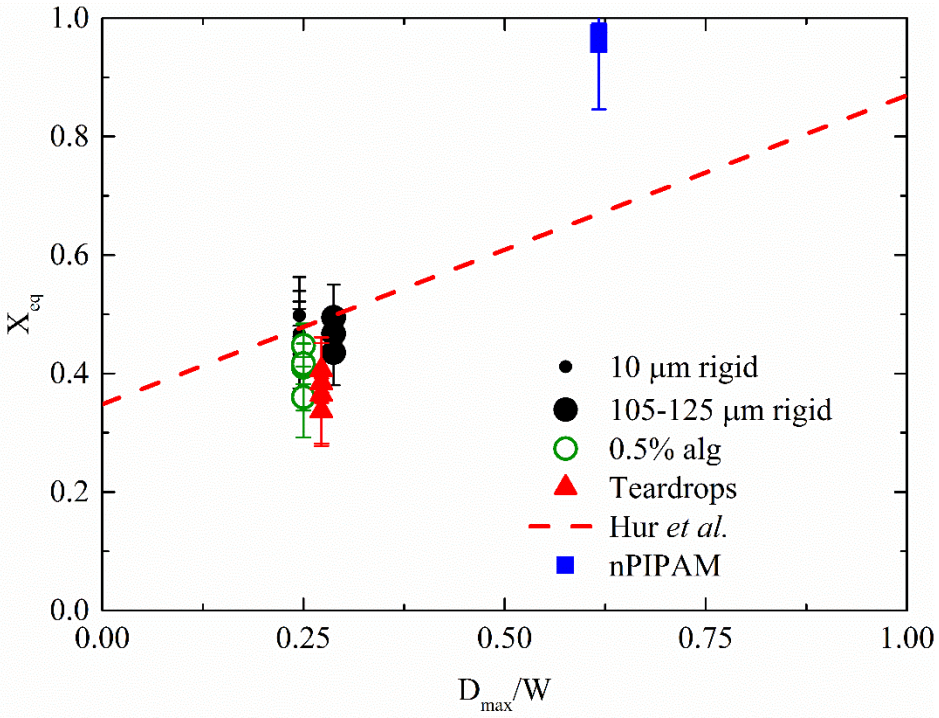

Figure 6-2. Comparison of non-dimensionalized equilibrium positions for inertially focused particles (markers) compared to a fit from Hur *et al.*[48] for migration trends of rigid particles. $X_{eq} = 0$ is the wall and $X_{eq} = 1$ is the centerline of the channel.

The softest pNIPAM particles with an average shear modulus of 13 Pa could potentially be used for experiments at low Re as well. With a sufficiently viscous carrying fluid, it may be possible to reach Ca ~0.1, resulting in non-negligible deformation. In this case, all lateral migration would be driven by deformation. Lower flow rates provide the possibility of single particle tracking experiments, where the lateral migration profile is obtained for an individual particle. Single particle tracking has previously been done for vesicles by Coupier *et al.*,[82] but similar studies have yet to be performed on deformable particles. Some preliminary work has been done on tracking single deformable particles using the suite of particles generated in this dissertation, but only with alginate particles, where Ca < 10^{-4}, which results in negligible deformation and no lateral migration. If high flow rates are needed, the same method as the one used for characterizing inertial migration could be used, where distribution profiles are obtained at multiple downstream lengths.

As particle deformation shape in confined flow is a good measure of deformability, it may be possible to combine particle generation and characterization into a single device and approximate an effective shear modulus in line. For example, adding a constricted channel at the end of the particle generation channel could result in particle deformation. An additional set of inlets at the end of the gelation channel could increase and control the shear rate to reach sufficient Ca for deformation. To avoid clogging and/or breakup, a preliminary step could be necessary, where particle

generation conditions are initially optimized in a device without the constriction. This could also provide a measure of extent of gelation or population homogeneity.

6.2.2 Stability of Wormlike Micelle Solutions in a High El Flow

As noted earlier, the PEO solution and the linear wormlike micellar solution transitioned to a similar regime with a steady lip vortex, but the linear WLM solution then developed time-dependent behavior at higher Wi. As this difference could arise from the contribution of the breaking and reforming of micelles and also from the solvent viscosity ratio, exploring different solutions that examine the effect of solvent viscosity ratio could help elucidate what drives the time-dependent behavior in wormlike micellar solutions. Furthermore, the wormlike micellar solutions examined were different in both structure (linear versus branched) and non-linear rheological response (non-shear-banding versus shear-banding). Future studies examining shear-banding wormlike micellar solutions with linear micelles could clarify the behavior. This can be done by changing the salt-to-surfactant concentration of the CPCl/NaSal solutions.

References

1 G. M. Whitesides, The origins and the future of microfluidics, *Nature*, 2006, **442**, 368–373.

2 D. T. Chiu, A. J. deMello, D. Di Carlo, P. S. Doyle, C. Hansen, R. M. Maceiczyk and R. C. R. Wootton, Small but Perfectly Formed? Successes, Challenges, and Opportunities for Microfluidics in the Chemical and Biological Sciences, *Chem*, 2017, **2**, 201–223.

3 A. A. Werdich, E. A. Lima, B. Ivanov, I. Ges, M. E. Anderson, J. P. Wikswo and F. J. Baudenbacher, A microfluidic device to confine a single cardiac myocyte in a sub-nanoliter volume on planar microelectrodes for extracellular potential recordings., *Lab Chip*, 2004, **4**, 357–362.

4 H. Zohar, C. L. Hetherington, C. Bustamante and S. J. Muller, Peptide nucleic acids as tools for single-molecule sequence detection and manipulation, *Nano Lett.*, 2010, **10**, 4697–4701.

5 R. Dylla-Spears, J. E. Townsend, L. Jen-Jacobson, L. L. Sohn and S. J. Muller, Single-molecule sequence detection via microfluidic planar extensional flow at a stagnation point, *Lab Chip*, 2010, **10**, 1543.

6 J. Shendure and H. Ji, Next-generation DNA sequencing, *Nat. Biotechnol.*, 2008, **26**, 1135–1145.

7 Y. Marcy, T. Ishoey, R. S. Lasken, T. B. Stockwell, B. P. Walenz, A. L. Halpern, K. Y. Beeson, S. M. D. Goldberg and S. R. Quake, Nanoliter reactors improve multiple displacement amplification of genomes from single cells, *PLoS Genet.*, 2007, **3**, 1702–1708.

8 D. S. Boyle, K. R. Hawkins, M. S. Steele, M. Singhal and X. Cheng, Emerging technologies for point-of-care CD4 T-lymphocyte counting, *Trends Biotechnol.*, 2012, **30**, 45–54.

9 P. Gascoyne, J. Satayavivad and M. Ruchirawat, Microfluidic approaches to malaria detection, *Acta Trop.*, 2004, **89**, 357–369.

10 H. Wei Hou, H. Y. Gan, A. A. S. Bhagat, L. D. Li, C. T. Lim, J. Han, H. W. Hou, H. Y. Gan, A. A. S. Bhagat and L. D. Li, A microfluidics approach towards high-throughput pathogen removal from blood using margination, *Biomicrofluidics*, 2012, **6**, 1–13.

11 D. Huh, H. J. Kim, J. P. Fraser, D. E. Shea, M. Khan, A. Bahinski, G. A. Hamilton and D. E. Ingber, Microfabrication of human organs-on-chips, *Nat. Protoc.*, 2013, **8**, 2135–2157.

12 M. T. Guo, A. Rotem, J. A. Heyman and D. A. Weitz, Droplet microfluidics for high-throughput biological assays, *Lab Chip*, 2012, **12**, 2146.

13 D. Di Carlo, Inertial microfluidics, *Lab Chip*, 2009, **9**, 3038.

14 J. Zhou and I. Papautsky, Fundamentals of inertial focusing in microchannels., *Lab Chip*, 2013, **13**, 1121–32.

15 L. E. Rodd, T. P. Scott, D. V. Boger, J. J. Cooper-White and G. H. McKinley, The inertio-elastic planar entry flow of low-viscosity elastic fluids in micro-fabricated geometries, *J. Nonnewton. Fluid Mech.*, 2005, **129**, 1–22.

16 P. C. Sousa, F. T. Pinho, M. S. N. Oliveira and M. A. Alves, Purely elastic flow instabilities in microscale cross-slot devices, *Soft Matter*, 2015, **11**, 8856–8862.

17 R. J. Poole, M. A. Alves and P. J. Oliveira, Purely elastic flow asymmetries, *Phys. Rev. Lett.*, 2007, **99**, 1–4.

18 S. J. Haward and G. H. McKinley, Instabilities in stagnation point flows of polymer solutions, *Phys. Fluids*, 2013, **25**, 83104.

19 J. Zilz, R. J. Poole, M. A. Alves, D. Bartolo, B. Levaché and A. Lindner, Geometric scaling of a purely elastic flow instability in serpentine channels, *J. Fluid Mech.*, 2012, **712**, 203–218.

20 R. J. Poole, A. Lindner and M. A. Alves, Viscoelastic secondary flows in serpentine channels, *J. Nonnewton. Fluid Mech.*, 2013, **201**, 10–16.

21 S. Gulati, C. S. Dutcher, D. Liepmann and S. J. Muller, Elastic secondary flows in sharp 90 degree micro-bends: A comparison of PEO and DNA solutions, *J. Rheol.*, 2010, **54**, 375–392.

22 S. Gulati, D. Liepmann and S. J. Muller, Elastic secondary flows of semidilute DNA solutions in abrupt 90° microbends, *Phys. Rev. E*, 2008, **78**, 1–5.

23 P. E. Arratia, C. C. Thomas, J. Diorio and J. P. Gollub, Elastic instabilities of polymer solutions in cross-channel flow, *Phys. Rev. Lett.*, 2006, **96**, 12–15.

24 T. Burghelea, E. Segre, I. Bar-Joseph, A. Groisman and V. Steinberg, Chaotic flow and efficient mixing in a microchannel with a polymer solution, *Phys. Rev. E*, 2004, **69**, 1–8.

25 P. Garstecki, M. J. Fuerstman, H. a Stone and G. M. Whitesides, Formation of droplets and bubbles in a microfluidic T-junction-scaling and mechanism of break-up., *Lab Chip*, 2006, **6**, 437–46.

26 G. F. Christopher and S. L. Anna, Microfluidic methods for generating continuous droplet streams, *J. Phys. D. Appl. Phys.*, 2007, **40**, R319–R336.

27 S. L. Anna and H. C. Mayer, Microscale tipstreaming in a microfluidic flow focusing device, *Phys. Fluids*, 2006, **18**, 121512.

28 A. S. Utada, Monodisperse Double Emulsions Generated from a Microcapillary Device, *Science*, 2005, **308**, 537–541.

29 H. Zhang, E. Tumarkin, R. Peerani, Z. Nie, R. M. A. Sullan, G. C. Walker and E. Kumacheva, Microfluidic Production of Biopolymer Microcapsules with Controlled Morphology, *J. Am. Chem. Soc.*, 2006, **128**, 12205–12210.

30 P. Voudouris, D. Florea, P. van der Schoot and H. M. Wyss, Micromechanics of temperature sensitive microgels: dip in the Poisson ratio near the LCST, *Soft Matter*, 2013, **9**, 7158–7166.

31 Y. Hu, Q. Wang, J. Wang, J. Zhu, H. Wang and Y. Yang, Shape controllable microgel particles prepared by microfluidic combining external ionic crosslinking, *Biomicrofluidics*, 2012, **6**, 26502.

32 D. Dendukuri, K. Tsoi, T. A. Hatton and P. S. Doyle, Controlled synthesis of nonspherical microparticles using microfluidics, *Langmuir*, 2005, **21**, 2113–2116.

33 R. Haghgooie, M. Toner and P. S. Doyle, Squishy non-spherical hydrogel microparticles, *Macromol. Rapid Commun.*, 2010, **31**, 128–134.

34 C. Kim, S. Chung, Y. E. Kim, K. S. Lee, S. H. Lee, K. W. Oh and J. Y. Kang, Generation of core-shell microcapsules with three-dimensional focusing device for efficient formation of cell spheroid., *Lab Chip*, 2011, **11**, 246–252.

35 W. Drenckhan, S. J. Cox, G. Delaney, H. Holste, D. Weaire and N. Kern, Rheology of ordered foams - On the way to Discrete Microfluidics, *Colloids Surfaces A Physicochem. Eng. Asp.*, 2005, **263**, 52–64.

36 M. Hashimoto, P. Garstecki and G. M. Whitesides, Synthesis of composite emulsions and complex foams with the use of microfluidic flow-focusing devices, *Small*, 2007, **3**, 1792–1802.

37 A. Huerre, V. Miralles and M.-C. Jullien, Bubbles and foams in microfluidics, *Soft Matter*, 2014, **10**, 6888–6902.

38 X. Niu and A. J. deMello, Building droplet-based microfluidic systems for biological analysis, *Biochem. Soc. Trans.*, 2012, **40**, 615–623.

39 B. L. Wang, A. Ghaderi, H. Zhou, J. Agresti, D. A. Weitz, G. R. Fink and G. Stephanopoulos, Microfluidic high-throughput culturing of single cells for selection based on extracellular metabolite production or consumption, *Nat. Biotechnol.*, 2014, **32**, 473–478.

40 W. Lee, L. M. Walker and S. L. Anna, Role of geometry and fluid properties in

droplet and thread formation processes in planar flow focusing, *Phys. Fluids*, 2009, **21**, 32103.

41 Z. Nie, M. Seo, S. Xu, P. C. Lewis, M. Mok, E. Kumacheva, G. M. Whitesides, P. Garstecki and H. A. Stone, Emulsification in a microfluidic flow-focusing device: effect of the viscosities of the liquids, *Microfluid. Nanofluidics*, 2008, **5**, 585–594.

42 P. Garstecki, H. A. Stone and G. M. Whitesides, Mechanism for flow-rate controlled breakup in confined geometries: A route to monodisperse emulsions, *Phys. Rev. Lett.*, 2005, **94**, 1–4.

43 C. Zhou, P. Yue and J. J. Feng, Formation of simple and compound drops in microfluidic devices, *Phys. Fluids*, 2006, **18**, 92105.

44 J. B. Dahl, V. Narsimhan, B. Gouveia, S. Kumar, E. S. G. Shaqfeh and S. J. Muller, Experimental observation of the asymmetric instability of intermediate-reduced-volume vesicles in extensional flow, *Soft Matter*, 2016, **12**, 3787–3796.

45 É. Guazzelli and J. F. Morris, *A Physical Introduction to Suspension Dynamics*, Cambridge University Press, 2011.

46 R. Toy, E. Hayden, C. Shoup, H. Baskaran and E. Karathanasis, The effects of particle size, density and shape on margination of nanoparticles in microcirculation, *Nanotechnology*, 2011, **22**, 115101.

47 A. Kumar, R. G. Henríquez Rivera and M. D. Graham, Flow-induced segregation in confined multicomponent suspensions: effects of particle size and rigidity, *J. Fluid Mech.*, 2014, **738**, 423–462.

48 S. C. Hur, S. E. Choi, S. Kwon and D. Di Carlo, Inertial focusing of non-spherical microparticles, *Appl. Phys. Lett.*, 2011, **99**, 1–4.

49 M. Masaeli, E. Sollier, H. Amini, W. Mao, K. Camacho, N. Doshi, S. Mitragotri, A. Alexeev and D. Di Carlo, Continuous Inertial Focusing and Separation of Particles by Shape, *Phys. Rev. X*, 2012, **2**, 31017.

50 A. C. Anselmo, M. Zhang, S. Kumar, D. R. Vogus, S. Menegatti, M. E. Helgeson and S. Mitragotri, Elasticity of Nanoparticles Influences Their Blood Circulation, Phagocytosis, Endocytosis, and Targeting, *ACS Nano*, 2015, **9**, 3169–3177.

51 A. C. Anselmo and S. Mitragotri, Impact of particle elasticity on particle-based drug delivery systems, *Adv. Drug Deliv. Rev.*, 2017, **108**, 51–67.

52 A. Kumar and M. D. Graham, Segregation by membrane rigidity in flowing binary suspensions of elastic capsules, *Phys. Rev. E*, 2011, **84**, 66316.

53 D. Leighton and A. Acrivos, The shear-induced migration of particles in concentrated suspensions, *J. Fluid Mech.*, 1987, **181**, 415–439.

54 P. R. Nott and J. F. Brady, Pressure-driven flow of suspensions: simulation and theory, *J. Fluid Mech.*, 1994, **275**, 157.

55 E. J. Lim, T. J. Ober, J. F. Edd, G. H. McKinley and M. Toner, Visualization of microscale particle focusing in diluted and whole blood using particle trajectory analysis., *Lab Chip*, 2012, **12**, 2199–210.

56 L. G. Leal, Particle Motions in a Viscous-Fluid, *Annu. Rev. Fluid Mech.*, 1980, **12**, 435–476.

57 S. Yang, J. Y. Kim, S. J. Lee, S. S. Lee and J. M. Kim, Sheathless elasto-inertial particle focusing and continuous separation in a straight rectangular microchannel, *Lab Chip*, 2011, **11**, 266–273.

58 K. W. Seo, H. J. Byeon, H. K. Huh and S. J. Lee, Particle migration and single-line particle focusing in microscale pipe flow of viscoelastic fluids, *RSC Adv.*, 2014, **4**, 3512–3520.

59 D. Di Carlo, D. Irimia, R. G. Tompkins and M. Toner, Continuous inertial focusing, ordering, and separation of particles in microchannels, *Proc. Natl. Acad. Sci.*, 2007, **104**, 18892–18897.

60 A. A. S. Bhagat, S. S. Kuntaegowdanahalli and I. Papautsky, Continuous particle separation in spiral microchannels using dean flows and differential migration, *Lab Chip*, 2008, **8**, 1906.

61 D. R. Gossett and D. Di Carlo, Particle focusing mechanisms in curving confined flows, *Anal. Chem.*, 2009, **81**, 8459–8465.

62 P. A. M. M. Aarts, S. A. T. van den Broek, G. W. Prins, G. D. C. Kuiken, J. J. Sixma and R. M. Heethaar, Blood platelets are concentrated near the wall and red blood cells, in the center in flowing blood., *Arteriosclerosis*, 1988, **8**, 819–824.

63 A. W. Tilles and E. C. Eckstein, The near-wall excess of platelet-sized particles in blood flow: Its dependence on hematocrit and wall shear rate, *Microvasc. Res.*, 1987, **33**, 211–223.

64 R. Fåhræus and T. Lindqvist, The viscosity of the blood in narrow capillary tubes, *Am. J. Physiol. -- Leg. Content*, 1931, **96**, 562 LP-568.

65 A. Kumar and M. D. Graham, Margination and segregation in confined flows of blood and other multicomponent suspensions, *Soft Matter*, 2012, **8**, 10536.

66 H. Zhao, E. S. G. Shaqfeh and V. Narsimhan, Shear-induced particle migration and margination in a cellular suspension, *Phys. Fluids*, 2012, **24**, 11902.

67 G. Segré and A. Silberberg, Behaviour of macroscopic rigid spheres in Poiseuille flow Part 2. Experimental results and interpretation, *J. Fluid Mech.*, 1962, **14**, 136.

68 J.-P. Matas, J. F. Morris and É. Guazzelli, Inertial migration of rigid spherical particles in Poiseuille flow, *J. Fluid Mech.*, 2004, **515**, 171–195.

69 P. Gascoyne, C. Mahidol, M. Ruchirawat, J. Satayavivad, P. Watcharasit and F. F. Becker, Microsample preparation by dielectrophoresis: isolation of malaria, *Lab Chip*, 2002, **2**, 70.

70 S. F. Ibrahim and G. Van Den Engh, High-speed cell sorting: Fundamentals and recent advances, *Curr. Opin. Biotechnol.*, 2003, **14**, 5–12.

71 N. Xia, T. P. Hunt, B. T. Mayers, E. Alsberg, G. M. Whitesides, R. M. Westervelt and D. E. Ingber, Combined microfluidic-micromagnetic separation of living cells in continuous flow, *Biomed. Microdevices*, 2006, **8**, 299–308.

72 T. Akagi and T. Ichiki, Cell electrophoresis on a chip: What can we know from the changes in electrophoretic mobility?, *Anal. Bioanal. Chem.*, 2008, **391**, 2433–2441.

73 S. S. Kuntaegowdanahalli, A. A. S. Bhagat, G. Kumar and I. Papautsky, Inertial microfluidics for continuous particle separation in spiral microchannels, *Lab Chip*, 2009, **9**, 2973.

74 J. Takagi, M. Yamada, M. Yasuda and M. Seki, Continuous particle separation in a microchannel having asymmetrically arranged multiple branches, *Lab Chip*, 2005, **5**, 778.

75 A. A. S. Bhagat, H. W. Hou, L. D. Li, C. T. Lim and J. Han, Pinched flow coupled shear-modulated inertial microfluidics for high-throughput rare blood cell separation, *Lab Chip*, 2011, **11**, 1870.

76 D. Di Carlo, J. F. Edd, D. Irimia, R. G. Tompkins and M. Toner, Equilibrium Separation and Filtration of Particles Using Differential Inertial Focusing, 2008, **80**, 2204–2211.

77 S. C. Hur, N. K. Henderson-MacLennan, E. R. B. McCabe and D. Di Carlo, Deformability-based cell classification and enrichment using inertial microfluidics, *Lab Chip*, 2011, **11**, 912.

78 R. Suwanarusk, B. M. Cooke, A. M. Dondorp, K. Silamut, J. Sattabongkot, N. J. White and R. Udomsangpetch, The deformability of red blood cells parasitized by Plasmodium falciparum and P. vivax., *J. Infect. Dis.*, 2004, **189**, 190–194.

79 F. H. Epstein and H. F. Bunn, Pathogenesis and Treatment of Sickle Cell Disease, *N. Engl. J. Med.*, 1997, **337**, 762–769.

80 S. M. McFaul, B. K. Lin and H. Ma, Cell separation based on size and deformability using microfluidic funnel ratchets, *Lab Chip*, 2012, **12**, 2369.

81 W. Zhang, K. Kai, D. S. Choi, T. Iwamoto, Y. H. Nguyen, H. Wong, M. D. Landis,

N. T. Ueno, J. Chang and L. Qin, Microfluidics separation reveals the stem-cell-like deformability of tumor-initiating cells, *Proc. Natl. Acad. Sci.*, 2012, **109**, 18707–18712.

82 G. Coupier, B. Kaoui, T. Podgorski and C. Misbah, Noninertial lateral migration of vesicles in bounded Poiseuille flow, *Phys. Fluids*, 2008, **20**, 20–23.

83 C. Misbah, Soft suspensions: inertia cooperates with flexibility, *J. Fluid Mech.*, 2014, **760**, 1–4.

84 S. J. Shin and H. J. Sung, Inertial migration of an elastic capsule in a Poiseuille flow, *Phys. Rev. E*, 2011, **83**, 1–13.

85 A. Fery and R. Weinkamer, Mechanical properties of micro- and nanocapsules: Single-capsule measurements, *Polymer*, 2007, **48**, 7221–7235.

86 I. Dulińska, M. Targosz, W. Strojny, M. Lekka, P. Czuba, W. Balwierz and M. Szymoński, Stiffness of normal and pathological erythrocytes studied by means of atomic force microscopy, *J. Biochem. Biophys. Methods*, 2006, **66**, 1–11.

87 E. A. Evans, Bending elastic modulus of red blood cell membrane derived from buckling instability in micropipet aspiration tests, *Biophys. J.*, 1983, **43**, 27–30.

88 D. V. Zhelev, D. Needham and R. M. Hochmuth, A novel micropipet method for measuring the bending modulus of vesicle membranes, *Biophys. J.*, 1994, **67**, 720–727.

89 I. Sraj, C. D. Eggleton, R. Jimenez, E. Hoover, J. Squier, J. Chichester and D. W. M. Marr, Cell deformation cytometry using diode-bar optical stretchers., *J. Biomed. Opt.*, 2013, **15**, 47010.

90 Z. S. Khan and S. A. Vanapalli, Probing the mechanical properties of brain cancer cells using a microfluidic cell squeezer device, *Biomicrofluidics*, 2013, **7**, 11806.

91 H. W. Hou, Q. S. Li, G. Y. H. Lee, A. P. Kumar, C. N. Ong and C. T. Lim, Deformability study of breast cancer cells using microfluidics, *Biomed. Microdevices*, 2009, **11**, 557–564.

92 Q. Guo, S. Park and H. Ma, Microfluidic micropipette aspiration for measuring the deformability of single cells, *Lab Chip*, 2012, **12**, 2687.

93 T. J. Merkel, S. W. Jones, K. P. Herlihy, F. R. Kersey, A. R. Shields, M. Napier, J. C. Luft, H. Wu, W. C. Zamboni, A. Z. Wang, J. E. Bear and J. M. DeSimone, Using mechanobiological mimicry of red blood cells to extend circulation times of hydrogel microparticles, *Proc. Natl. Acad. Sci.*, 2011, **108**, 586–591.

94 X.-Q. Hu, A.-V. Salsac and D. Barthès-Biesel, Flow of a spherical capsule in a pore with circular or square cross-section, *J. Fluid Mech.*, 2012, **705**, 176–194.

95 X. Q. Hu, B. Sévénié, A. V. Salsac, E. Leclerc and D. Barthès-Biesel, Characterizing the membrane properties of capsules flowing in a square-section microfluidic channel: Effects of the membrane constitutive law, *Phys. Rev. E*, 2013, **87**, 1–9.

96 M. E. Cates, Reptation of living polymers: dynamics of entangled polymers in the presence of reversible chain-scission reactions, *Macromolecules*, 1987, **20**, 2289–2296.

97 C. A. Dreiss, in *Wormlike Micelles: Advances in Systems, Characterisation and Applications*, eds. C. A. Dreiss and Y. Feng, Royal Society of Chemistry, 2017, pp. 1–8.

98 S. Lerouge and J.-F. Berret, in *Advances in Polymer Science*, 2009, pp. 1–71.

99 M. E. Cates and S. J. Candau, Statics and dynamics of worm-like surfactant micelles., *J. Phys. Condens. Matter*, 1990, **2**, 6869–6892.

100 S. Förster, M. Konrad and P. Lindner, Shear Thinning and Orientational Ordering of Wormlike Micelles, *Phys. Rev. Lett.*, 2005, **94**, 17803.

101 H. Rehage and H. Hoffmann, Viscoelastic surfactant solutions: model systems for rheological research, *Mol. Phys.*, 1991, **74**, 933–973.

102 E. Cappelaere and R. Cressely, Shear banding structure in viscoelastic micellar solutions, *Colloid Polym. Sci.*, 1997, **275**, 407–418.

103 E. Cappelaere, J. F. Berret, J. P. Decruppe, R. Cressely and P. Lindner, Rheology, birefringence, and small-angle neutron scattering in a charged micellar system: Evidence of a shear-induced phase transition, *Phys. Rev. E*, 1997, **56**, 1869–1878.

104 H. Rehage and H. Hoffmann, Rheological properties of viscoelastic surfactant systems, *J. Phys. Chem.*, 1988, **92**, 4712–4719.

105 F. Lequeux, Reptation of Connected Wormlike Micelles, *Europhys. Lett.*, 1992, **19**, 675–681.

106 C. Oelschlaeger, M. Schopferer, F. Scheffold and N. Willenbacher, Linear-to-Branched Micelles Transition: A Rheometry and Diffusing Wave Spectroscopy (DWS) Study, *Langmuir*, 2009, **25**, 716–723.

107 D. Gaudino, R. Pasquino and N. Grizzuti, Adding salt to a surfactant solution: Linear rheological response of the resulting morphologies, *J. Rheol.*, 2015, **59**, 1363–1375.

108 M. A. Calabrese, S. A. Rogers, R. P. Murphy and N. J. Wagner, The rheology and microstructure of branched micelles under shear, *J. Rheol.*, 2015, **59**, 1299–1328.

109 M. A. Fardin, D. Lopez, J. Croso, G. Grégoire, O. Cardoso, G. H. McKinley and S. Lerouge, Elastic turbulence in shear banding wormlike micelles, *Phys. Rev. Lett.*,

2010, **104**, 1–4.

110 M. A. Fardin, T. Divoux, M. A. Guedeau-Boudeville, I. Buchet-Maulien, J. Browaeys, G. H. McKinley, S. Manneville and S. Lerouge, Shear-banding in surfactant wormlike micelles: elastic instabilities and wall slip, *Soft Matter*, 2012, **8**, 2535.

111 H. Mohammadigoushki and S. J. Muller, A flow visualization and superposition rheology study of shear-banding wormlike micelle solutions, *Soft Matter*, 2016, **12**, 1051–1061.

112 M. R. Stukan, E. S. Boek, J. T. Padding, W. J. Briels and J. P. Crawshaw, Flow of wormlike micelles in an expansion-contraction geometry, *Soft Matter*, 2008, **4**, 870.

113 S. J. Haward and G. H. McKinley, Stagnation point flow of wormlike micellar solutions in a microfluidic cross-slot device: Effects of surfactant concentration and ionic environment, *Phys. Rev. E*, 2012, **85**, 1–14.

114 N. Dubash, P. Cheung and A. Q. Shen, Elastic instabilities in a microfluidic cross-slot flow of wormlike micellar solutions, *Soft Matter*, 2012, **8**, 5847.

115 J. A. Pathak and S. D. Hudson, Rheo-optics of equilibrium polymer solutions: Wormlike micelles in elongational flow in a microfluidic cross-slot, *Macromolecules*, 2006, **39**, 8782–8792.

116 M. A. Fardin, B. Lasne, O. Cardoso, G. Gr?goire, M. Argentina, J. P. Decruppe and S. Lerouge, Taylor-like Vortices in Shear-Banding Flow of Giant Micelles, *Phys. Rev. Lett.*, 2009, **103**, 28302.

117 M. A. Fardin, T. J. Ober, V. Grenard, T. Divoux, S. Manneville, G. H. McKinley and S. Lerouge, Interplay between elastic instabilities and shear-banding: three categories of Taylor–Couette flows and beyond, *Soft Matter*, 2012, **8**, 10072.

118 S. Lerouge, M. Argentina and J. P. Decruppe, Interface instability in shear-banding flow, *Phys. Rev. Lett.*, 2006, **96**, 1–4.

119 S. Lerouge, J. P. Decruppe and P. Olmsted, Birefringence banding in a micellar solution or the complexity of heterogeneous flows, *Langmuir*, 2004, **20**, 11355–11365.

120 M. R. Stukan, E. S. Boek, J. T. Padding and J. P. Crawshaw, Influence of system size and solvent flow on the distribution of wormlike micelles in a contraction-expansion geometry, *Eur. Phys. J. E*, 2008, **26**, 63–71.

121 T. J. Ober, S. J. Haward, C. J. Pipe, J. Soulages and G. H. McKinley, Microfluidic extensional rheometry using a hyperbolic contraction geometry, *Rheol. Acta*, 2013, **52**, 529–546.

122 S. Kuriakose and P. Dimitrakopoulos, Deformation of an elastic capsule in a rectangular microfluidic channel, *Soft Matter*, 2013, **9**, 4284.

123 G. Coupier, A. Farutin, C. Minetti, T. Podgorski and C. Misbah, Shape diagram of vesicles in poiseuille flow, *Phys. Rev. Lett.*, 2012, **108**, 1–5.

124 M. Guo and H. M. Wyss, Micromechanics of soft particles, *Macromol. Mater. Eng.*, 2011, **296**, 223–229.

125 M. Stolz, R. Raiteri, A. U. Daniels, M. R. VanLandingham, W. Baschong and U. Aebi, Dynamic elastic modulus of porcine articular cartilage determined at two different levels of tissue organization by indentation-type atomic force microscopy., *Biophys. J.*, 2004, **86**, 3269–83.

126 C. T. Buckley, S. D. Thorpe, F. J. O'Brien, A. J. Robinson and D. J. Kelly, The effect of concentration, thermal history and cell seeding density on the initial mechanical properties of agarose hydrogels, *J. Mech. Behav. Biomed. Mater.*, 2009, **2**, 512–521.

127 A. Adler, E. A. Cowley, J. H. Bates and D. H. Eidelman, Airway-parenchymal interdependence after airway contraction in rat lung explants., *J. Appl. Physiol.*, 1998, **85**, 231–7.

128 Q. Chen, S. I. Ringleb, T. Hulshizer and K. N. An, Identification of the testing parameters in high frequency dynamic shear measurement on agarose gels, *J. Biomech.*, 2005, **38**, 959–963.

129 S. Inoué and K. Spring, *Video Microscopy: The Fundamentals*, Springer US, New York: Plenum, 2nd edn., 1997.

130 N. Otsu, A threshold selection method from gray-level histograms, *IEEE Trans. Syst. Man. Cybern.*, 1979, **9**, 62–66.

131 K. M. C. Chan, R. H. Li, J. W. Chapman, E. M. Trac, J. B. Kobler, S. M. Zeitels, R. Langer and S. S. Karajanagi, Functionalizable hydrogel microparticles of tunable size and stiffness for soft-tissue filler applications, *Acta Biomater.*, 2014, **10**, 2563–2573.

132 E. Kumacheva and P. Garstecki, *Microfluidic Reactors for Polymer Particles*, John Wiley and Sons, 2011.

133 M. Malmsten, Soft drug delivery systems, *Soft Matter*, 2006, **2**, 760.

134 S. Seiffert, Small but smart: sensitive microgel capsules., *Angew. Chemie Int. Ed.*, 2013, **52**, 11462–8.

135 D. Barthès-Biesel, Motion and Deformation of Elastic Capsules and Vesicles in Flow, *Annu. Rev. Fluid Mech.*, 2016, **48**, 25–52.

136 A. R. Abate, A. Poitzsch, Y. Hwang, J. Lee, J. Czerwinska and D. A. Weitz, Impact of inlet channel geometry on microfluidic drop formation, *Phys. Rev. E*, 2009, **80**, 26310.

137 L.-Y. Chu, A. S. Utada, R. K. Shah, J.-W. Kim and D. A. Weitz, Controllable Monodisperse Multiple Emulsions, *Angew. Chemie Int. Ed.*, 2007, **46**, 8970–8974.

138 W. J. Duncanson, T. Lin, A. R. Abate, S. Seiffert, R. K. Shah and D. A. Weitz, Microfluidic synthesis of advanced microparticles for encapsulation and controlled release, *Lab Chip*, 2012, **12**, 2135.

139 K. Y. Lee and D. J. Mooney, Alginate: Properties and biomedical applications, *Prog. Polym. Sci.*, 2012, **37**, 106–126.

140 H. H. Tønnesen and J. Karlsen, Alginate in drug delivery systems., *Drug Dev. Ind. Pharm.*, 2002, **28**, 621–30.

141 G. T. Grant, E. R. Morris, D. A. Rees, P. J. C. Smith and D. Thom, Biological interactions between polysaccharides and divalent cations: The egg-box model, *FEBS Lett.*, 1973, **32**, 195–198.

142 J. L. Drury, R. G. Dennis and D. J. Mooney, The tensile properties of alginate hydrogels, *Biomaterials*, 2004, **25**, 3187–3199.

143 C. D. Markert, X. Guo, A. Skardal, Z. Wang, S. Bharadwaj, Y. Zhang, K. Bonin and M. Guthold, Characterizing the micro-scale elastic modulus of hydrogels for use in regenerative medicine, *J. Mech. Behav. Biomed. Mater.*, 2013, **27**, 115–127.

144 S. Fu, A. Thacker, D. M. Sperger, R. L. Boni, I. S. Buckner, S. Velankar, E. J. Munson and L. H. Block, Relevance of rheological properties of sodium alginate in solution to calcium alginate gel properties., *AAPS PharmSciTech*, 2011, **12**, 453–60.

145 A. Martinsen, G. Skjåk-Braek and O. Smidsrød, Alginate as immobilization material: I. Correlation between chemical and physical properties of alginate gel beads., *Biotechnol. Bioeng.*, 1989, **33**, 79–89.

146 M. A. LeRoux, F. Guilak and L. A. Setton, Compressive and shear properties of alginate gel: Effects of sodium ions and alginate concentration, *J. Biomed. Mater. Res.*, 1999, **47**, 46–53.

147 H.-J. Kong, K. Y. Lee and D. J. Mooney, Decoupling the dependence of rheological/mechanical properties of hydrogels from solids concentration, *Polymer*, 2002, **43**, 6239–6246.

148 E. R. West, M. Xu, T. K. Woodruff and L. D. Shea, Physical properties of alginate hydrogels and their effects on in vitro follicle development, *Biomaterials*, 2007, **28**, 4439–4448.

149 K. Y. Lee, J. A. Rowley, P. Eiselt, E. M. Moy, K. H. Bouhadir and D. J. Mooney, Controlling Mechanical and Swelling Properties of Alginate Hydrogels Independently by Cross-Linker Type and Cross-Linking Density, *Macromolecules*, 2000, **33**, 4291–4294.

150 E. Amici, G. Tetradis-Meris, C. P. de Torres and F. Jousse, Alginate gelation in microfluidic channels, *Food Hydrocoll.*, 2008, **22**, 97–104.

151 G. Fundueanu, C. Nastruzzi, A. Carpov, J. Desbrieres and M. Rinaudo, Physico-chemical characterization of Ca-alginate microparticles produced with different methods, *Biomaterials*, 1999, **20**, 1427–1435.

152 C.-H. Yeh, Q. Zhao, S.-J. Lee and Y.-C. Lin, Using a T-junction microfluidic chip for monodisperse calcium alginate microparticles and encapsulation of nanoparticles, *Sensors Actuators A Phys.*, 2009, **151**, 231–236.

153 J.-W. Kim, A. S. Utada, A. Fernández-Nieves, Z. Hu and D. A. Weitz, Fabrication of Monodisperse Gel Shells and Functional Microgels in Microfluidic Devices, *Angew. Chemie Int. Ed.*, 2007, **46**, 1819–1822.

154 T. Kong, L. Wang, H. M. Wyss and H. C. Shum, Capillary micromechanics for core-shell particles., *Soft Matter*, 2014, **10**, 3271–6.

155 R. Pelton, Temperature-sensitive aqueous microgels, *Adv. Colloid Interface Sci.*, 2000, **85**, 1–33.

156 Y. Guan and Y. Zhang, PNIPAM microgels for biomedical applications: from dispersed particles to 3D assemblies, *Soft Matter*, 2011, **7**, 6375.

157 D. Lim, E. Lee, H. Kim, S. Park, S. Baek and J. Yoon, Multi stimuli-responsive hydrogel microfibers containing magnetite nanoparticles prepared using microcapillary devices, *Soft Matter*, 2015, **11**, 1606–1613.

158 D. Kim, E. Lee, H. S. Lee and J. Yoon, Energy Efficient Glazing for Adaptive Solar Control Fabricated with Photothermotropic Hydrogels Containing Graphene Oxide, *Sci. Rep.*, 2015, **5**, 7646.

159 A. Wang, C. Tao, Y. Cui, L. Duan, Y. Yang and J. Li, Assembly of environmental sensitive microcapsules of PNIPAAm and alginate acid and their application in drug release, *J. Colloid Interface Sci.*, 2009, **332**, 271–279.

160 R. H. Pelton and P. Chibante, Preparation of aqueous latices with N-isopropylacrylamide, *Colloids and Surfaces*, 1986, **20**, 247–256.

161 L. Y. Chu, J. W. Kim, R. K. Shah and D. A. Weitz, Monodisperse thermoresponsive microgels with tunable volume-phase transition kinetics, *Adv. Funct. Mater.*, 2007, **17**, 3499–3504.

162 A. Burmistrova, M. Richter, C. Uzum and R. V. Klitzing, Effect of cross-linker density of P(NIPAM-co-AAc) microgels at solid surfaces on the swelling/shrinking behaviour and the Young's modulus, *Colloid Polym. Sci.*, 2011, **289**, 613–624.

163 H. A. Awad, M. Q. Wickham, H. A. Leddy, J. M. Gimble and F. Guilak, Chondrogenic differentiation of adipose-derived adult stem cells in agarose, alginate, and gelatin scaffolds, *Biomaterials*, 2004, **25**, 3211–3222.

164 A. J. Engler, S. Sen, H. L. Sweeney and D. E. Discher, Matrix Elasticity Directs Stem Cell Lineage Specification, *Cell*, 2006, **126**, 677–689.

165 A. J. Keung, E. M. De Juan-Pardo, D. V. Schaffer and S. Kumar, Rho GTPases mediate the mechanosensitive lineage commitment of neural stem cells, *Stem Cells*, 2011, **29**, 1886–1897.

166 J. F. Morris, A review of microstructure in concentrated suspensions and its implications for rheology and bulk flow, *Rheol. Acta*, 2009, **48**, 909–923.

167 D. Lee, S. N. Beesabathuni and A. Q. Shen, Shape-tunable wax microparticle synthesis via microfluidics and droplet impact, *Biomicrofluidics*, 2015, **9**, 1–14.

168 D. Dendukuri, D. C. Pregibon, J. Collins, T. A. Hatton and P. S. Doyle, Continuous-flow lithography for high-throughput microparticle synthesis., *Nat. Mater.*, 2006, **5**, 365–369.

169 D. Dendukuri, S. S. Gu, D. C. Pregibon, T. A. Hatton and P. S. Doyle, Stop-flow lithography in a microfluidic device., *Lab Chip*, 2007, **7**, 818–828.

170 L. Liu, F. Wu, X.-J. Ju, R. Xie, W. Wang, C. H. Niu and L.-Y. Chu, Preparation of monodisperse calcium alginate microcapsules via internal gelation in microfluidic-generated double emulsions., *J. Colloid Interface Sci.*, 2013, **404**, 85–90.

171 K. S. Paulsen, D. Di Carlo and A. J. Chung, Optofluidic fabrication for 3D-shaped particles., *Nat. Commun.*, 2015, **6**, 6976.

172 C. Y. Wu, K. Owsley and D. Di Carlo, Rapid Software-Based Design and Optical Transient Liquid Molding of Microparticles, *Adv. Mater.*, 2015, **27**, 7970–7978.

173 E. A. Nunamaker, K. J. Otto and D. R. Kipke, Investigation of the material properties of alginate for the development of hydrogel repair of dura mater, *J. Mech. Behav. Biomed. Mater.*, 2011, **4**, 16–33.

174 S. K. Bajpai and S. Sharma, Investigation of swelling/degradation behaviour of alginate beads crosslinked with Ca2+ and Ba2+ ions, *React. Funct. Polym.*, 2004, **59**, 129–140.

175 S. H. Hong, M. Shin, J. Lee, J. H. Ryu, S. Lee, J. W. Yang, W. D. Kim and H. Lee, STAPLE: Stable Alginate Gel Prepared by Linkage Exchange from Ionic to

Covalent Bonds, *Adv. Healthc. Mater.*, 2016, **5**, 75–79.

176 G. Pasparakis and N. Bouropoulos, Swelling studies and in vitro release of verapamil from calcium alginate and calcium alginate-chitosan beads, *Int. J. Pharm.*, 2006, **323**, 34–42.

177 H. Ma and M. D. Graham, Theory of shear-induced migration in dilute polymer solutions near solid boundaries, *Phys. Fluids*, 2005, **17**, 83103.

178 S. J. Shin and H. J. Sung, Dynamics of an elastic capsule in moderate Reynolds number Poiseuille flow, *Int. J. Heat Fluid Flow*, 2012, **36**, 167–177.

179 W. E. Uspal, H. Burak Eral and P. S. Doyle, Engineering particle trajectories in microfluidic flows using particle shape, *Nat. Commun.*, 2013, **4**, 2666.

180 F. Gentile, C. Chiappini, D. Fine, R. C. Bhavane, M. S. Peluccio, M. M.-C. Cheng, X. Liu, M. Ferrari and P. Decuzzi, The effect of shape on the margination dynamics of non-neutrally buoyant particles in two-dimensional shear flows., *J. Biomech.*, 2008, **41**, 2312–8.

181 L. Shi, T. W. Pan and R. Glowinski, Lateral migration and equilibrium shape and position of a single red blood cell in bounded Poiseuille flows, *Phys. Rev. E*, 2012, **86**, 1–12.

182 H. L. Goldsmith and S. G. Mason, The flow of suspensions through tubes. I. Single spheres, rods, and discs, *J. Colloid Sci.*, 1962, **17**, 448–476.

183 P. C.-H. Chan and L. G. Leal, The motion of a deformable drop in a second-order fluid, *J. Fluid Mech.*, 1979, **92**, 131.

184 D. Abreu, M. Levant, V. Steinberg and U. Seifert, Fluid vesicles in flow, *Adv. Colloid Interface Sci.*, 2014, **208**, 129–141.

185 D. Barthès-Biesel, Motion and Deformation of Elastic Capsules and Vesicles in Flow, *Annu. Rev. Fluid Mech.*, 2016, **48**, 25–52.

186 T. Gao and H. H. Hu, Deformation of elastic particles in viscous shear flow, *J. Comput. Phys.*, 2009, **228**, 2132–2151.

187 C.-H. Wang and A. S. Popel, Effect of red blood cell shape on oxygen transport in capillaries., *Math. Biosci.*, 1993, **116**, 89–110.

188 V. P. Zharov, E. I. Galanzha, Y. Menyaev and V. V. Tuchin, In vivo high-speed imaging of individual cells in fast blood flow, *J. Biomed. Opt.*, 2006, **11**, 54034.

189 G. Tomaiuolo, M. Simeone, V. Martinelli, B. Rotoli and S. Guido, Red blood cell deformation in microconfined flow, *Soft Matter*, 2009, **5**, 3736.

190 H. Noguchi and G. Gompper, Shape transitions of fluid vesicles and red blood cells in capillary flows, *Proc. Natl. Acad. Sci.*, 2005, **102**, 14159–14164.

191 B. G. De Geest, C. Déjugnat, G. B. Sukhorukov, K. Braeckmans, S. C. De Smedt and J. Demeester, Self-rupturing microcapsules, *Adv. Mater.*, 2005, **17**, 2357–2361.

192 J. Siepmann and F. Siepmann, Modeling of diffusion controlled drug delivery, *J. Control. Release*, 2012, **161**, 351–362.

193 M.-A. Mader, V. Vitkova, M. Abkarian, A. Viallat and T. Podgorski, Dynamics of viscous vesicles in shear flow, *Eur. Phys. J. E*, 2006, **19**, 389–397.

194 M. Abkarian and A. Viallat, Vesicles and red blood cells in shear flow, *Soft Matter*, 2008, **4**, 653.

195 J. Deschamps, V. Kantsler and V. Steinberg, Phase diagram of single vesicle dynamical states in shear Flow, *Phys. Rev. Lett.*, 2009, **102**, 3–6.

196 V. Kantsler and V. Steinberg, Orientation and Dynamics of a Vesicle in Tank-Treading Motion in Shear Flow, *Phys. Rev. Lett.*, 2005, **95**, 258101.

197 V. Kantsler and V. Steinberg, Transition to Tumbling and Two Regimes of Tumbling Motion of a Vesicle in Shear Flow, *Phys. Rev. Lett.*, 2006, **96**, 36001.

198 H. Noguchi and G. Gompper, Dynamics of fluid vesicles in shear flow: Effect of membrane viscosity and thermal fluctuations, *Phys. Rev. E*, 2005, **72**, 11901.

199 H. Noguchi and G. Gompper, Swinging and Tumbling of Fluid Vesicles in Shear Flow, *Phys. Rev. Lett.*, 2007, **98**, 128103.

200 S. R. Keller and R. Skalak, Motion of a tank-treading ellipsoidal particle in a shear flow, *J. Fluid Mech.*, 1982, **120**, 27.

201 C. Misbah, Vacillating Breathing and Tumbling of Vesicles under Shear Flow, *Phys. Rev. Lett.*, 2006, **96**, 28104.

202 J. Deschamps, V. Kantsler, E. Segre and V. Steinberg, Dynamics of a vesicle in general flow, *Proc. Natl. Acad. Sci.*, 2009, **106**, 11444–11447.

203 D. Barthès-Biesel, Motion of a spherical microcapsule freely suspended in a linear shear flow, *J. Fluid Mech.*, 1980, **100**, 831.

204 D. Barthes-Biesel, Theoretical modelling of the motion and deformation of capsules in shear flows., *Biomater. Artif. Cells Immobilization Biotechnol.*, 1993, **21**, 359–373.

205 C. Pozrikidis, Finite deformation of liquid capsules enclosed by elastic membranes in simple shear flow, *J. Fluid Mech.*, 1995, **297**, 123.

206 S. Ramanujan and C. Pozrikidis, Deformation of liquid capsules enclosed by elastic membranes in simple shear flow: large deformations and the effect of fluid viscosities, *J. Fluid Mech.*, 1998, **361**, 117–143.

207 E. Lac, D. Barthès-Biesel, N. A. Pelekasis and J. Tsamopoulos, Spherical capsules in three-dimensional unbounded Stokes flows: effect of the membrane constitutive law and onset of buckling, *J. Fluid Mech.*, 2004, **516**, 303–334.

208 S. Kessler, R. Finken and U. Seifert, Swinging and tumbling of elastic capsules in shear flow, *J. Fluid Mech.*, 2008, **605**, 207–226.

209 Y. Sui, H. T. Low, Y. T. Chew and P. Roy, Tank-treading, swinging, and tumbling of liquid-filled elastic capsules in shear flow, *Phys. Rev. E*, 2008, **77**, 207–226.

210 D. R. Subramaniam and D. J. Gee, Shape oscillations of elastic particles in shear flow, *J. Mech. Behav. Biomed. Mater.*, 2016, **62**, 534–544.

211 P. Bagchi and R. M. Kalluri, Dynamics of nonspherical capsules in shear flow, *Phys. Rev. E*, 2009, **80**, 1–12.

212 K. S. Chang and W. L. Olbricht, Experimental studies of the deformation and breakup of a synthetic capsule in steady and unsteady simple shear flow, *J. Fluid Mech.*, 1993, **250**, 609.

213 A. Walter, H. Rehage and H. Leonhard, Shear-induced deformations of polyamide microcapsules, *Colloid Polym. Sci.*, 2000, **278**, 169–175.

214 A. Walter, H. Rehage and H. Leonhard, Shear induced deformation of microcapsules: shape oscillations and membrane folding, *Colloids Surfaces A Physicochem. Eng. Asp.*, 2001, **183**, 123–132.

215 I. Koleva and H. Rehage, Deformation and orientation dynamics of polysiloxane microcapsules in linear shear flow, *Soft Matter*, 2012, **8**, 3681.

216 D. Barthes-Biesel and H. Sgaier, Role of membrane viscosity in the orientation and deformation of a spherical capsule suspended in shear flow, *J. Fluid Mech.*, 1985, **160**, 119.

217 S. Sukumaran and U. Seifert, Influence of shear flow on vesicles near a wall: A numerical study, *Phys. Rev. E*, 2001, **64**, 1–11.

218 M. Abkarian, C. Lartigue and A. Viallat, Tank Treading and Unbinding of Deformable Vesicles in Shear Flow: Determination of the Lift Force, *Phys. Rev. Lett.*, 2002, **88**, 68103.

219 M. Abkarian and A. Viallat, Dynamics of Vesicles in a Wall-Bounded Shear Flow, *Biophys. J.*, 2005, **89**, 1055–1066.

220 N. Callens, C. Minetti, G. Coupier, M.-A. Mader, F. Dubois, C. Misbah and T. Podgorski, Hydrodynamic lift of vesicles under shear flow in microgravity, *EPL (Europhysics Lett.*, 2008, **83**, 24002.

221 R. K. Singh, X. Li and K. Sarkar, Lateral migration of a capsule in plane shear near a wall, *J. Fluid Mech.*, 2014, **739**, 421–443.

222 S. K. Doddi and P. Bagchi, Lateral migration of a capsule in a plane Poiseuille flow in a channel, *Int. J. Multiph. Flow*, 2008, **34**, 966–986.

223 B. Kaoui, G. H. Ristow, I. Cantat, C. Misbah and W. Zimmermann, Lateral migration of a two-dimensional vesicle in unbounded Poiseuille flow, *Phys. Rev. E*, 2008, **77**, 1–9.

224 H. Li and G. Ma, Modeling performance of a two-dimensional capsule in a microchannel flow: Long-term lateral migration, *Phys. Rev. E*, 2010, **82**, 1–14.

225 M. M. Villone, F. Greco, M. A. Hulsen and P. L. Maffettone, Numerical simulations of deformable particle lateral migration in tube flow of Newtonian and viscoelastic media, *J. Nonnewton. Fluid Mech.*, 2016, **234**, 105–113.

226 F. Risso, F. Collé-Paillot and M. Zagzoule, Experimental investigation of a bioartificial capsule flowing in a narrow tube, *J. Fluid Mech.*, 2006, **547**, 149.

227 S. Kuriakose and P. Dimitrakopoulos, Motion of an elastic capsule in a square microfluidic channel, *Phys. Rev. E*, 2011, **84**, 1–22.

228 R. Bruinsma, Rheology and shape transitions of vesicles under capillary flow, *Phys. A Stat. Mech. its Appl.*, 1996, **234**, 249–270.

229 V. Vitkova, M. Mader and T. Podgorski, Deformation of vesicles flowing through capillaries, *Europhys. Lett.*, 2004, **68**, 398–404.

230 J. L. McWhirter, H. Noguchi and G. Gompper, Flow-induced clustering and alignment of vesicles and red blood cells in microcapillaries, *Proc. Natl. Acad. Sci.*, 2009, **106**, 6039–6043.

231 J. L. McWhirter, H. Noguchi and G. Gompper, Deformation and clustering of red blood cells in microcapillary flows, *Soft Matter*, 2011, **7**, 10967.

232 Y. Lefebvre, E. Leclerc, D. Barthès-Biesel, J. Walter and F. Edwards-Lévy, Flow of artificial microcapsules in microfluidic channels: A method for determining the elastic properties of the membrane, *Phys. Fluids*, 2008, **20**, 123102.

233 P. Dimitrakopoulos and S. Kuriakose, Determining a membrane's shear modulus, independent of its area-dilatation modulus, via capsule flow in a converging micro-capillary, *Soft Matter*, 2015, **11**, 2782–2793.

234 K. S. Chang and W. L. Olbricht, Experimental studies of the deformation and breakup of a synthetic capsule in steady and unsteady simple shear flow, *J. Fluid Mech.*, 1993, **250**, 609.

235 M. Y. Hwang, S. G. Kim, H. S. Lee and S. J. Muller, Generation and characterization of monodisperse deformable alginate and pNIPAM microparticles with a wide range of shear moduli, *Soft Matter*, 2017, DOI: 10.1039/C7SM01079F.

236 L. E. Rodd, J. J. Cooper-White, D. V. Boger and G. H. McKinley, Role of the elasticity number in the entry flow of dilute polymer solutions in micro-fabricated contraction geometries, *J. Nonnewton. Fluid Mech.*, 2007, **143**, 170–191.

237 M. A. Alves, P. J. Oliveira and F. T. Pinho, On the effect of contraction ratio in viscoelastic flow through abrupt contractions, *J. Nonnewton. Fluid Mech.*, 2004, **122**, 117–130.

238 S. Gulati, S. J. Muller and D. Liepmann, Direct measurements of viscoelastic flows of DNA in a 2:1 abrupt planar micro-contraction, *J. Nonnewton. Fluid Mech.*, 2008, **155**, 51–66.

239 S. J. Haward, Z. Li, D. Lighter, B. Thomas, J. A. Odell and X. F. Yuan, Flow of dilute to semi-dilute polystyrene solutions through a benchmark 8:1 planar abrupt micro-contraction, *J. Nonnewton. Fluid Mech.*, 2010, **165**, 1654–1669.

240 E. S. Shaqfeh, Fully Elastic Instabilities in Viscometric Flows, *Annu. Rev. Fluid Mech.*, 1996, **28**, 129–185.

241 G. H. McKinley, P. Pakdel and A. Öztekin, Rheological and geometric scaling of purely elastic flow instabilities, *J. Nonnewton. Fluid Mech.*, 1996, **67**, 19–47.

242 P. Pakdel and G. H. McKinley, Elastic instability and cruved streamlines, *Phys. Rev. Lett.*, 1996, **77**, 2459–2462.

243 A. Lanzaro and X. F. Yuan, Effects of contraction ratio on non-linear dynamics of semi-dilute, highly polydisperse PAAm solutions in microfluidics, *J. Nonnewton. Fluid Mech.*, 2011, **166**, 1064–1075.

244 Z. Li, X. F. Yuan, S. J. Haward, J. A. Odell and S. Yeates, Non-linear dynamics of semi-dilute polydisperse polymer solutions in microfluidics: Effects of flow geometry, *Rheol. Acta*, 2011, **50**, 277–290.

245 F. A. Cruz, R. J. Poole, A. M. Afonso, F. T. Pinho, P. J. Oliveira and M. A. Alves, Influence of channel aspect ratio on the onset of purely-elastic flow instabilities in three-dimensional planar cross-slots, *J. Nonnewton. Fluid Mech.*, 2016, **227**, 65–79.

246 S. J. Haward, G. H. McKinley and A. Q. Shen, Elastic instabilities in planar elongational flow of monodisperse polymer solutions, *Sci. Rep.*, 2016, **6**, 33029.

247 R. G. Larson, S. J. Muller and E. S. G. Shaqfeh, The effect of fluid rheology on the elastic Taylor-Couette instability, *J. Nonnewton. Fluid Mech.*, 1994, **51**, 195–225.

248 R. G. Larson, Instabilities in viscoelastic flows, *Rheol. Acta*, 1992, **31**, 213–263.

249 S. J. Muller, Elastically-influenced instabilities in Taylor-Couette and other flows with curved streamlines: A review, *Korea Aust. Rheol. J.*, 2008, **20**, 117–125.

250 B. M. Baumert and S. J. Muller, Flow regimes in model viscoelastic fluids in a circular couette system with independently rotating cylinders, *Phys. Fluids*, 1997, **9(3)**, 566–586.

251 S. Chono and Y. Iemoto, Generation of reverse flow of viscoelastic fluid upstream of re-entrant corner in two-dimensional l-shaped channel, *Japan Soc. Mech. Eng.*, 1986, **53**, 2733–2738.

252 S. Chono, Numerical simulation of viscoelastic flow in two-dimensional L-shaped channels, *J. Rheol.*, 1992, **36**, 335.

253 J. A. Pathak, D. Ross and K. B. Migler, Elastic flow instability, curved streamlines, and mixing in microfluidic flows, *Phys. Fluids*, 2004, **16**, 4028–4034.

254 M. S. N. Oliveira, L. E. Rodd, G. H. McKinley and M. A. Alves, Simulations of extensional flow in microrheometric devices, *Microfluid. Nanofluidics*, 2008, **5**, 809–826.

255 S. C. Omowunmi and X. F. Yuan, Modelling the three-dimensional flow of a semi-dilute polymer solution in microfluidics-on the effect of aspect ratio, *Rheol. Acta*, 2010, **49**, 585–595.

256 R. J. Poole, M. Alfateh and A. P. Gauntlett, Bifurcation in a T-channel junction: Effects of aspect ratio and shear-thinning, *Chem. Eng. Sci.*, 2013, **104**, 839–848.

257 Z. Chu, C. A. Dreiss and Y. Feng, Smart wormlike micelles, *Chem. Soc. Rev.*, 2013, **42**, 7174.

258 L. M. Walker, Rheology and structure of worm-like micelles, *Curr. Opin. Colloid Interface Sci.*, 2001, **6**, 451–456.

259 H. Mohammadigoushki and S. J. Muller, Sedimentation of a sphere in wormlike micellar fluids, *J. Rheol.*, 2016, **60**, 587–601.

260 J. P. Rothstein, Transient extensional rheology of wormlike micelle solutions, *J. Rheol.*, 2003, **47**, 1227–1247.

261 S. J. Haward, T. J. Ober, M. S. N. Oliveira, M. A. Alves and G. H. McKinley, Extensional rheology and elastic instabilities of a wormlike micellar solution in a microfluidic cross-slot device, *Soft Matter*, 2012, **8**, 536–555.

262 H. R. Tamaddon Jahromi, M. F. Webster, J. P. Aguayo and O. Manero, Numerical investigation of transient contraction flows for worm-like micellar systems using Bautista-Manero models, *J. Nonnewton. Fluid Mech.*, 2011, **166**, 102–117.

263 F. C. Li, H. Kinoshita, X. Bin Li, M. Oishi, T. Fujii and M. Oshima, Creation of very-low-Reynolds-number chaotic fluid motions in microchannels using viscoelastic surfactant solution, *Exp. Therm. Fluid Sci.*, 2010, **34**, 20–27.

264 Y. Zhao, P. Cheung and A. Q. Shen, Microfluidic flows of wormlike micellar solutions, *Adv. Colloid Interface Sci.*, 2014, **211**, 34–46.

265 S. A. Rogers, M. A. Calabrese and N. J. Wagner, Rheology of branched wormlike micelles, *Curr. Opin. Colloid Interface Sci.*, 2014, **19**, 530–535.

266 R. Angelico, S. Amin, M. Monduzzi, S. Murgia, U. Olsson and G. Palazzo, Impact of branching on the viscoelasticity of wormlike reverse micelles, *Soft Matter*, 2012, **8**, 10941.

Appendix A PDMS Master and Device Fabrication

This chapter details the process to making the masters used for standard soft lithography methods that make polydimethylsiloxane (PDMS) devices. Then a basic protocol for PDMS device fabrication is described.

Channel masks were designed in AutoCAD—Autodesk provides free student versions of its software. It is best to start with the wafer size/boundary. Both SU-8 and Riston Goldmaster laminate are negative photoresists, meaning that the desired channels should be exposed to UV and require "Dark Field Right Read Down" image and polarity and orientation. The Mylar masks used were ordered from Fineline Imaging. Before submitting, check each design to ensure that there are no gaps. The easiest way for this is to use the region function, select each set of objects to make them regions, then use the "union" function to join the regions.

A.1 SU-8 Master Fabrication

SU-8 is the standard negative photoresist for making masters. It requires a lengthy process of spin coating the SU-8 onto silicon wafers, baking, exposing, and developing the master. Because the height of the master is dependent on the spin coating, longer channels spanning the entire wafer sometimes are uneven in height across the device. However, the resulting masters make clean channels with good resolution and a wide and continuous range of possible heights. Depending on the desired channel height, there are a range of SU-8 photoresists, each with different viscosities. Use the technical references available from MicroChem to determine the optimal one based on the thickness versus spin speed calibration curves. For example, SU-8 2050 can be used for heights from 40 to 170 μm.

Step by step SU-8 protocol:

1) Turn on UV aligner
2) Set hot plates at 65°C, 95°C, and 150°C
3) Clean the silicon wafers by rinsing with: acetone, IPA, DI water, air drying between each rinse. Dry for 15-30 minutes on the 150°C hot plate
4) Spin coat the SU-8 as soon as possible after dehydration bake.
    a. Replace foil in the spin coater.
    b. Make sure wafer is centered on vacuum chuck in the spin coater (there is a program on the spin coater where you can observe the wafer for any imbalances).
    c. Program and spin coat the wafer. Spin speed depends on targeted height. Basic program:

Spin speed:	500 rpm	time:	10 s	acceleration:	100 rpm/s
Spin speed: (set by height)		time:	30 s	acceleration:	300 rpm/s

5) Remove edge bead with acetone using a cotton swab or folded techwipe

6) Soft bake the wafer on a hot plate, covering with foil, leaving a gap between the foil and the wafer. The time at each temperature (and on each corresponding hot plate) depends on the height and is specified on the MicroChem data sheet
7) Load blank mask (clear mylar sheet) in UV aligner, measure UV power
8) Calculate exposure time needed based on exposure energy appropriate for the height using:

    Time = [(Energy / Power) * 1.5] ^ 2

9) Load mask in UV aligner. Align wafer and visually ensure hard contact (slight change in color of features) between wafer and mask. Expose.
10) Post exposure bake on 65°C and 95°C hot plates for appropriate times.
11) Remove mask from aligner
12) Develop wafer in a dish of SU-8 developer on the shaker.
13) Rinse with developer for 10 seconds.
14) Rinse with IPA for 10 seconds. If the wafer is not fully developed yet, a white film will form. If this is the case, continue developing until the film no longer forms.
15) Dry with air.
16) Hard bake for 30 minutes (or at least 5-10 minutes) on the 150°C hot plate. Turn off hot plate and cool on hot plate for 30 minutes before removing.
17) Silanize the wafer with silane (Trichloro(1H,1H,2H,2H-perfluorooctyl)silane)
    a. If wafer has cooled completely after the hard bake, bake at 150°C for 5 minutes.
    b. Place wafer in desiccator.
    c. Add 1 drop silane in the small vials on either side of the wafer, ensuring that the vials remain upright. They can be inserted into pieces of foam or held up by beakers.
    d. Vacuum for 2 hours.
    e. Bake at 65°C for 10 minutes.

A.2 Laminate Master Fabrication

Dupont Riston Goldmaster GM130 is a negative photoresist film, so the same mask can be used for both the dry film and SU-8. The film is laminated onto a steel wafer with an Akiles ProLam Ultra laminator, exposed with a UV aligner, and finally developed with aqueous 1 wt% K_2CO_3. Because Riston is a film, the height and resolution of the master is limited to the film thickness, (50, 75, or 100 μm) or combinations of the films. The fabrication process is much faster than SU-8 and has fairly uniform channel heights .However, the developing process is not as robust as SU-8, with finer features occasionally washing away.

Step-by-step laminate protocol

1) Turn on laminator and set to desired temperature (usually T=120°C). Turn on the hot plate to 150°C
2) Clean steel wafer
    a. Remove sticker protecting mirrored side of the wafer

   b. Clean with acetone. Adhesive tends to stick to edge of wafer, so rub edge with techwipe and acetone until adhesive is removed. Rinse with more acetone and dry with air gun.
   c. Rinse with IPA and water. Dry with air gun between each rinse.
3) Dehydrate the steel wafer on the hot plate for 20 minutes. Immediately remove and cool completely.
4) Cut out laminate in rectangles slightly longer than the diameter of the steel wafer. Note: The blue photoresist is sandwiched in two plastic sheets, a matte one and a shiny one.
5) Peel off the matte side of the laminate.
6) Place a mylar sheet as the base. Then layer a techwipe, the wafer, the photoresist laminate (newly exposed side contacting the wafer), then another layer of mylar on top.
7) Laminate the entire stack.
8) Cut wafer out from the laminate/kimwipe sandwich. Cool wafer completely. Remove the shiny plastic on the top of the wafer
9) For multiple layers, let the wafer cool completely and repeat steps 4-8. **Make sure the plastic layer on top of the wafer is removed each time before laminating a new layer.**
10) Place mask in UV aligner. Align wafer and expose. Exposure time is usually ~15 seconds for 100-150 μm devices, but it is better to err on the side of overexposure vs underexposure.
11) Develop in 1 wt% K_2CO_3 in a dish
   a. Shake the dish until the K_2CO_3 solution is saturated (fully blue).
   b. Rinse wafer with water
   c. Repeat (a) and (b) with a fresh dish of solution until most of the uncrosslinked photoresist is rinsed away. Note: for maintaining finer features, do not repeat.
   d. Using a squirt bottle filled with K_2CO_3, target the undeveloped patches until mostly dissolved, tilting the wafer so that the flow is away from the main channels. Rinse with water frequently.
   e. If overdeveloping is a concern, use a cotton swab dipped in developing solution and rub at the undeveloped patches, then rinse with water.
12) Rinse fully developed wafer with IPA then water and air dry.
13) Pour on a first PDMS layer and let it cure. Discard this—the first PDMS layer does not bond well.

A.3 PDMS Device Fabrication

We used Sylgard 184 (Dow Corning) to make our PDMS devices. The quantities are listed for 10 cm diameter wafers.

Curing PDMS

1) Make sure the vacuum oven is at room temperature.
2) Using a 150 mL disposable plastic beaker, vigorously mix 3.5 g of curing agent and 35 g base until the mixture is opaque looking and full of tiny bubbles. If changing the amounts of PDMS, maintain a ratio of 10:1 base to curing agent.
3) Place the beaker in the room temperature vacuum oven and degas for approximately 1 hour. If more than 3.5g/35g PDMS is made or a smaller beaker is used, keep an eye on the degassing, as the bubbles may overflow the beaker during degassing. Open the purge valve slowly if it looks like the beaker will overflow.
4) Prep the device master:
    a. Rinse master with IPA and water. Dry with air.
    b. Place device master on a square of folded aluminum foil. Fold up the edges to form a dish, ensuring that the walls are fairly straight and not blocking any channels. The wall height should be at least 1 cm tall. Push down on the master to ensure that it is firmly seated and flat in the aluminum.
5) Once the PDMS is fully degassed, remove from vacuum oven and pour slowly over the wafer, avoiding incorporating bubbles. Pop any large bubbles with a toothpick or a needle.
6) Degas the PDMS covered master for 1 hour, or until there are no bubbles remaining. Check the channels, as the raised photoresist will occasionally have bubbles pinned to the edges.
7) Remove the wafer from the oven and turn the oven heat to 60°C.
8) Once the oven is preheated, place the PDMS wafer in the vacuum oven and cover with a plastic petri dish cover. Check that the wafer is level and the aluminum foil walls are not bending. Cure for at least 4 hours. Longer curing is fine--the PDMS can cure overnight. Higher temperatures can be used to decrease the cure time, but the PDMS will shrink more and be stiffer, which can sometimes lead to cracking at the inlet/outlet holes when tubing is inserted or adjusted.

Bonding devices

1) Let PDMS cool to room temperature. Remove foil and slowly separate PDMS from wafer.
2) Cut out the individual devices, ensuring that the size of the resulting microfluidic chip is smaller than a glass slide and any uneven edges are cut off.
3) Place the chip so the channel is face up. Using a blunt 16 gauge needle attached to a syringe, punch out inlet and outlet holes, ensuring holes are perpendicular to the surface and that the hole is clear of PDMS remnants.

4) Use scotch tape to clean both sides of the PDMS and to cover up channels when waiting or transferring.
5) Clean glass slide by scrubbing with acetone and a Kimwipe. Then rinse with acetone, then IPA. Dry with air. Rinse with IPA then DI water. Dry with air.
6) Rinse the PDMS device with IPA, and check flow of each inlet and outlet. Dry with air. Rinse with IPA and then immediately with water, rinsing holes again. Dry with air.
7) Lay clean glass slide and PDMS device (channels up) on benchtop or other non-conducting surface. Keep discharger at least 3 feet away from other electronic devices.
8) Using corona discharger (Electro-Technic Products, SKU 12051A-10), expose glass and PDMs to air plasma. Hold the discharger very close to the surface (~ 1 mm from surface) so that purple arc is visible. Move discharger around so that all surfaces are covered thoroughly and expose for about 1 minute (30 seconds for each side for larger devices, 15-20 seconds for smaller ones).
9) Quickly place PDMS channel/exposed side down on the glass slide. Press down on PDMS to ensure all parts are in full contact and there is no debris preventing good bonding. If there is, separate the two and use tape to remove any debris. Repeat step 8.
10) Wrap the microfluidic chip in foil, leaving a gap between the PDMS and the foil. Cure for 20-30 minutes at 60-80 C in the vacuum oven or on a hot plate. Cool slowly when possible by leaving the chip in the cooling oven or hot plate. The chip can remain in the oven for a few hours at 60-80 C without detriment.

Appendix B Protocols for Particle Generation

B.1 On-chip Generation of Alginate Particles

This section offers a step-by-step procedure for generation of alginate particles and tips for common difficulties.

B.1.1 Device Set-up

For use with the 2 junction device design discussed in Chapter 3 (see Figure B-1).

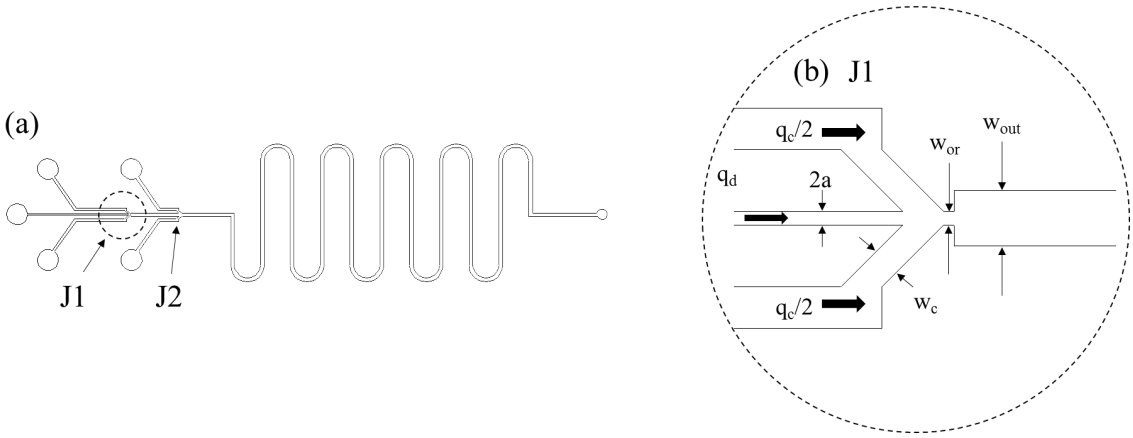

Figure B-1. Schematic of (a) the full optimized on-chip particle generation device and (b) the orifice for drop formation at the first junction (J1)

Option 1: Fill tubing first. This option is faster, but is more likely to introduce debris in device at first.

Assembling the device

1) Insert needles into unattached tubing. The inlet tubing should all be the same length
2) Fill syringes and remove air bubbles.
3) Attach syringes to needles and inject until tubing is filled
4) Attach tubing to device, inserting with tweezers.
    a. If wetting is an issue (for example, you want to avoid getting the continuous phase in the dispersed phase channel, but it is acceptable for the dispersed phase to touch the continuous phase channel), have a slight air gap at the end of the tubing when inserting.

Option 2: Attach tubing to device first.

1) Insert needles into unattached tubing

2) Insert tubing into devices, ensuring that the inlet tubing is all the same length.
3) Fill syringes and remove air bubbles.
4) Attach syringes to needles

Filling the device:

Fill at a relatively low flow rate, particularly for the dispersed phase/more viscous phase. High pressures can cause the area around the inlet to debond. For a standard drop generation device with height ~140 um, filling between 300-500 ul/hr for each continuous phase inlet and 100-300 ul/hr for the dispersed phase inlet should be safe. If backflow is occurring in the dispersed phase channel, it can be helpful to fill at 200 ul/hr for the continuous phase and 300 ul/hr for the dispersed phase until the dispersed phase has reached the first junction (J1).

B.1.2 Emulsion Drop Formation

For calcium alginate particles, the continuous phase is undecanol and the dispersed phase is aqueous sodium alginate (Na-alg).

Once device is filled, adjust flow rates by incrementally decreasing dispersed phase flow rate (q_d) and increasing the continuous phase flow rate (q_c). The ideal flow rate depends on the phases used and the target drop size. If the final flow rates are put in immediately, back flow will occur.

Ex: for a target flow rate of q_c=500 ul/hr and q_d=10 ul/hr, starting at a flow rate of q_c=300 ul/hr, q_d=300 ul/hr, adjust flow rates as listed, waiting for the flow to stabilize between each step.

1) q_c=400 ul/hr
2) q_c=500 ul/hr
3) q_d =200 ul/hr
4) q_d = 100 ul/hr
5) q_d =50 ul/hr
6) q_d =25 ul/hr
7) q_d=10 ul/hr

B.1.3 Crosslinking

Once drop formation stabilizes and the emulsion drops exit the outlet without coalescing:

1) Stop all flow.
2) Remove second set of continuous phase syringes from syringe pump (J2 inlets). This will cause some backflow in the J2 channels—try to avoid getting the dispersed phase in the J2 channels, but it is fine if there is some.
3) Switch the J2 syringes to syringes with crosslinking agent

4) Place syringes back in syringe pump, being careful not to push on plunger too hard—the buffer of continuous phase without crosslinker prevents gelation in the channel while the flow equilibrates.
5) Continue running the device at the same flow rate as before until drops are visibly gelled at the outlet. When they are gelled, the drops will no longer coalesce and instead exit in clumps if not individually. They may also stick and collect in the reservoir before exiting.
6) Check device outlet to ensure that particles are exiting without issue.

B.1.4 Rinsing and Storage of Particles

1) Take a transfer pipette and carefully remove the yellow layer of undecanol and calcium iodide closest to the alginate particles (contains calcium). Without this step, addition of water will often cause precipitation of impurities at the interface, preventing further rinsing of the particles.
2) Using another pipette, flow distilled water down the sides of the falcon tube, displacing the undecanol. Centrifuge or let the particles sit overnight.
3) Draw out the remaining oil with a transfer pipette, using a cotton ball to remove the remaining trace amounts. Fill with distilled water. To resuspend the particles for use in experiments, vortex ~10 seconds.
4) If undecanol still remains (i.e. an emulsion forms when the tube is vortexed), transfer suspended particles to a new falcon tube and repeat step 3.

B.1.5 Troubleshooting

Debris in the channel

Option 1: Flush debris backward out of inlets (good for large debris, long fibers) **safest option, but also potentially introduces the opposite phase in the channel

1) Remove tubing from the inlet that's closest to the debris.
2) Allow the fluid to flow out of inlet hole for at least 1 minute, dabbing up with a Kimwipe
3) Replace tubing and wait for flow to equilibrate.

Option 2: Flush debris forward out of device (good for small debris that won't get stuck in channel)

1) Increase flow rate of channel that has the debris until the debris is flushed out.
2) Check other channels and further downstream to ensure that the debris is not stuck in a bend or the orifice.
3) If needed, increase the flow rates of the other channels to prevent the debris from entering. This can also help flush the debris out.
4) Return flow rates to desired values and wait to equilibrate.

Option 3: Pulse (good for stuck debris)

**runs the risk of debonding the device. DO THIS LAST

1) Remove the syringe connected to the inlet closest to the debris.
2) Pulse the syringe (apply gentle pressure to the plunger and releasing repeatedly) until the debris is dislodged
3) Use Option 1 or 2 to flush the debris out of the device.
4) If debris is still stuck:
    a. remove the tubing from the inlet closest to debris
    b. Remove syringe from an inlet on the opposite end/2nd closest to the debris. Pulse the plunger until debris is dislodged. Flush with Option 1.

Backflow while running

Potential causes:

1) Air bubbles in tubing
    a. Wait for air bubbles to exit. If they are not moving:
        i. Stop syringe pumps.
        ii. Remove tubing that has air from the device.
        iii. Hold outlet of tubing above the syringe and inject until the air has fully exited
        iv. Replace tubing in device and start syringe pumps again.
2) Debris in channel
    a. Remove debris as above
3) Debonding
    a. Use a new device.
    b. Sometimes if the debonding is minimal, can clamp the PDMS to the glass slide with a large binder clip.
4) Syringe plunger is not fully flush with the syringe pump pusher block
    a. Ensure that all syringes on the same syringe pump have the same amount of fluid so that the syringes all line up.
    b. Wait for the pusher block to fully contact the plunger, allowing backflow to continue. Eventually everything from the backflow will be injected back through the device.
    c. Push the pusher block forward slightly. This can cause a large influx of the fluid, so be careful.

Gelled particles are clogging

Options:

1) Using tweezers, push down on outlet tubing to force clog out of device.
2) Pull tubing out slightly and check to see if particles exit without forming large clogs

3) Pull tubing out completely.
    a. If gelled particle clump still remains in outlet, insert needle into outlet hole and poke about. This can debond the hole slightly, but as long as the device doesn't debond, the device is still usable.
4) Pull out tubing and cut the tubing on an angle. Insert tubing with the wedge on the far side of the device (opposite of the incoming drops)

If clogging is a consistent problem, it can help to punch the device at an oblique angle (rather than perpendicular) to avoid the 90^{o} turn at the outlet.

B.2 Axisymmetric Gelation in Bath

For gelation in bath, the device set-up and protocols in B.1 are applicable through B.1.3. However, the introduction of ions is now at the exit tubing. The second set of continuous phase inlets at J2 provide additional spacing between each alginate emulsion drop.

Crosslinking

Once emulsion drops are steady and well-spaced (at least 1 mm apart, preferably 2 mm, in the exit tubing), flip the device so the tubing exits below the device (Fig. B-2). This allows the drops to maintain maximum spacing between them—they otherwise slow down as the tubing curves in the standard upright set-up. Cut the tubing to ~ 5-10 cm long, depending on bath height. This needs to be long enough to reach the interface. Mount flipped device over collection bath, raising or lowering to reach desired tubing exit height.

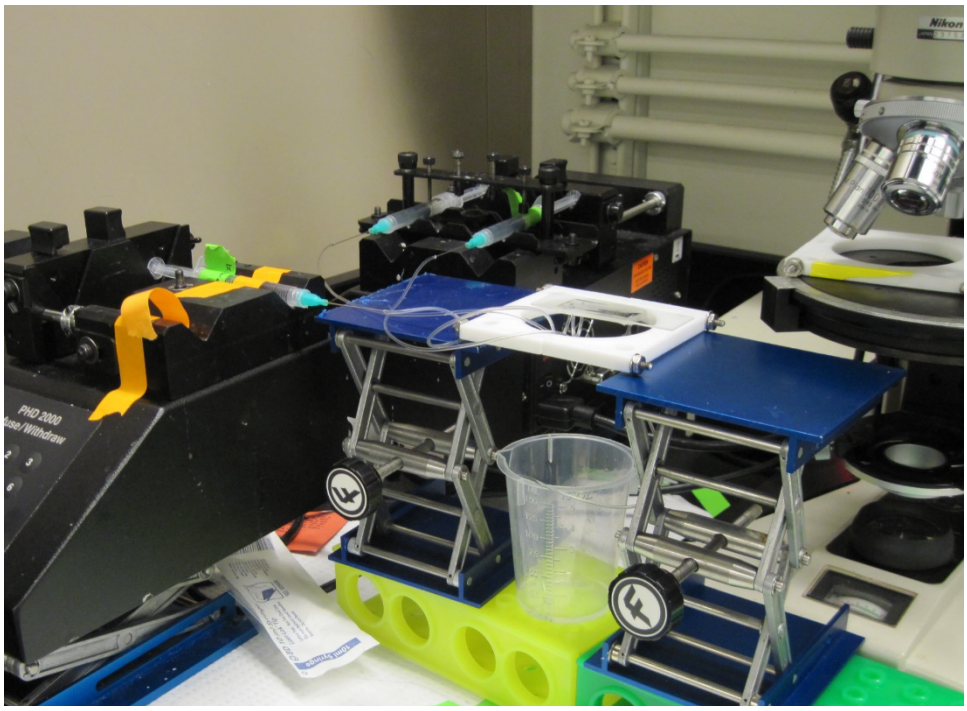

Figure B-2. Flipped device set-up

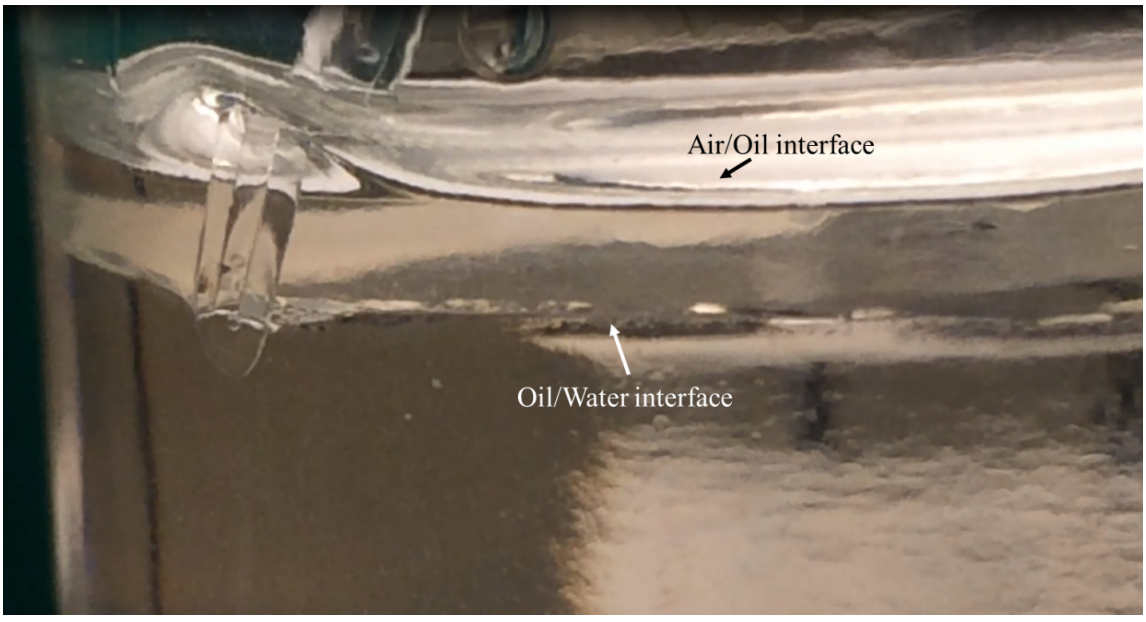

Figure B-3. Tubing outlet at interface at height = 0 mm. Negative height is below the surface. Because of the exiting oil, even if the tubing is exactly at 0 mm, there will be a thin layer of oil between the tube itself and the oil-water interface

After collecting

1) Remove collection bath and allow to settle for 15 minutes to ensure all emulsion drops have fully settled.
2) Remove oil layer with a pipette, using a cotton ball to remove any remaining oil.
3) Add DI water and dilute bath. Let settle overnight.
4) Remove majority of water carefully, avoiding disturbing the particles settled at the bottom, leaving ~5 mL or sufficient water for the particles.
5) Add water.
6) Steps 3-5 should be repeated for high glycerol wt% baths to ensure glycerol concentration is negligible, in which case centrifuging rather than overnight settling if more efficient.
7) To store device: switch the dispersed phase syringe (alginate) with oil phase (n-decanol). Flush out all alginate. Remove all syringes and cover needles

B.3 On-chip Generation of pNIPAM Particles

pNIPAM generation uses more hazardous chemicals, so always fill the syringes in the fume hood and ensure outlet waste beaker/collection bath is properly covered.

The longest device (~350 mm gelation channel) was most effective—reaction needs a fairly long residence time.

Preparation

1) Prepare the solutions in the fume hood:
   Monomer solution: 0.28 g N-isopropylacrylamide monomer in 2 mL water. Vortex until fully dissolved.
   Crosslinker (CL) solution: Bis-acrylamide. Dissolve appropriate amount of Bis-acrylamide for the targeted concentration in 10 mL of water. Mix on a hot plate with stir bar. Note: if this initial solution is 0.5 wt% CL, the final crosslinker concentration will be 0.15 wt%
   Initiator solution: Mix 0.11 g ammonium persulfate in 1 mL DI water.
2) Mix 2 mL of **monomer** solution with 960 μL **crosslinker** solution
3) Mix 1 mL of solution from **(2)** with 100 μL of the **initiator** solution. This is the dispersed phase solution.
4) Prepare the continuous phase solutions:
   For J1: Add 0.015-0.02 g emulsifier (polyglycerol-3 polyricinoleate & sorbitan isostearate, commercial name Radia 7887, WOOSUNG CNT) to 1.6 g paraffin oil.
   For J2: Add 200 μL N,N,N',N'-tetramethylethylenediamine (TEMED) to 1.6 g paraffin oil.
5) Degas the solutions under vacuum for at least 10-20 minutes. Keep an eye on the solution—too long under vacuum can volatilize the dispersed phase solution.
6) Degas under nitrogen for at least 5-10 minutes.
7) Use degassed solutions immediately (same day).

Particle generation

1) Run particle generation as described for alginate particles except for these changes:
    a. Fill syringe pumps and tubing and attach to device in fume hood. Ensure there is a sufficiently large air gap (at least 2 mm of empty tubing) between the front of the liquid in the tubing and the device so that handling the device before use doesn't cause backflow.
    b. Run with a higher flow rate ratio compared to alginate to get steady drop formation, which will end up with larger particles. The particular flow rates that were successful: qd=225 μL/hr, $q_c/2$=220 μL/hr (for each syringe).
2) Particle generation is at a steady flow rate and ready to be collected when there are a lot of tiny spheres exiting, not large clumps/coalesced particles.
3) Gelation can be confirmed by increasing the dispersed phase flow rate/decreasing the continuous phase flow rate so that large slugs form in the outlet tubing. Spread the outlet along a glass slide and allow to dry—there should be gelled strings clearly visible
4) Collect the particles in hexane that is continuously stirred with a stir bar at a moderate pace (speed 2-3)

Hydrating and storage:

1) Rinse the particles 5 times with pure hexane.
    a. Transfer particles to centrifuge tube and centrifuge at 1000 rpm for 1 minute.
    b. Draw off old hexane and add new hexane.
    c. Repeat 5 times
2) Transfer back to glass vial. Let settle at least five minutes.
3) Draw off as much hexane as possible without disturbing particles.
4) Dry under vacuum until all hexane is evaporated. The pNIPAM should look white at this point—if it's still translucent, there is still hexane.
5) Add DI water to vial and vortex for 3-5 minutes.

Appendix C Protocols for Capillary Micromechanics

This section details the set-up and procedure for obtaining a series of images needed to calculate shear and compressive moduli.

C.1 Pipette Pulling

1.2-1.5 mm diameter glass capillaries were pulled with a Sutter P-30 micropipette puller.

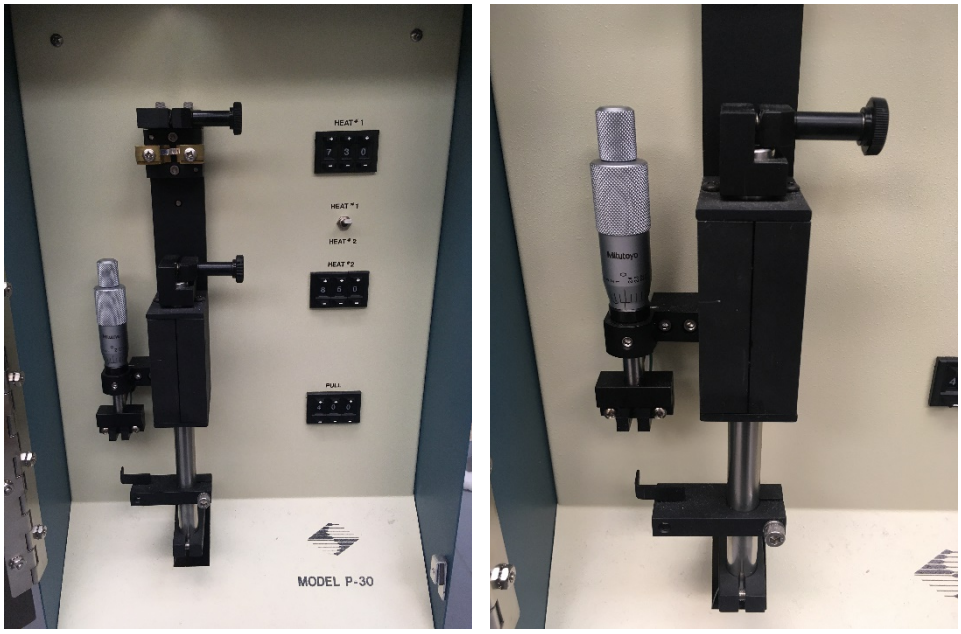

Figure C-1. Pipette puller. (a) full device and (b) micrometer for setting the gap with the optical trip point

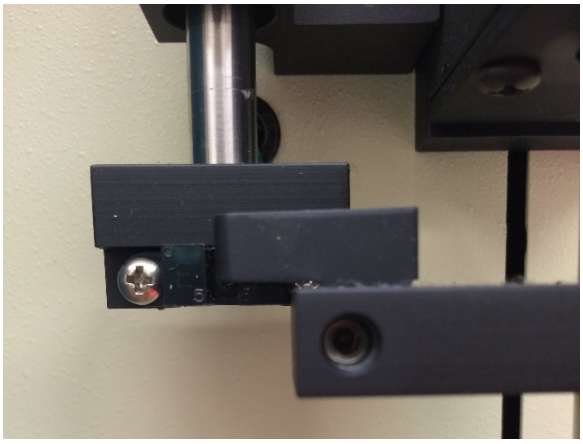

Figure C-2. Aligned trip point and flag

For a standard pull:

1) Set the Heat = 730, pull = 400, gap width 3.5”
2) To set the gap width, set 0.35” on the micrometer, which raises the sensor.
3) Clamp glass capillary to top mount.
4) Raise bottom clamp and align flag with sensor (Fig. C-2), then clamp bottom end of capillary
5) Lower sensor back to 0”
6) Close the door and press PULL. Filament should glow

With this particular pipette puller, the top half of the pulled capillary often is noticeably asymmetric and should be discarded.

As pipettes tend to be very fragile, careful transport and storage is necessary. To avoid breaking the tips, the bases of the pulled capillaries can be pressed into Sculpy clay or taped around the edge of a large plastic petri dish.

C.2 Capillary Micromechanics Protocol

C.2.1 Experimental Set-up

1) Cut ~20-30 cm long piece of 1/16” Tygon tubing (For softer particles, this can be shorter, e.g. ~10 cm. Scale this based on expected moduli or cut after characterizing the first particle of the batch). Tape one end to a plastic petri dish with clear packing tape. There should be about 2 cm untaped and free, with the end close to the center of the dish.
2) Check glass taper to see if it is a) unbroken and b) symmetric. If the end is far too narrow, gently and carefully tap the taper until the end is appropriately sized. This may take several attempts
3) Insert capillary by lifting and bending the free end of the tubing and inserting the untapered end of the capillary, tilting as necessary until the taper can fit in the petri dish. Ensure that the taper does not ever contact anything, as that will snap the tip.
4) Insert plastic 22 gauge plastic taper into tubing inlet.
5) Tape a 10 mL plastic BC syringe without the plunger to the sliding plate that is attached to the micrometer and mount (right side of Figure C-3)

.

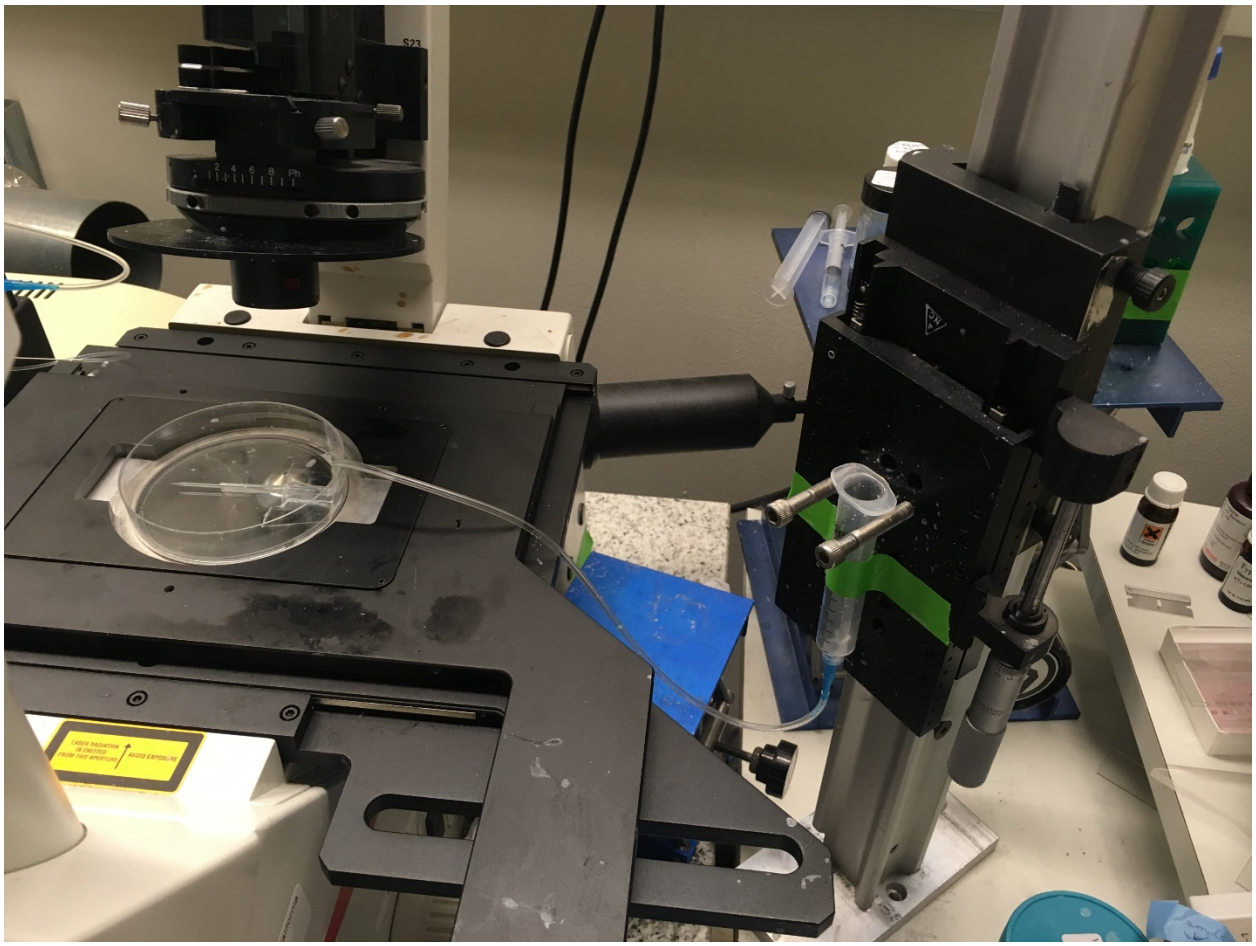

Figure C-3. Complete capillary mechanics set-up

C.2.2 Experimental Procedure

1) With a filter attached to the syringe, hand inject water carefully through the taper. Excess pressure buildup will launch the taper across the petri dish and break it. Flush about 3 mL of water through.
2) If there is debris that is too large to fit through the end, withdraw the water until the debris is back in the tubing .Carefully remove the taper, flush the debris out, and reinsert the taper.
3) Fill petri dish with water
4) Fill syringe with ~1 mL of suspended particle solution. Switch water syringe and inject until particles start entering the tubing, ~0.2 mL. Switch back to water syringe (might need to refill) and hand inject slowly until particles have entered the taper. If there is increased resistance as you inject, stop and check to see if there is debris or a particle in the taper. If the taper is starting to move, it can help to hold it at the point where it is in the tubing while injecting with the other hand.
5) Remove syringe and attach to empty 10 mL syringe on mount. Quickly add water until approximately level with petri dish water level. This is the water reservoir.

6) Observe the particles in the taper and raise and lower the water level either by filling/withdrawing water in the 10 mL syringe or raising and lowering the mount until the particle remains stationary when close to the tip—this indicates that the difference is negligible.
7) Take an image of the unconfined particle (h=0 mm)
8) With the micrometer that has a resolution of 5 μm, control the hydrostatic head. The increments will depend on the moduli of the particular batch—softer particles require smaller increments. Take images at 20 increasing heights, waiting 2 minutes between each image. If the particle seems to be moving backwards with increasing height, check the line for air bubbles. The appropriate increment is one where the particle deforms noticeably more than the previous image (want at least 1 pixel difference between each measurement, preferably 2 pixels), but close enough to get a good distribution of points for the calculation.
9) If you need more hydrostatic head than the micrometer can provide, switch the mount to the one that has millimeter markings on it. This will require manual adjustment by loosening the clamp on the plate and moving the entire assembly for each height.
10) Two options for switching particles.

    If there are more in the taper still

    a. Using the plunger of the 10 mL syringe, pulse until current particle has squeezed out of the end.
    b. Increase height of water reservoir until the next particle approaches the taper

    If there are no more available particles (they sometimes adhere to the glass), repeat from step (4)

11) Cleaning out the set-up:
    a. Hand inject and flush with 10 mL of water through a filter.
    b. Switch to filtered 50% IPA/50% water and flush with 10 mL
    c. Hand inject and flush with another 10 mL of water.
    d. Inject air to partially dry. Cover petri dish and curve tubing around it. Cover the inlet taper with parafilm.

    This is only worthwhile if the taper is particularly symmetric/well broken/clean or if you need to run more particles of the **same batch**. Otherwise, simply switch to a new taper for each new experiment.

C.3 Image Analysis

The explanation of the image analysis used to obtain shear and compressive moduli is detailed in Section 2.3.1. The measurements were obtained in ImageJ by hand. It is important to make sure that the image is rotated so that the top and bottom walls are at the same angle

Appendix D Protocols for Particle Flow Experiments

D.1 Glass Capillary Device Fabrication

This section discusses the assembly of a rectangular glass capillary channel for use in migration and deformation experiments. Glass capillary channels were fabricated in two ways, one with index of refraction matching and one minimizing distance between the channel and the lens. As long as the focal plane is acceptable, the index of refraction matched channels (section D.1.2) give clearer images, particularly near the walls.

D.1.1 Basic Glass Channel Design

The rectangular glass capillaries with rectangular cross sections were purchased from VitroCom. The sizes currently in lab:

200 μm x 400 μm x 100 mm
200 μm x 500 μm x 100 mm
400 μm x 800 μm x 100 mm
300 μm x 1000 μm x 100 mm

Standard square cross section capillaries are available directly through VitroCom. Contacting sales@vitrocom.com can provide more options for custom sizes or remnants from large orders.

For a channel overlaying a Mylar ruler (good for single particle tracking experiments):

1) Preheat the hot glue gun. Although rapid curing 2 part epoxy tends to leak less, the amount of time it generally took to level the channel often meant that the epoxy was cured before it could be used.
2) Insert capillary into tubing on either end, overlapping ~ 2 mm
3) Tape the ruler to glass coverslips on either side, overlapping about 5 mm of the ruler on the glass
4) On the microscope, overlay and center the rectangular channel and tubing on the ruler, checking that the walls are about the same width on either side—this is when the channel is level. A large glass slide can be placed underneath to use as support. When targeting a low aspect ratio device (h<w), the capillary tends to come to rest fairly level. For a high aspect ratio device, however, the device needs aligning.
5) Glue the capillary to the glass cover slips, ensuring that the intersection between the tubing and the capillary is fully sealed with glue.

Note: For help maintaining a level channel for a high aspect ratio device, it can help to tape the channel down. However, if the tape is adhered too strongly to the channel, the capillary can break.

D.1.2 Matched Refractive Index

For a device without distance markers visible within the channel:

1) Make PDMS in 150 mm diameter disposable petri dish. This generally takes a minimum of 45 g base:4.5 g curing agent to get sufficiently high channels (~3 mm thick)
2) Cut strips ~3 mm wide, 100 mm long strips of PDMS.
3) Using sufficiently long glass slide (cut 4.5”x 6” glass slide (Ted Pella) into 4.5”x 1” pieces), bond the two strips of PDMS to the glass. They should be parallel to one another, with a gap of ~5 mm.
4) Mix the fast curing 2 part epoxy.
6) Pre-glue the tubing to the glass capillary—the diameter of the tubing should fit somewhat tightly on the channel. Insert capillary into tubing on one end and glue. Repeat on the other end. Ensure that while the glue dries, the channel does not slip around or glue can get into the capillary.
7) Mix fast curing 2 part epoxy. Place some on either end of the PDMS boat
5) On the microscope, align the capillary—the glass capillary and tubing overlap should be on the epoxy
6) Press down on either end of the capillary over the epoxy until the epoxy has set. The epoxy may have attached slightly to the gloves, but should be removable.
7) Add more epoxy as needed to close either end of the channel.
8) Once the epoxy is dried, fill the channel with glycerol.
9) For determining downstream channel length, tape a Mylar ruler to the bottom of the glass near the glass capillary.

This design can be used for standard flow experiments and inertial migration experiments.

Figure D-1. Image of a filled PDMS boat with rectangular glass capillary in glycerol.

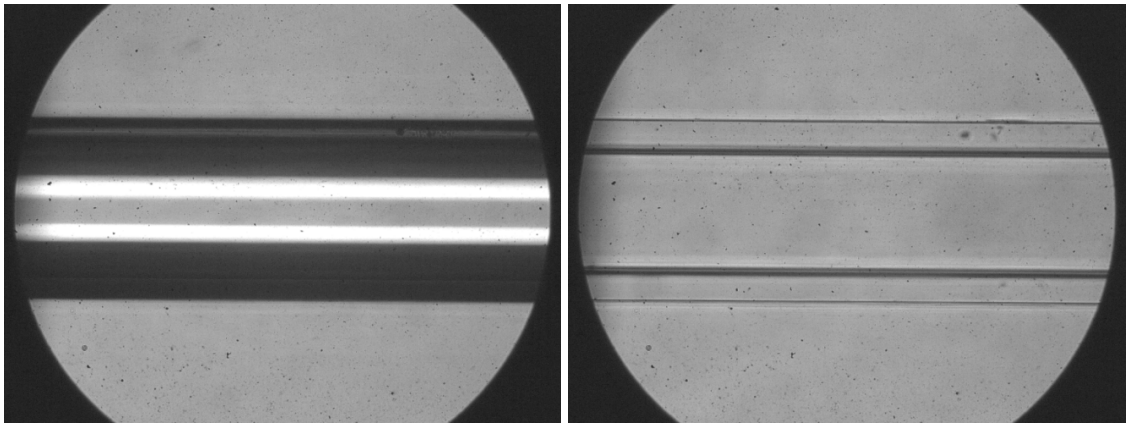

Figure D-2. Comparison of water filled glass channel (a) in air and (b) immersed in glycerol.

D.2 Image and Video Capture Optimization

This section includes some general tips for optimizing image capture in a glass capillary

1) Use rolled and flattened lab tape or cut rubber gaskets to raise device on one side if needed to ensure glass capillary is level.
2) Find the top and bottom of the glass capillary—this can generally be identified by debris or dust on the outside, but if not, it is possible to draw a mark on the top of the channel
3) Find the center of the channel by going from the bottom of the channel to (wall thickness+half channel height).
4) When using the PDMS boats filled with glycerol, avoid overfilling—the curvature of an overfilled channel will cause the image to become diffuse.
5) If the channel walls seem to become more visible after several days, remove the old glycerol with a pipette and replace with fresh glycerol. Due to its hygroscopic nature, glycerol's index of refraction will decrease as it is exposed to air.

D.3 Deformation in Flow Experiments

This section gives a step-by-step protocol for running flow experiments for examining deformation shapes.

1) Insert 22G or 24G plastic taper into tubing, depending on the tubing size.
2) Flush device with 1 mL of filtered water, then 2 mL of matched solution (e.g. the pNIPAM particles were suspended in 10 wt% 8000 MW PEG, so flush with PEG solution)
3) Switch to diluted particle solution and flow at a moderate flow rate (1000-5000 μL/hr) until particles appear.
4) Select a frame rate that allows ~10 images per particle within the window. For 400 μm x 800 μm channels, an approximate frame rate to start with is flow rate (in μL/hr) / 100 and to decrease if possible.
5) Change flow rate and capture full video toward the end of the channel.
6) Quickly skim through video to ensure that there are at least 10 particles in the video. If not, repeat.
7) Once all flow rates have been run, flush device with 2 mL each of: (a) matched solution (b) water (c) soapy water and (d) DI water, all with a filter in line. Inject air into device for storage

Note: for inertial migration experiments, this same basic protocol is used. In this case, however, each flow rate needs 100 particles rather than 10. Also, videos should be taken at multiple points in the channel, with the Mylar ruler as reference for distance downstream.

Appendix E Codes Used for Particle Characterization Image Analysis

This appendix compiles all the codes used for image analysis. Section E.1 contains the code used to obtain size distributions and compile the output. Section E.2 includes the code used for edge detection, both MATLAB and ImageJ options. It also contains the image optimization macro done in ImageJ before each stack is input into MATLAB.

E.1 Particle Size Distribution Analysis

E.1.1 MATLAB Code for Circle Detection.

Modified from Joanna Bechtel Dahl's vesicle size detection code to suit bright field particle images.

```
% Find circular shapes in single image

close all % close all open figures

% circle finding options
sens = 0.96;
method = 'twostage';
 %method = 'phasecode';

%% Load image (PNG)
% PNG image seems to give better contrast when MATLAB plotting
% This will be easier for the user when accepting/rejecting circles
file_start = 1;
totalf = 20;
for filen = file_start:totalf
    % Define input and output paths and file names
    foldername = sprintf('2017.03.13 results');
    fileName = sprintf('%d.tif',filen);
    pathName = pwd;
    bw = imread(fileName);
    outname=sprintf('%d.txt', filen);
    outpath   =   [fullfile('C:',   'Users',   'Margaret',   'Box   Sync',
'Research',...
        'Coding', foldername, outname)];
    fileOut = fopen(outpath, 'w');

    fprintf(fileOut,'Circlular Finding in %12s',fileName);
    fprintf(fileOut,'\n');
    fprintf(fileOut,'Location : %100s',pathName);
    fprintf(fileOut,'\n\n');
```

```
    %% Find circles
    % Call |imfindcircles| on this image

    % Note: "The accuracy of imfindcircles is limited when the
    % value of radius (or rmin) is less than 10." -- imfindcircles help

    % Break up radius range into 15 groups
    nRange = 15;

    figure('Position',[0   524   652*2   582]) % one screen
    % figure('Position',[-1437 391 1304  582]); % two screen
    subplot(1,2,1); hOrig = imshow(bw);
    title('Original Image')
    subplot(1,2,2); hCirc = imshow(bw); axCirc = gca;
    title('Circle Check over Original Image')

    % preallocate
    centers = cell(nRange); radii = cell(nRange);
    centersConf = cell(nRange); radiiConf = cell(nRange);
    nDiscard = zeros(nRange,1);
    centersKeep = [];  radiiKeep = []; hKeep = []; hRmv = [];
    discard = 0;

    % Change this range to suit expected particle sizes
    for i = 8:15
        if i == 1
            range = [7 10];
        else
            %range = [i*5-1 (i+1)*5-1]; % Adjust boundaries so that the
            %overlap is not too close to expected particle size
            range = [10*(i-1) 10*(i)];
        end

        [centers{i}, radii{i}] = imfindcircles(bw,range,...
            'ObjectPolarity','dark',...
            'Sensitivity',sens,'Method',method, 'EdgeThreshold', 0.03);

        currCtr = centers{i};
        currRad = radii{i};

        % output to file and screen
        fprintf('Found  %i  circles  in  the  range  %i  -  %i  px
\n',length(currRad),...
            10*i,10*(i+1))

        for j = 1:length(currRad)
            axes(axCirc)
            h                                                          =
viscircles(currCtr(j,:),currRad(j),'EdgeColor','y','LineWidth',1);
            home % return cursor to command window
            iKeep = input('Keep this circle? y/n   ','s');
            if iKeep == 'y'
                centersKeep(end+1,1:2) = currCtr(j,:);
                radiiKeep(end+1,1) = currRad(j);
```

```
                delete(h)
                % green means go
                hKeep(end+1) = viscircles(currCtr(j,:),currRad(j),...
'EdgeColor','g','LineWidth',1,'DrawBackgroundCircle',false);
            elseif iKeep == 'n'
                disp('Circle discarded')
                nDiscard(i) = nDiscard(i) + 1;
                delete(h)
            discard=discard+1;
            elseif iKeep == 's'
                disp('Skip to end')
                break
            end
        end

        % save confirmed circle info
        centersConf{i} = centersKeep;
        radiiConf{i}  = radiiKeep;

        if ge(length(currRad),1)
            % write to output file
            fprintf(fileOut,'Kept %3i of %3i circles found in the radius
range %i - %i px \n',length(radiiKeep),...
                length(currRad),range(1),range(2));
            fprintf(fileOut,'%13s %13s %13s \n','CenterX [px]',...
                'CenterY [px]','Radius [px]');
            fprintf(fileOut,'%13.3f    %13.3f    %13.3f\n',[centersKeep
radiiKeep]');
        else
            fprintf(fileOut,'No circles found in the radius range %i - %i
px \n',...
                range(1),range(2));
        end
        fprintf(fileOut,'\n\n');
        % reset
        centersKeep = [];  radiiKeep = [];

    end

    % Save final image of selected particles
    figname = sprintf('%d', filen);
    figout   =   [fullfile('C:',   'Users',   'Margaret',   'Box   Sync',
'Research',...
        'Coding', foldername, figname)];
    savefig(gcf,figout);

    %% Option to add circles that were missed

    %% OUTPUT SUMMARY OF PARAMETERS

    fprintf(fileOut,'999');
    fprintf(fileOut,'\n');
    fprintf(fileOut,'\n');
    fprintf(fileOut,'Total shapes found = %6i;',length(hKeep));
```

```
    fprintf(fileOut,'\n');
    fprintf(fileOut,'Number discarded     = %6i;',discard);
    fprintf(fileOut,'\n');
    fprintf(fileOut,'\n');
    fprintf(fileOut,'Circle Finding options [imfindcircles] \n');
    fprintf(fileOut,'Sensitivity   = %4.2f;',sens);
    fprintf(fileOut,'\n');
    fprintf(fileOut,'Method        = %10s;',method);

    fclose(fileOut);

    % Close figure for new figure
    close(gcf)

end
fclose('all')
```

E.1.2 MATLAB Code to Compile Output into a Single Excel Sheet

```
% Read txt files sequentially from another folder.
clear all
clc

% Preallocate array for total particles

Total = zeros(1000, 4);
Npart = 1;
for k = 1:20

    % Create a text file name, and read the file.
    filename = sprintf('%d.txt', k);
    foldername = '2017.03.13 results'; % Input folder name with results
    textFileName  =  [fullfile('C:',  'Users',  'Margaret',  'Box  Sync',
'Research',...
        'Coding', foldername, filename)];
        fid = fopen(textFileName, 'r');
        % Advance five lines:
        linesToSkip = 4;
        for ii = 1:linesToSkip-1
             fgetl(fid);
        end

        % Placeholder variable to keep loop going until end of file is
        % reached

        open = 1;

        while open==1

            % Check to see if circles were found in the first batch
            firstline = fgetl(fid);
            check = strsplit(firstline);

            if strcmp(check{1},'Kept') == 1
```

```
                % check to see number of particles kept
                particles = str2num(check{2});
               fprintf('%d\n', particles)
                if particles ~= 0;
                    % Skip the header line
                    fgetl(fid);
                    for n = 1:particles
                        Psizetemp = fgetl(fid);
                        split = regexp(Psizetemp,'       ','split');

                        if length(split) > 3
                            Psizetemp2 = split(2:end);
                        else
                            Psizetemp2 = split;
                        end

                        Psizef = str2double(Psizetemp2);

                        % Store the particle sizes
                        Total(Npart,1)= Psizef(1);
                        Total(Npart,2)= Psizef(2);
                        Total(Npart,3)= Psizef(3);
                        Total(Npart,4) = k;
                        Npart = Npart + 1;

                    end
                end

                % Advance to next line
                fgetl(fid);

            elseif strcmp(check{1}, 'Total') == 1
                fprintf('End\n')
                [a b] = size(check);
                split = check{b};
                npart = str2num(split);
                fprintf('Total number of particles = %d\n', npart)
                open = 0;

            else
                fprintf('No\n')
            end
        end

        textData = textscan(fid, '%s');
        fclose(fid);
fprintf('File is %d\n', k)
end

headers = {'CenterX [px]', 'CenterY [px]', 'Radius [px]', 'Image'};
filename = 'ParticleSizes.xlsx';
xlswrite(filename, headers, 'Sheet1') % by defualt starts from A1
xlswrite(filename, Total(1:Npart-1,:), 'Sheet1','A2') % array under the
header.
```

```
fclose('all')
```

E.2 Shape Edge Detection and Characterization

E.2.1 ImageJ Code for Background Subtraction

This ImageJ macro subtracts a background and determines the approximate center of mass for each image in a stack, then outputs it to a file that is inputted into the MATLAB code. It is a sample code for a particle run at 5000 μL/hr.

```
imageCalculator("Difference stack", "5000 ulhr
p20.tif","Clipboard")
run("Rotate... ", "angle=0.5 grid=10 interpolation=Bilinear
stack");
run("Save");
setAutoThreshold("Default dark");
//run("Threshold...");
setThreshold(9, 255);
setOption("BlackBackground", false);
run("Convert to Mask", "method=Default background=Dark");
run("Analyze Particles...", "size=5000-Infinity display stack");
saveAs("Results", "C:\\Users\\Margaret\\Box
Sync\\Research\\Coding\\Edge Detection\\0.5% CL\\5000 ulhr\\5000
ulhr p20 centroid.txt");
     if (isOpen("Results")) {
         selectWindow("Results");
         run("Close");
    }
run("Open Next");
```

E.2.2 MATLAB Code for Edge Detection

This MATLAB code does the edge detection on a compiled image for each particle shape. It detects the edge with a Sobel operator and interpolates a cubic spline fit. It then uses the fit to obtain the radius of curvature at the tip, the dimple length, the maximum axial length, and the maximum radius.

```
clear
nstart=1;
nend=24;
flowq = 5000;
```

```
for filen=nstart:nend

    close all
    fileName =  sprintf('%d ulhr p%d',flowq,filen);
    Ifile = sprintf('%s.tif',fileName);
    txtfilename = sprintf('%s centroid.txt',fileName);
    centroids = importdata(txtfilename);

    %input parameters
    edgetol = 0.05; % edge detection tolerance
    imthresh = 0.45; % binary threshold
    splinetol = 0.05; % cubic spline smoothing parameter
    fitfrac=0.1; % fraction of points to include for tip fitting

    % Center particles by centering centroids
    I0 = Centerstack(Ifile,centroids);
    %I0 = imread(fileName); % input grayscale image
    I = im2bw(I0,imthresh); % convert to binary
    I = bwareaopen(I,10000); % remove any outliers
    I= imfill(I,'holes'); % fill holes
    figure, imshow(I), title('binary image');
    %I = rgb2gray(I); % convert color to grayscale

    % Detect edges and fit cubic spline. Calculate circularity
    [BW1,thresh1] = edge(I,'sobel',edgetol);
    %figure;
    %imshow(BW1)
    [Ysize Xsize] = size(BW1); % pixel sizes

    [ycol xrow] = find(BW1); % x and y coordinates for detected edge

    % sort points for spline
    % recenter points to image center, which is where the particles were
centered
    [ncol nrow] = size(I);
    ycol2 = ycol - ncol/2;
    xrow2 = xrow - nrow/2*1.1;
    [angle,r] = cart2pol(xrow2,ycol2); % polar coordinates, angle
    points  =  horzcat(xrow,ycol,angle,r);  %  add  cooresponding  polar
coordinates to cartesian coord
    %sortedp = sortrows(points,3);% Use polar coordinates angle to sort
CCW,first radius, then angle
    sortedp = flipud(sortrows(flipud(sortrows(points,1)),3));% Use polar
coordinates angle to sort CCW,first radius, then angle

    % repeat first point to ensure circle
    allp = vertcat(sortedp,sortedp(1,:));
    sortx = allp(:,1);
    sorty = allp(:,2);

    % convert to cumulative arc length and fit spline individually to x
and y
    t = cumsum(sqrt([0,diff(sortx.')].^2 + [0,diff(sorty.')].^2));
    tplot = linspace(0, max(t),2500);
```

```
    % fit edge points with cubic spline
    yfit = csaps(t,sorty, splinetol, tplot);
    xfit = csaps(t,sortx, splinetol, tplot);

    % Check order of points into into spline.
    figure
 %   imshow(I)
    hold on
    plot(sortx, sorty, '.r')
    plot(nrow/2*1.1,ncol/2,'ok')
    labels = cellstr( num2str([1:length(sortx)]') );
    text(sortx,     sorty,     labels,     'VerticalAlignment','bottom',
'HorizontalAlignment','right')
  %  plot(xfit,yfit, 'b', 'Linewidth', 2)
    hold off

    % Show fit on original summed image
    figure
    imshow(I0)
    hold on
    plot(xfit,yfit, 'r', 'Linewidth', 2)
    hold off
    xlim([0 Xsize])
    ylim([0 Ysize])

        % Save final image of edge fit
        figname = sprintf('%s edge.tif',fileName);


    % Calculate circularity
    Area = polyarea(xfit,yfit)
    Perimeter = sum(sqrt(diff(xfit).^2+diff(yfit).^2))
    Circularity = 4*pi*Area/Perimeter^2

    % Calculate axes
    [maxx Imaxx] = max(xfit);
    [maxy Imaxy] = max(yfit);
    [minx Iminx] = min(xfit);
    [miny Iminy] = min(yfit);
    slopex = (yfit(Imaxx)-yfit(Iminx))/(xfit(Imaxx)-xfit(Iminx))
    slopey = (yfit(Imaxy)-yfit(Iminy))/(xfit(Imaxy)-xfit(Iminy))
    Lmax = maxx-minx
    Rmax = (maxy-miny)/2

    % Find dimple: minimum x with y centered around half of y
    yhalf = miny+(maxy - miny)/2;
    xhalf = minx+(maxx-minx)/2;
    % top half
    xfitdimpt = xfit(yfit<(yhalf+Rmax*.7));
    yfitdimpt = yfit(yfit<(yhalf+Rmax*.7));
    xfitdimpt(yfitdimpt<(yhalf))=[];
    yfitdimpt(yfitdimpt<(yhalf))=[];
    yfitdimpt(xfitdimpt>xhalf)=[];
    xfitdimpt(xfitdimpt>xhalf)=[];
```

```
    % bottom half
    xfitdimpb = xfit(yfit<(yhalf));
    yfitdimpb = yfit(yfit<(yhalf));
    xfitdimpb(yfitdimpb<(yhalf-Rmax*.7))=[];
    yfitdimpb(yfitdimpb<(yhalf-Rmax*.7))=[];
    yfitdimpb(xfitdimpb>xhalf)=[];
    xfitdimpb(xfitdimpb>xhalf)=[];


    % Calculate minimum and maximum x points

    [dimpminxt, Idminxt] = min(xfitdimpt);
    [dimpmaxxt, Idmaxxt] = max(xfitdimpt);
    [dimpminxb, Idminxb] = min(xfitdimpb);
    [dimpmaxxb, Idmaxxb] = max(xfitdimpb);

    % Determine if particle is concave or convex
    if
yfitdimpt(Idminxt)>yfitdimpt(Idmaxxt)||yfitdimpb(Idminxb)<yfitdimpb(Idm
axxb)
        fprintf('Concave\n')
        shape=sprintf('Concave\n');
            Ldimp = maxx-max([dimpmaxxt,dimpmaxxb])
       % else
        %    fprintf('Inconclusive\n')
        %    shape=sprintf('Inconclusive\n');

        %end
            % Check for fit of dimple points
    figure
    imshow(I0)
    hold on
    plot([xfitdimpb(Idmaxxb)],[yfitdimpb(Idmaxxb)],'or')
    hold off
    elseif
yfitdimpt(Idminxt)<yfitdimpt(Idmaxxt)||yfitdimpb(Idminxb)>yfitdimpb(Idm
axxb)
            fprintf('Convex\n')
            shape=sprintf('Convex\n');
            Ldimp = maxx-min([dimpminxt,dimpminxb])
                % Check for fit of dimple points
    figure
    imshow(I0)
    hold on
    plot([xfitdimpb(Idminxb)],[yfitdimpb(Idminxb)],'or')
    hold off
        %else
        %    fprintf('Inconclusive\n')
        %    shape=sprintf('Inconclusive\n');
        %end
    end

    % Check for fit of dimple points
    figure
    imshow(I0)
    hold on
```

```
    plot([xfitdimpb(Idminxb)],[yfitdimpb(Idminxb)],'or')
    hold off

    % Circle fit at the tip
    %outlier threshold
    cutxmin = max(sortx)-(Lmax*fitfrac);

    fitp=horzcat(sortx,sorty);
    fitp(fitp(:,1)<cutxmin,:)=[];

    % Fit circle to points
    [rc,a,b]=radcurv(fitp(:,1),fitp(:,2))

    % Plot circle fit
    figure
    hold on
    plot(sortx, sorty, '.')
    t = linspace(0,2*pi);plot([rc*cos(t)+a],[rc*sin(t)+b],'r')
    axis equal
    xlim([0 Xsize])
    ylim([0 Ysize])
    hold off


        % Save final image of circle fit
        figname = sprintf('%s circle.tif',fileName);
    %       figout  =  [fullfile('C:',  'Users',  'Margaret',  'Box  Sync',
'Research', 'Coding', foldername, figname)];
        saveas(gcf,figname);

    % Output important parameters
        outname=sprintf('%d p%d.txt', flowq, filen);
        %outpath  =  [fullfile('C:',  'Users',  'Margaret',  'Box  Sync',
'Research', 'Coding', foldername, outname)];
        fileOut = fopen(outname,'w');

        fprintf(fileOut,'%s\n',shape);
        fprintf(fileOut,'%f\n',Area);
        fprintf(fileOut,'%f\n',Perimeter);
        fprintf(fileOut,'%f\n',Circularity);
        fprintf(fileOut,'%f\n',Lmax);
        fprintf(fileOut,'%f\n',Rmax);
        fprintf(fileOut,'%f\n',Ldimp);
        fprintf(fileOut,'%f\n',rc);
        fprintf(fileOut,'%f\n',a);
        fprintf(fileOut,'%f\n',b);
fclose('all')
close all
end
%fclose('all')

function Asum = Centerstack(fname,centroids)
% center each frame around particle from ImageJ edge detection

%fname = '200000 ulhr 10 mm 320 um.tif';
```

```
info = imfinfo(fname);
num_images = numel(info);
%centroids = xlsread('200000 ulhr 10 mm 320 um2 centroid.xlsx');

for k = 1:num_images

    A = imread(fname, k, 'Info', info);
%    imshow(A)
    % shift image to center particle
    cent_im = centroids(k,:);
    [ncol nrow] = size(A);
    shift = [ncol/2-centroids(:,2),nrow/2-centroids(:,1)];
    Anew = imtranslate(A,shift(k,:));
    if k == 1
        Asum=Anew;
    else
        Asum=Asum+Anew;
    end

end
    % output summed image
    imwrite(Asum,'200000 ulhr sum.tif')
    %imshow(Asum)
end
```

Appendix F Sharp Bend Experiment Protocols

F.1 Attaching Tubing to Silicon Devices

The silicon devices used for the bend experiments were ones that were previously made by Shelly Gulati. Details of the fabrication can be found in her thesis or in her publications on the earlier bend experiments.

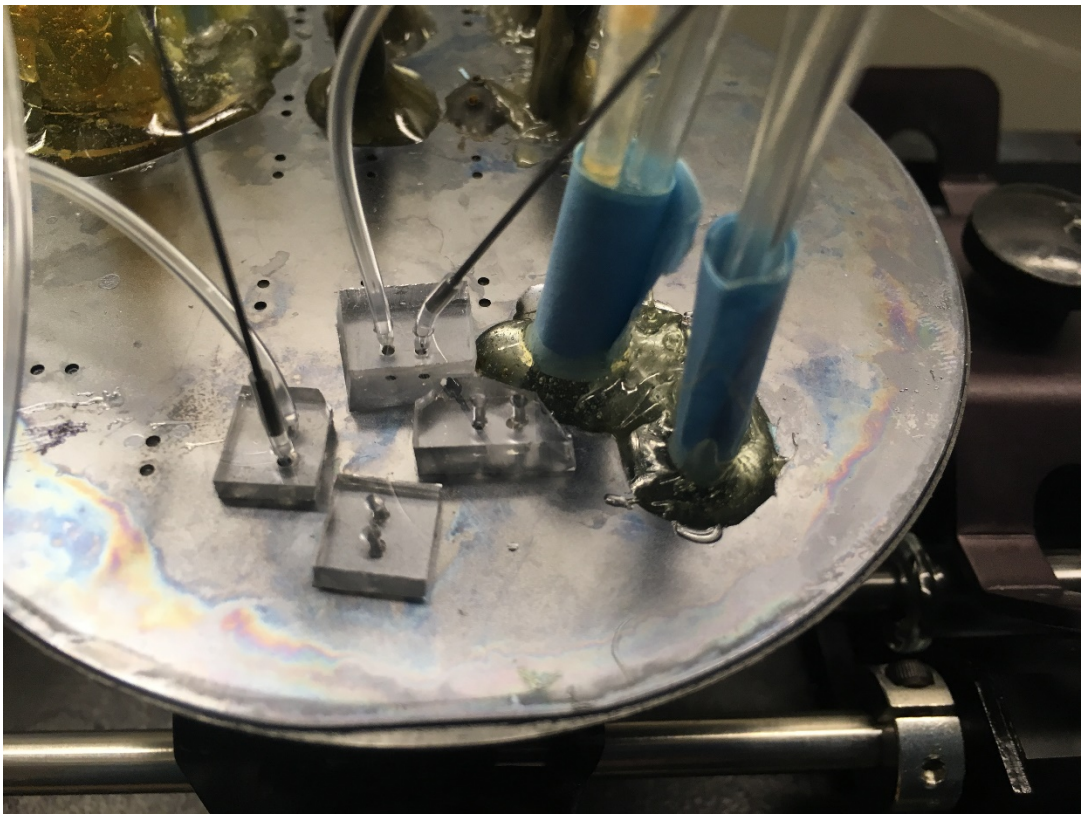

Figure F-1. Silicon wafer with inlets and outlets attached

We used two methods to attach the tubing to the through-holes in the silicon.

1) Fast curing 2 part epoxy
2) PDMS pads

For the fast curing epoxy, in order to attach both tubes at once to avoid getting epoxy into the other inlet, two ~2" pieces of 1/16" ID Tygon tubing were taped together. The fast curing epoxy was mixed. After aligning the two tube ends with the two through-holds, the epoxy was applied while maintaining a grip on the tubing. This is finicky—if the tubing slips, the epoxy will get into the channel. The tubing was held upright until 5 minutes have passed and the remaining unused mixed epoxy had become solid.

For the PDMS pads, a disk of PDMS ~2 mm thick was cured in a plastic petri dish. After tracing spacing of the through-holes onto a sheet of paper, the PDMS was laid over the paper and holes were punched into the PDMS with a blunt 16G needle. Small squares surrounding the holes were cut out. The PDMS squares were thoroughly washed with IPA then water and air dried. The appropriate areas on the silicon wafer were rubbed with a Kimwipe with IPA, the rinsed with IPA and water and air dried. The surface should look clean—sometimes when devices leak, it can leave residue on the surface that require multiple attempts to clean. The PDMS was bonded to the silicon wafer using the corona discharger, aligning the holes in the PDMS with the silicon through-holes and ensuring that the PDMS can lie flat and bond.

The PDMS pads are preferable for a range of reasons. First, fast curing epoxy eventually leaks as the device is used and the tubing is manipulated, and eventually further layers of epoxy will not be possible. In contrast, if a PDMS pad pops off, another can be bonded on. Furthermore, leaking is more evident with the PDMS connections. Finally, the smaller tubing that fits into the PDMS means that there is less dead volume to fill before the solutions switch in the corner.

F.2 Flow Experiments through a Sharp Microbend

This section gives a procedure and some trouble shooting tips for running experiments flowing solutions through the microbend.

Procedure

1) Open the inlet vent. Flush the device with 1 mL filtered soapy water (Micro-80). Check the channel for debris as it is being flushed.
2) Close the inlet vent and continue flushing with soapy water—monitor the channel for debris. If debris appears and cannot be flushed forward, withdraw/backflow until the debris is dislodged and in the inlet reservoir. Open the inlet vent and repeat (1)..
3) Switch to filtered DI water and repeat the process in (2) except with water.
4) Switch to experimental solution and repeat. Once there is no debris, ensure the inlet valve is filled with the proper solution before closing.
5) Fill the device with desired solution with tracing particles.
6) Change flow rate and wait 30-60 minutes
7) Take video at the corner.
8) Repeat steps 6 and 7 for each flow rate.
9) To flush the device after experiments are completed, first flush with DI water at 1000 μL/hr until majority of tracer particles are gone. Switch to soapy water and flush for at least 2 hours. If there is stuck debris or particles, it can help to let the channel sit overnight in soapy water before continuing to flush. Switch back to water and flush at 1000 μL/hr for at least 1 hour. If debris appears at any point and cannot flow through the device, withdraw/backflow to remove, open the inlet valve, let flush until the debris has exited, then close and continue flushing.

Generally, debris in the channel is the biggest concern. All flushing solutions need to have a syringe in line. Similarly, when making aqueous solutions, filter the DI water with syringe/filter.

F.3 Image and Video Analysis

F.3.1 Streak Imaging MATLAB Code

This code is used to generate streak images from videos.

```
clear all
close all
% file name
q = 10.89; %flow rate, ulhr
input_name = sprintf('R=0.57 10.89 ulhr 0.005%%spheres 30 min 22.3
C.tif');%, q, fps);
fname = fullfile('F:', '2017.05.05 R=0.57', input_name );
info = imfinfo(fname);
num_images = numel(info)/5;
fps = 24;
time = 1;
nsegments = 10;

% initialize average image (background)
f_ave = zeros(size(imread(fname,1)));

Nf_set =floor(num_images/nsegments); % Number of frames per set of images
in each streak image

for k = 1:num_images
    A = im2double(imread(fname, k, 'Info', info));
    % average frames for backround
    f_ave = (A + f_ave);
end
f_ave = f_ave ./ num_images;
ave_image = uint8(round(f_ave .* 255));

% If more than 1 image is made, they will show up sequentially in separate
% windows
for j = 1:(floor(num_images/Nf_set))
    % Initial image for brightness
    Streak = f_ave-f_ave;
    for m = 1:Nf_set
        % subtract out background image
        %A = im2double(imread(fname, (10*(j-1)+m), 'Info', info)) - f_ave;
        B = im2double(imread(fname, (10*(j-1)+m), 'Info', info));
        A=B - f_ave;

        % Compare two frames and take the brightest values
        Streak = max(A,Streak);
    end
    % convert image back to uint8
```

```
    Streak_out=uint8(round(Streak .* 255));
    figure
    %imshow(Streak)
% stretch image brightness
Stretchedimage = imadjust(Streak_out,stretchlim(Streak_out),[]);
figure(1)
imshow(Streak_out);
figure
imshow(Stretchedimage);
% output info
    foldername = sprintf('%4.2f ulhr', q);
    outname = sprintf(' %d frames%d.tif',Nf_set, j);
%    MLoutname = sprintf('%d fps %d frames%d.fig',fps, Nf_set, j);
    %         C:\Users\Margaret\Box         Sync\Research\Coding\Streak
Imaging\2016.05.10 R=0.52 CpCl NaSal
    outpath   =   [fullfile('C:',   'Users',   'Margaret',   'Box   Sync',
'Research',...
        'Coding', 'Streak Imaging', '2017.05.05', foldername, outname)];
%       MLoutpath  =  [fullfile('C:',  'Users',  'Margaret',  'Box  Sync',
'Research',...
%      'Coding', 'Streak Imaging', '2017.05.05', foldername, MLoutname)];

    imwrite(Stretchedimage,outpath);
   % imwrite(Streak_out,MLoutpath);
 %   savefig(MLoutpath)
 %   close 1
end
```

F.3.2 Vortex Length Measurement

Determining the vortex length and vortex length over time was done by hand in ImageJ. First rotate the video so that the inlet channel is perfectly horizontal. For each image, determine the length of the vortex as depicted in Figure F-2. This measurement needs to be done with streak images, low frame rates, or high concentrations of particles so that the vortex is clearly delineated.

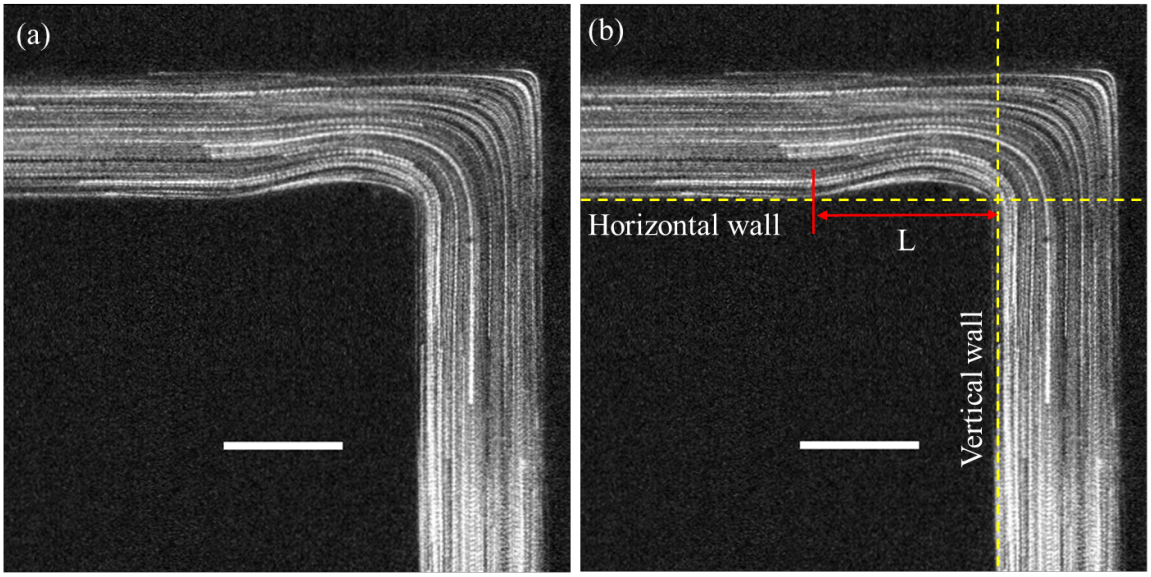

Figure F-2. (a) Streak image and (b) corresponding vortex length measurement schematic. Scale bars indicate 100 μm.